

A VALIDATION STUDY OF THE MONTANA STATE UNIVERSITY

IN-PLANE LOADER

by

Aaron Bruce Collett

A thesis submitted in partial fulfillment  
of the requirements for the degree

of

Master of Science

in

Mechanical Engineering

MONTANA STATE UNIVERSITY  
Bozeman, Montana

May 2006

©COPYRIGHT

by

Aaron Bruce Collett

2006

All Rights Reserved

APPROVAL

of a thesis submitted by

Aaron Bruce Collett

This thesis has been read by each member of the thesis committee and has been found to be satisfactory regarding content, English usage, format, citations, bibliographic style, and consistency, and is ready for submission to the College of Graduate Studies.

Dr. Douglas S. Cairns

Approved for the Department of Mechanical Engineering

Dr. Christopher H.M. Jenkins

Approved for the College of Graduate Studies

Dr. Joseph Fedock

STATEMENT OF PERMISSION TO USE

In presenting this thesis in partial fulfillment of the requirements for a master's degree at Montana State University, I agree that the Library shall make it available to borrowers under rules of the Library.

If I have indicated my intention to copyright this thesis by including a copyright notice page, copying is allowable only for scholarly purposes, consistent with "fair use" as prescribed in the U.S. Copyright Law. Requests for permission for extended quotation from or reproduction of this thesis in whole or in parts may be granted only by the copyright holder.

Aaron Bruce Collett

May 11, 2006

## TABLE OF CONTENTS

1. INTRODUCTION .....	1
COMPOSITE MATERIALS AND THE MONTANA STATE UNIVERSITY IN-PLANE LOADER	1
Isotropic Material Design.....	1
Polymer Composite Material Design.....	3
A Method to Characterize Non-Linear Composite Material Response .....	5
BACKGROUND OF THE IPL .....	7
THESIS OBJECTIVE .....	8
2. APPLICATIONS OF THE IPL.....	10
DISSIPATED ENERGY DENSITY (DED).....	10
OTHER USES OF ENERGY METHODS IN PREDICTING FAILURE IN COMPOSITES.....	19
Normalized Difference in Recoverable Energy (NDRE) [7] .....	19
Obtaining Material Properties in the Inelastic Region.....	21
VALIDATION OF DAMAGE INITIATION AND PROGRESSIVE DAMAGE THEORIES .....	22
OBTAINING MATERIAL PROPERTIES .....	23
3. FIRST GENERATION IPL CHARACTERISTICS AND FEATURES.....	25
FRAME .....	25
ACTUATORS .....	26
ACTUATOR KINEMATICS.....	27
GRIPS .....	28
DISPLACEMENT ACQUISITION.....	29
OTHER FEATURES .....	29
4. COMPONENTS OF THE IPL .....	31
FRAME .....	31
ACTUATORS .....	32
Hardware .....	32
Control and Data Acquisition.....	33
Kinematics.....	33
Test Program.....	34
GRIPS .....	34
OUT-OF-PLANE CONSTRAINER.....	37
LOAD ACQUISITION SYSTEM .....	37
Load Cells, Hardware, and Data Acquisition.....	38
Resolving Loads into Components.....	38
Frictional Loads and Load Offset Files.....	39

## TABLE OF CONTENTS - CONTINUED

DISPLACEMENT ACQUISITION SYSTEM .....	42
LVDTs.....	42
LVDT Kinematics.....	44
Position Control .....	45
Unloading Loop in Feedback .....	48
5. VALIDATION TESTS CONDUCTED ON THE IPL.....	51
DISPLACEMENT READINGS.....	51
LVDT Precision.....	51
LVDT Accuracy .....	52
OUT-OF-PLANE DEFLECTION .....	55
GRIP BENDING.....	59
GRIPPING EFFECTS.....	63
LOAD READINGS.....	67
Precision of Loads.....	67
Accuracy of Loads .....	71
DISPLACEMENT TESTS WITH SAMPLES.....	75
Tension Testing .....	76
Shear Testing .....	77
Compression Testing.....	78
6. DISCUSSION OF THE TESTING RESULTS.....	80
DISPLACEMENT READINGS.....	80
LVDT Precision.....	80
LVDT Accuracy .....	81
OUT-OF-PLANE DEFLECTION .....	82
Causes of Out-Of-Plane Deflection .....	82
Effects of Out-Of-Plane Deflection on Sample Tests.....	83
GRIP BENDING.....	84
GRIPPING EFFECTS.....	85
False Non-Linear Constitutive Response.....	85
LOAD READINGS.....	87
Precision of Load Readings.....	87
Accuracy of Resolved Loads.....	92
Relative Percent Error Figures.....	92
Absolute Load Error Figures .....	92
TENSION TESTS.....	94
Sensitivity to Material Properties .....	94

## TABLE OF CONTENTS - CONTINUED

Optimized Coupon Geometry.....	101
SHEAR TESTS.....	105
COMPRESSION TESTS .....	106
SUMMARY OF TESTING RESULTS .....	107
7. CURRENT CAPABILITIES OF THE IPL .....	108
CURRENT CAPABILITIES OF THE IPL.....	108
8. RECOMMENDATIONS FOR THE IPL AND CONCLUSION .....	111
DISPLACEMENT READINGS.....	111
OUT-OF-PLANE DEFLECTION.....	113
GRIP DEFLECTION.....	114
GRIPPING EFFECTS.....	115
LOAD READINGS.....	116
SUMMARY OF RECOMMENDATIONS .....	117
PROCEDURE FOR FURTHER VALIDATION TESTS .....	118
RECENT MODIFICATIONS .....	118
Load Cell Amplifiers and A/D Conversion.....	118
New Grips and Higher Gripping Pressure.....	120
CONCLUSION .....	121
REFERENCES.....	123
APPENDIX A: LABVIEW CODE .....	127
APPENDIX B: MATLAB CODE.....	144
APPENDIX C: ANSYS CODE .....	154

## LIST OF TABLES

Table	Page
1. ASTM classification of extensometer systems [14]. .....	54
2. Precision load tests performed with in-house built amplifiers and a 12-bit A/D converter .....	68
3. Material properties of fiberglass coupons used for IPL validation testing .....	76
4. Summary of current load errors and potential minimized load errors .....	91
5. Current advisable and not advisable testing conditions and their caveats .....	110

## LIST OF FIGURES

Figure	Page
1. The Montana State University second generation In-Plane Loader.....	8
2. Load versus displacement graph showing dissipated and recoverable energy .....	11
3. The IPL coupon and its dimensions (cm) [7] .....	12
4. Displacements of the IPL [7].....	13
5. Eight-node element representing the solution strain space linear interpolation functions [7].....	15
6. 5 x 5 x 5 cubic representing the global linear interpolation function for the strain state [7].....	16
7. Compact tension sample used to run the dissipated energy density method [7].....	18
8. Experimental and predicted crack tip opening displacement on a compact tension sample using the DED method [7].....	19
9. Dissipated energy test data from the IPL for seven different loading combinations [7].....	20
10. NDRE test data from the IPL for 7 different loading combinations [7].....	21
11. First generation IPL [7].....	26
12. Tension test data on first generation IPL with play in the initial part of the elastic curve.....	27
13. First generation IPL grips [7] .....	28
14. The Montana State University second generation In-Plane Loader.....	31

## LIST OF FIGURES - CONTINUED

Figure	Page
15. Actuator, load cell, and pivot block on the IPL [7] .....	32
16. Vector schematic of the actuator positions on the IPL .....	33
17. Grip assembly without LVDTs attached to the LVDT arms .....	35
18. Assembly of the rack and pinion gears mounted to the grip body and grip blocks .....	36
19. Assembly of the grip block showing the tie down bolt, rack gear, and grip block constrainers (grip body is not shown) .....	37
20. Diagram showing the loose fit of the bearing plates to the top in plane constrainer plate .....	40
21. $F_y$ versus $v$ curve with no sample .....	41
22. $F_y/v$ curve with displacement measured by the LVDTs and the actuators.....	42
23. IPL grip assembly with LVDTs.....	43
24. Vector schematic of the LVDTs .....	44
25. Vector schematic for the feedback loop.....	47
26. $F_y/v$ curve with backdrive due to LVDT feedback.....	49
27. Figure 27. $F_y/v$ curve without backdrive.....	50
28. Typical $F_y/v$ test with a sample showing the precision of the LVDTs after averaging each data point over 100,000 readings .....	51
29. Typical $F_x/u$ curve using the average of 100,000 readings for both force and displacement.....	52

LIST OF FIGURES - CONTINUED

Figure	Page
30. Displacement error of $v$ read by the LVDTs compared to a dial gage mounted between the top and bottom grip faces.....	55
31. Percent error of $v$ read by the LVDTs compared to a dial gage mounted between the top and bottom grip faces .....	55
32. Out-of-plane displacement as a function of sample thickness .....	57
33. Aluminum sample in tension. Out-of-plane bending measured with dial gages mounted to the front (+z) and back (-z) grips .....	58
34. Tension test with dial gages mounted between the $-z$ and $+z$ grips to show no out-of-plane deflection .....	59
35. Grip face with two mounting holes.....	59
36. Grip face with LVDT arms attached.....	60
37. $F_y/v$ displacement test measured by dial gages between the top and bottom $+x$ LVDT arms, between the top and bottom grips in the center of the grip face (at $x=0$ ), and between the top and bottom $-x$ LVDT arms .....	61
38. $F_y/v$ curves after correcting the grip bending of the $-x$ and $+x$ LVDT arm curves .....	63
39. Tension stress/strain curve of 6061-T651 aluminum measured by two dial gages; one located between the $-z$ grips and the other located between the $+z$ grips; compared to the true modulus and an independent extensometer mounted tension test .....	65
40. Aluminum tension tests on the IPL, linear and non-linear elastic regions.....	66

## LIST OF FIGURES - CONTINUED

Figure	Page
41. Steel tension tests on the IPL, linear and non-linear elastic regions.....	66
42. Typical $Mz$ versus $\omega$ curve from an IPL test with no force or displacement data averaging.....	69
43. Typical $Mz$ versus $\omega$ curve from an IPL test that averages 100,000 load cell and LVDT readings for each data point on the curve.....	70
44. $Fx/u$ curve using the average of 100,000 readings for both force and displacement.....	71
45. $Fy/v$ curve using the average of 100,000 readings for both force and displacement.....	71
46. Load error of $Fx$ loads versus true $Fx$ loads.....	72
47. Percent error of $Fx$ loads versus true $Fx$ loads.....	73
48. Load error of $Fy$ loads versus true $Fy$ loads.....	73
49. Percent error of $Fy$ loads versus true $Fy$ loads.....	74
50. Moment error of $Mz$ loads versus true $Mz$ loads.....	74
51. Percent error of $Mz$ loads versus true $Mz$ loads.....	75
52. $Fy/v$ slope versus % error for aluminum, steel, and fiberglass samples.....	77
53. $Fx/u$ slope versus percent error for aluminum, steel, and fiberglass samples.....	78
54. $-Fy/-v$ (compression) slope versus percent error for aluminum, steel, and fiberglass samples.....	79

## LIST OF FIGURES - CONTINUED

Figure	Page
55. Log scale plot of relative standard deviation versus the force at which the data was taken. Standard deviation taken with 20,000 readings per data point .....	88
56. $\epsilon_y$ versus $E$ and $\nu$ according to elastic constitutive plane stress equations. $\sigma_x = \sigma_y$ .....	95
57. $\sigma_y$ versus $E$ and $\nu$ according to elastic constitutive plane stress equations. $\sigma_y = \sigma_x$ .....	96
58. Percent difference in major strain due to a 10% lower Poisson's ratio as the ration of minor to major stress varies.....	97
59. Percent difference in major stress due to a 10% lower Poisson's ratio as the ratio of minor to major strain varies.....	98
60. $Fy/\nu$ as elastic modulus is varied 20% for the test coupons in Figure 66.....	99
61. $Fy/\nu$ as Poisson's ratio is varied for the test coupons in Figure 66.....	99
62. $Fx/u$ as Young's Modulus is varied 20% for the test coupons in Figure 67 .....	100
63. $Fx/u$ as Poisson's ratio is varied for the test coupon in Figure 67.....	100
64. IPL coupon geometry [7] .....	102
65. Impractical optimized coupon geometry for aluminum tension tests.....	104
66. Practical optimized coupon geometry for aluminum tension test .....	105
67. Optimized aluminum coupon for shear tests.....	106

LIST OF FIGURES - CONTINUED

Figure	Page
68. Macrosensor GHSAR 750 LVDT [18] .....	111
69. Schematic of the NRL IPL grips and LVDT setup [5] .....	112
70. Proposed setup of the IPL to eliminate out-of-plane bending .....	114
71. Press fit grip face assembly .....	115
72. Absolute standard deviation versus force at which the data was taken. 20,000 readings were taken per data point.....	119
73. Old, predicted, and new load precision data on a log scale plot. Old load cell data was taken with in-house built amplifiers and 12 bit A/D conversion. New load cell data was taken with Omega DMD-465 amplifiers and 16 bit A/D conversion. ....	120
74. Sample of carbide alloy coated metal for gripping composites from Carbinite Metal Coatings .....	121

## ABSTRACT

Characterizing a polymer composite material's response to loading beyond the elastic region is less well defined than it is for other structural materials such as metals. The Naval Research Laboratory has developed a method that uses dissipated energy as a metric to facilitate this characterization. The method relies on empirical data from material strength tests as well as finite element analysis data to make the prediction. A substantial amount of empirical data from different loading conditions is needed to characterize a material. This warrants a testing machine that can apply several loading conditions simultaneously to a sample.

Montana State University has built an In-Plane Loader capable of applying all three in-plane displacements to a sample of material: two translations and a rotation. Montana State University's In-Plane Loader requires validation testing to clearly define its precision, accuracy, and current usefulness.

This study has found that the Montana State University's In-Plane Loader works well for test samples that are below a certain stiffness and that some test materials work better than others. The bounds of the current In-Plane Loader are established in this thesis and modifications are suggested.

## CHAPTER 1

## INTRODUCTION

Composite Materials and the Montana State University In-Plane Loader

Polymer composite materials are being used more and more as applications demand higher strength and lower weight materials than conventional engineering materials. These two characteristics are possible in polymer composites since the strength comes from long continuous ceramic fibers, often glass or carbon fibers, aligned in a lightweight polymer matrix. Both of these materials are relatively brittle by themselves but by combining the two the toughness increases dramatically. This is because the fibers arrest cracks propagating in the matrix. The result is a material that can reach the strength of steel and be as light as aluminum. Of course, there are certain challenges to designing with composites that do not exist with other structural materials such as metals. Overcoming some of these design challenges is the motivation for the Montana State University In-Plane Loader (IPL). It is instructive to discuss briefly how design is done using isotropic materials compared to designing with polymer composites. That leads into an introduction of a method to deal with some complexities of composite design, which justifies the existence of the IPL.

Isotropic Material Design

Determining a material's properties is the first step in engineering a structure made out of that material. Uni-axial testing machines are invaluable resources for

accomplishing the task of obtaining structural material properties. These properties are usually obtained by applying tension or compression forces and measuring the subsequent displacement of the specimen. From the force/displacement data, stress/strain graphs can be obtained. A uni-axial tension or compression test can yield the two fundamental elastic material constants for an isotropic material: elastic modulus and Poisson's ratio. Other important parameters such as yield strength, ultimate strength, fracture strength, toughness modulus, and strain to failure can also be obtained [1]. These properties can then be used to characterize the material's response to applied forces for a structure's geometry.

Ideally, the response can be characterized in the elastic, inelastic, and final failure regions. Ductile materials generally have their usefulness limited by yielding whereas brittle materials are limited by fracture. Consequently, failure for ductile materials is usually defined by the yield stress or strain of a material and fracture is defined by ultimate stress or strain [1]. The response in the elastic region is defined through elasticity theory and is well established for many materials. The inelastic region is characterized by plastic deformation analysis. Failure theories, for first and ultimate failure, such as the Von Mises failure criterion or the Tresca failure criterion describe failure for relatively ductile isotropic materials. The maximum normal stress fracture criterion is used for failure of brittle materials. Buckling theory or collapse analysis applies to geometries that lend themselves to those types of failure such as beams, columns, and plates. Crack growth can be analyzed via fracture mechanics if the material is brittle enough with self-similar fracture properties [1].

### Polymer Composite Material Design

Obtaining material properties for composites is more difficult than for isotropic materials. First, composite material properties are sensitive to the manufacturing process. Wavy fibers, voids in the matrix, varying laminate thickness, and differing fiber volume percentages are all factors that can change the material's properties [2]. Second, composite materials are usually assumed to be orthotropic (if the fibers are aligned in the matrix or have a random mat construction) but can be estimated as transversely isotropic if the material properties are the same for all directions in one of the planes of symmetry. If the composite is defined to be orthotropic, nine elastic constants are required to characterize the composite (three elastic moduli, three Poisson's ratios, and three shear moduli). Transversely isotropic materials only have five elastic constants since the transverse and thickness directions are assumed to have the same properties. Consequently, obtaining material properties for composites is more difficult than for general isotropic materials given the sensitivity to the manufacturing process and the need for more elastic constants to characterize the composite. If elastic constants are obtained for a composite material, elastic composite theory does a good job of predicting the response from an applied load for a given geometry.

Composites don't have a yield point per se since inelasticity is due to matrix and fiber cracking rather than yielding of the laminate. One concept of laminate failure is based on individual ply failure since the laminate as a whole is not regarded as a homogeneous structure but rather as distinct plies. The stresses or strains in each ply are

compared to the strength properties of that ply. The other concept of laminate failure is based on fracture mechanics [3].

Many first ply failure criteria have been proposed for composites. The common theme among them being that a specific stress or strain level in a ply is exceeded thereby failing the entire ply [3]. Some work better than others [2]. Progressive laminate failure theories have been proposed which discount the residual strength in failed plies to a greater or lesser extent. These theories attempt to define the residual strength of the laminate based on the residual strength of the individual plies. There are two problems inherent in these approaches. The first is that residual strength in a failed ply is due to fiber/matrix interactions but the theories have already assumed homogeneity within the plies. The other is that residual strength within the laminate is based on ply-to-ply interactions but the laminate analysis is based on individual plies acting independently of each other. Three-dimensional laminate stress analysis must be conducted to account for the displacement continuity and traction stress equilibrium across the ply interface [3].

Composite material softening after initial failure is characterized by a series of cumulative damage events as matrix material and fibers crack and break. Thus, the inelastic region in polymer composites has to take into account the varied fracture events that happen after initial softening. The inelastic region in composites is analogous to crack propagation in isotropic materials. In this failure region, there is still residual strength. Fracture mechanics predicts this strength adequately in brittle isotropic materials and for delamination in composites. It has been used as well to describe matrix cracking in transverse angled plies but it is not well established how this affects laminate

residual strength [2]. It works less adequately in predicting crack growth across fibers since damage zones become large when the crack meets an interfering fiber. The direction of crack propagation in isotropic materials is proposed to follow a path perpendicular to the principal stresses [4]. Conversely, a crack in the matrix of a composite is arrested by a fiber, which re-aligns the crack with the fiber. The crack can then be classified as a delamination between the fiber and matrix. This continues until the energy required for the crack to follow the fiber is greater than the energy required to propagate into the matrix again. This process yields a large damage zone and a high fracture toughness. It also makes predicting residual strength using fracture mechanics in composite materials less accurate. The combination of elastic ply theory in three-dimensions and elastic fracture mechanics for matrix cracking (using an energy criterion for failure) has been suggested [3].

Failure in composites is an open problem notwithstanding the previous discussion on the topic. Part of this is due to the relative recent use of engineered composite architectures compared to classical engineering materials. Composites are also more complicated than isotropic materials. Composite material failure is thus a topic that invites further study.

#### A Method to Characterize Non-Linear Composite Material Response

The Naval Research Laboratory (NRL) has proposed a method that uses empirical and finite element data from a test sample of a composite material to predict the behavior of composite materials in the inelastic region [1]. The basics of the method are as follows. A finite element (FE) model is used to supply a map of the elastic strain state

for the test sample for given loading conditions. Tests with the same loading, geometry, and material are run to failure and force versus displacement plots are generated. From these plots, dissipated energy versus displacement plots are created (dissipated energy is the amount of energy dissipated by material softening. It is described in more detail in a subsequent section). A scaling function maps the empirical dissipated energy to the elastic strain states obtained from the FE model. This function is called a dissipated energy density function. Since the dissipated energy density function is not known a priori, it must be found from the two pieces of information known from the test and the FE analysis: dissipated energy and sample strain state respectively. The function essentially provides a relationship to form a dissipated energy state in the sample from an elastic strain state. Once this function is known, it can be used to provide a dissipated energy state in another structure made of the same material by acquiring the strain state of the structure using a FE model and mapping that to a dissipated energy state. The amount of dissipated energy in the structure can then indicate the level of damage in that structure.

In order to find an accurate dissipated energy density function, as much empirical data as feasible are desired. This means either performing tests with a single kind of loading on many different sample geometries or performing tests with many different loadings on a single sample geometry. The latter is preferable for ease of manufacturing samples and running FE models on those samples. This lead to the concept of a multi-axial testing machine: specifically, a machine that can apply three in-plane displacements

to a sample of material:  $u$ ,  $v$ , and  $\omega$ . These displacements produce shear forces, tension or compression forces, and moment couples in the sample respectively.

The NRL has built such a machine; it is called the in-plane loader or IPL [5]. It is rather large, expensive, and intricate. The composites research group at Montana State University under the direction of Dr. Douglas Cairns wanted to duplicate the functionality of NRL's IPL but with a machine that is simple and less expensive. The Office of Naval Research has funded the project with a desire to characterize polymer matrix composite materials for application in naval ships and planes.

### Background of the IPL

The MSU IPL was initially designed as an ME 404 senior design project by Eric Booth, Marc Schaff, and Kim Higgins [6]. Additional construction of the machine was then done by Will Ritter, Jeremy Kingma, Sarah Grochowski, Bryan Bundy, Jay Smith, John Parker, and Aaron Collett. The overriding design concept of Montana State University's IPL was to be relatively inexpensive, small, and portable compared to NRL's IPL. As such, MSU's IPL was built with off-the-shelf components whenever possible. All of the machining was completed at MSU, the majority done by students in the student machine shop. Additional machining was performed by the Computer Integrated Machine lab and the College of Engineering Tech Services at Montana State University.

Since the initial or first generation of the IPL, modifications have been made. Figure 1 is a picture of the second generation IPL. The IPL applies loads to a sample of material by moving one grip with respect to the opposing grip. The movements can be

anywhere in the plane of the IPL. This can be described by the three planar degrees of freedom: two translations and a rotation. These correspond to  $x$  and  $y$  direction translations and a rotation around the  $z$  axis, respectively.

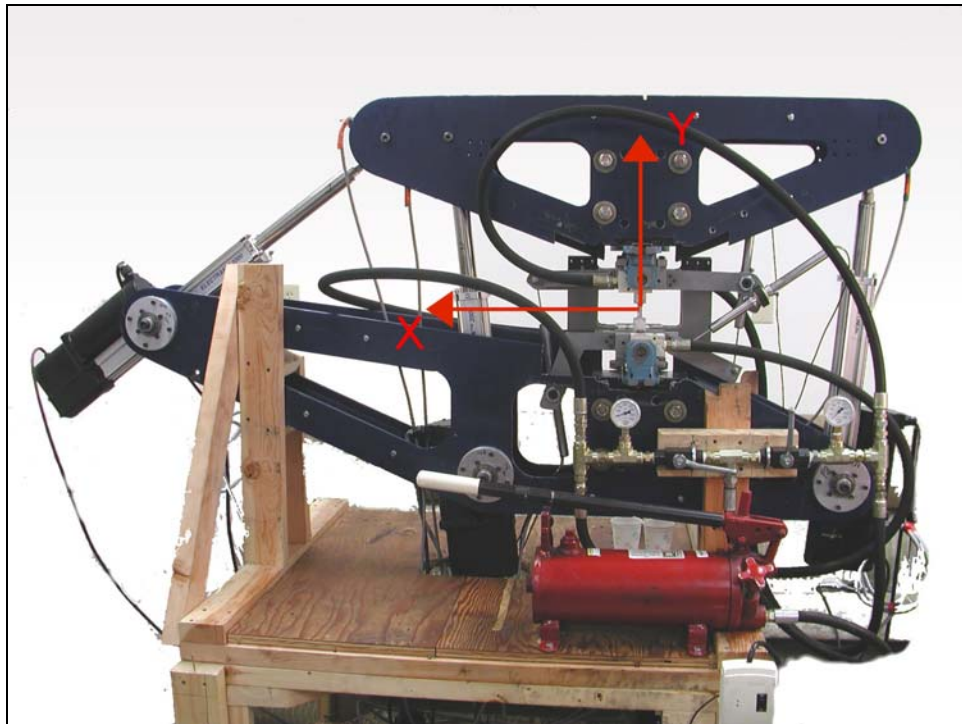


Figure 1. The Montana State University second generation In-Plane Loader

### Thesis Objective

Construction of the MSU IPL began in 2002 by the ME senior design team previously mentioned. Since then it has passed through the hands of others that have made improvements to almost all components and systems. Accurate output of loads and displacements during a test is of primary concern. This merits a quantification of the precision and accuracy of the IPL, which is the purpose of this study. A detailed presentation of how the IPL data is used to predict composite material softening is given first to provide a firm argument for the existence of the IPL. Following that, the first

generation IPL is introduced along with a summary of the modifications made. The second generation IPL is then presented by examining the main components to see where existing problems may take root. Many tests were run to determine the precision and accuracy of the loads and displacements and those are presented thereafter. A discussion then follows that attempts to explain where and how the inaccuracies and imprecisions from the tests arise. A judgment is offered that qualifies the current state of the IPL and the bounds of its usefulness. Finally, recommendations are made to modify the IPL to increase precision and accuracy.

## CHAPTER 2

## APPLICATIONS OF THE IPL

The IPL was primarily built to accommodate the method proposed by NRL in analyzing composite material softening. It can be used in other ways, however. NRL's method is discussed first and is then followed by other methods.

Dissipated Energy Density (DED)

A method developed by Mast et al. [5] of the Naval Research Lab to evaluate the damage experienced by a composite material is done by using a parameter called dissipated energy density (Ritter [7] has also discussed this method). This is proposed to be a material property since it only depends on the material makeup of a composite. Dissipated energy is shown in Figure 2 as the difference between the total absorbed energy in a material and recoverable energy.

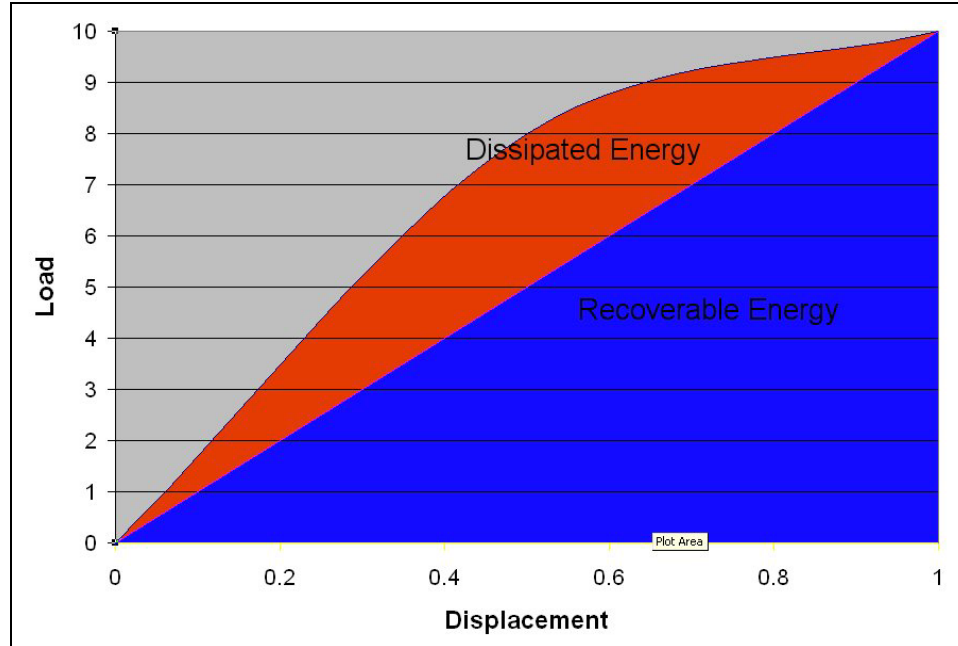


Figure 2. Load versus displacement graph showing dissipated and recoverable energy

As shown, when dissipated energy exists, damage is occurring because the material is outside of its linear elastic zone. Composite materials respond differently to loads than metals in that metals experience permanent deformation whereas composites recover the deformation. Mast et al. [5] propose that a dissipated energy density function, which is only a function of material, can be used to predict dissipated energy in a structure of the same material. The procedure uses experimental data as well as finite element modeling to correlate a linear strain state to a dissipated energy state, the latter being a measure of damage in a material. The following process describes how this is done.

1. Several load versus displacement curves are obtained via several experiments for a material. The coupon geometry proposed for testing by Ritter is shown in Figure 3.

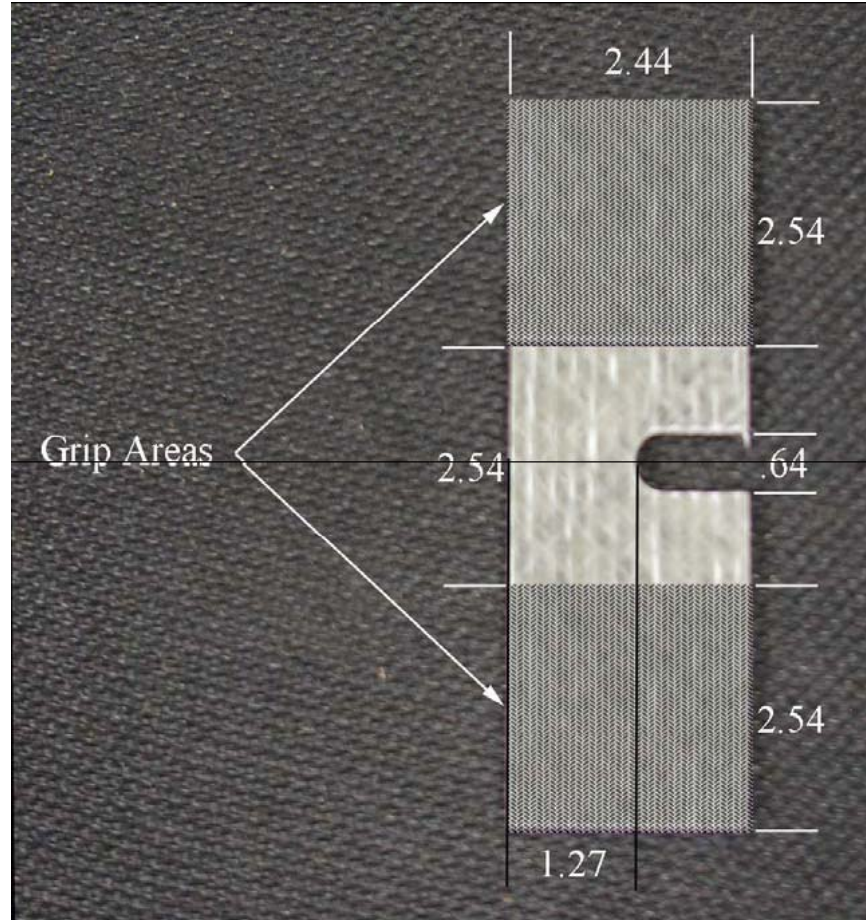


Figure 3. The IPL coupon and its dimensions (cm) [7]

Ritter [7] proposes seven different tests, each with its own loading path. They are:

- a. pure shear displacement  $u$
- b. pure axial displacement  $v$
- c. pure rotation  $\omega$
- d. combination of shear and axial displacement  $u + v$
- e. combination of shear displacement and rotation  $u + \omega$
- f. combination of axial displacement and rotation  $v + \omega$
- g. combination of all three displacements  $u + v + \omega$

These displacements are shown in FE models in Figure 4.

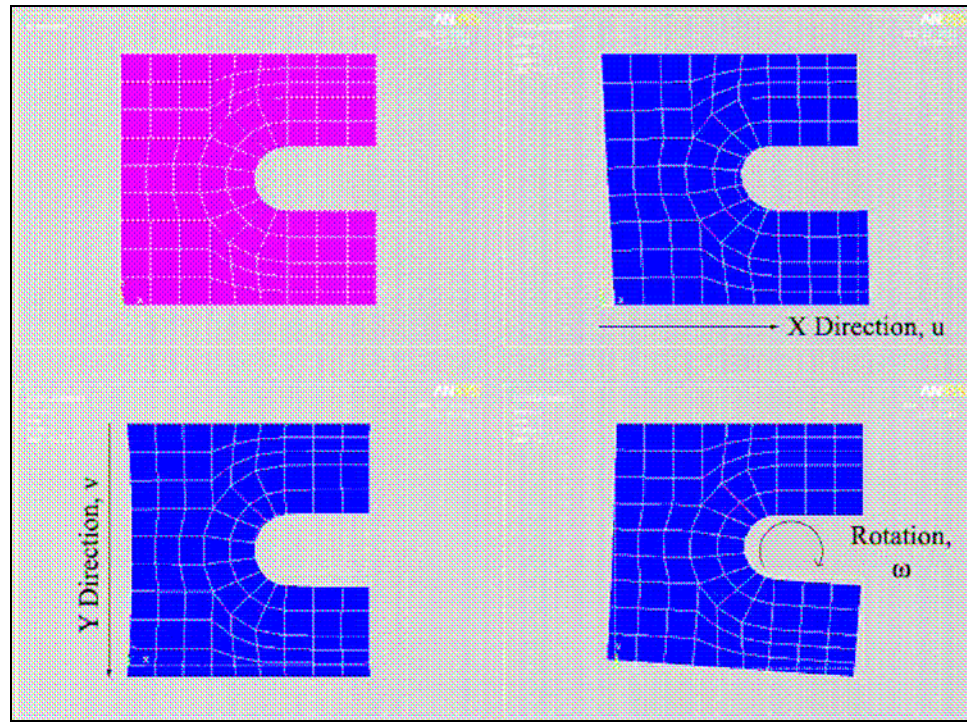


Figure 4. Displacements of the IPL [7]

It can thus be seen that to produce the same loading paths with a single-axis testing machine, many more samples with different architectures are required. The IPL is especially suited to this method since it can produce three boundary displacements in one test and one sample of material. For each test, dissipated energy versus boundary displacement curves can be derived from the load versus displacement curves. This produces three dissipated energy versus boundary displacement curves ( $u$ ,  $v$ , or  $\omega$ ) for each loading path or test. The total dissipated energy for each boundary displacement state can then be obtained by adding the three curves.

2. An FE analysis is conducted for the samples being tested with the appropriate boundary displacements applied (loading paths). The strain state for each element is obtained which, for a planar structure, is defined by the material properties coordinate axes  $\epsilon_{11}$ ,  $\epsilon_{22}$ , and  $\epsilon_{12}$  where 1 is in the fiber direction and 2 is transverse. In practice only the three boundary displacements  $(u, 0, 0)$ ,  $(0, v, 0)$ , and  $(0, 0, \omega)$  need to be applied since a linear superposition of strains can be applied to get any of the loading paths and magnitudes.
3. Dissipated energy density is obtained from the strain state in each coupon via a dissipated energy density function. This function can take several forms. Ritter [7] uses a linear interpolation function. The goal is to deconvolute the dissipated energy density, which is a function of geometry  $s$ , loading  $l$ , material  $m$ , and position in the structure  $\mathbf{x}$ , to a function of two variables, one a function of material only  $c(m)$  and the other a function of strain  $f(\epsilon)$  [5][7] (strain is a function of  $s$ ,  $m$ ,  $l$ , and  $\mathbf{x}$ ) (Equation 1):

$$\phi(m, \underline{\epsilon}) = c_i(m) f_i(\underline{\epsilon}). \quad 1$$

At this point,  $c_i$  is an unknown set of coefficients and the set of  $f_i$  functions can be completely defined by the strain state in the element which is known from the FE model. The  $f_i$  functions are defined by the variables

$$\begin{aligned} \alpha &= \frac{\epsilon_{11} - \epsilon_{\min}}{\epsilon_{\max} - \epsilon_{\min}} \\ \beta &= \frac{\epsilon_{22} - \epsilon_{\min}}{\epsilon_{\max} - \epsilon_{\min}}, \\ \gamma &= \frac{\epsilon_{12} - \epsilon_{\min}}{\epsilon_{\max} - \epsilon_{\min}} \end{aligned} \quad 2$$

which are local variables in the eight-node linear interpolation element shown in Figure 5.  $\varepsilon_{\max}$  and  $\varepsilon_{\min}$  are the maximum and minimum strains out of all strain directions, elements, data points, and loading paths for a material obtained from the IPL tests.

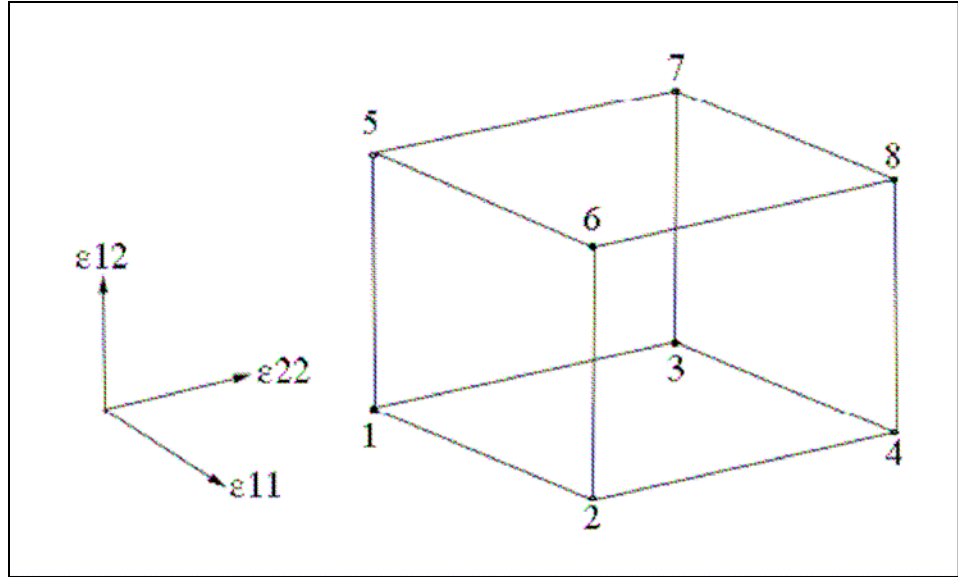


Figure 5. Eight-node element representing the solution strain space linear interpolation functions [7]

The  $f_i$  functions have the characteristic of being 1 at the  $i^{\text{th}}$  node and zero at the other nodes [7]:

$$f_1 = (1 - \alpha)(1 - \beta)(1 - \gamma)$$

$$f_2 = (\alpha)(1 - \beta)(1 - \gamma)$$

$$f_3 = (1 - \alpha)(\beta)(1 - \gamma)$$

$$f_4 = (\alpha)(\beta)(1 - \gamma)$$

$$f_5 = (1 - \alpha)(1 - \beta)(\gamma)$$

$$f_6 = (\alpha)(1 - \beta)(\gamma)$$

$$f_7 = (1 - \alpha)(\beta)(\gamma)$$

$$f_8 = (\alpha)(\beta)(\gamma)$$

In Equation 1,  $\varphi$  is the dissipated energy density at any point in the solution element. To increase the accuracy of the dissipated energy density function the strain space is divided into 64 elements which gives 125 nodes. The number of coefficients therefore is  $i=125$  which correspond to the nodes in a global  $5 \times 5 \times 5$  cubic (Figure 6). The coordinate axes represent the three strain axes  $\varepsilon_{11}$ ,  $\varepsilon_{22}$ , and  $\varepsilon_{12}$ .

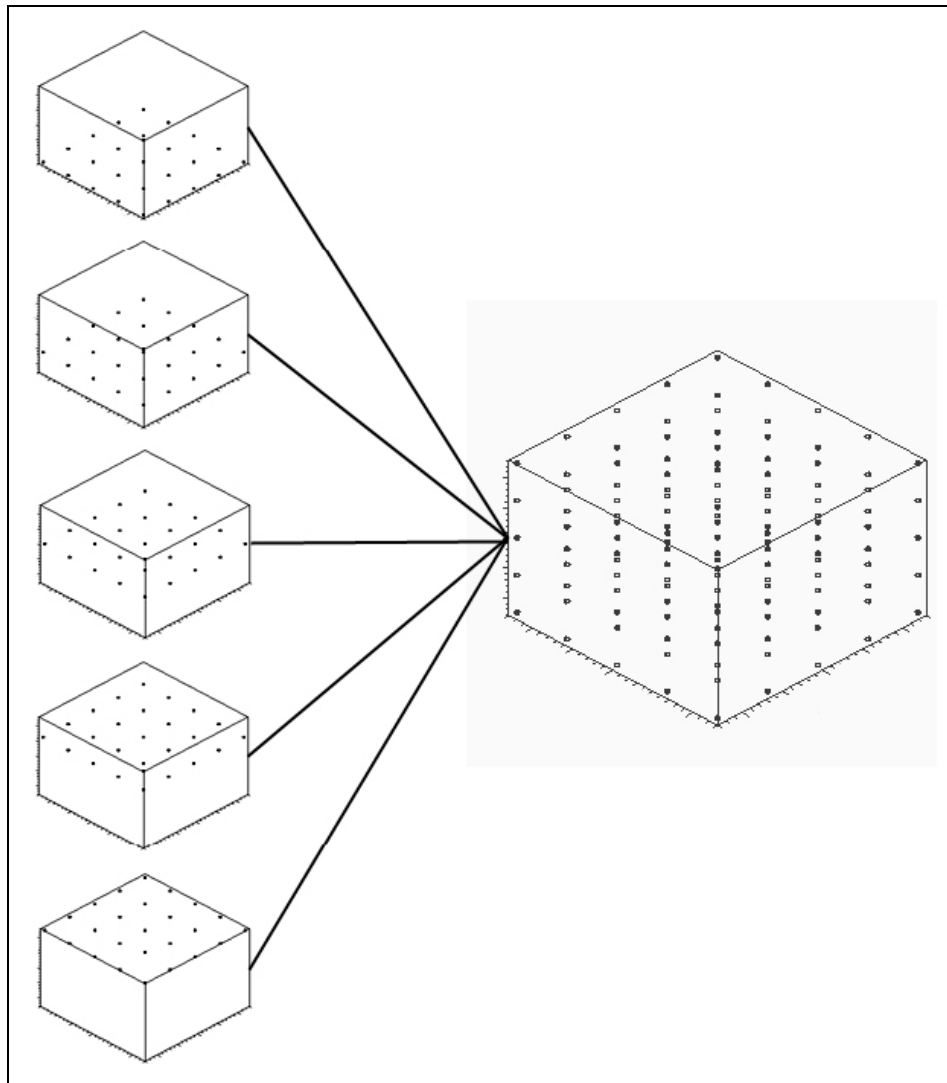


Figure 6.  $5 \times 5 \times 5$  cubic representing the global linear interpolation function for the strain state [7]

Each element in the 125 node cubic is similar to the single element shown in Figure 5. The result is an array of 64 piecewise linear interpolation elements.

4. Dissipated energy ( $\Phi$ ) in each element of the finite element model is found by simply integrating the dissipated energy density function over the volume of the element:

$$\Phi = \int_{V_{element}} \phi dV_{element} . \quad 4$$

In practice this is done by multiplying the energy density function in the element by the volume of the element.

5. The total dissipated energy in the coupon is found by summing the dissipated energy in each element over all the elements in the coupons. Equation 5 then describes the dissipated energy in the coupon as a scalar equal to the row vector of 125 interpolation function values times the column vector of 125 coefficients. This is the equation for one data point on one test:

$$\Phi = \{F\}^T \{C\} . \quad 5$$

6. To take into account the rest of the data points on one test and the data points for the rest of the tests, vertical concatenation of all data points is done to get:

$$\{\Phi\} = [F] \{C\} , \quad 6$$

where  $\{\Phi\}$  is a vector containing dissipated energy values for each data point on all tests.  $[F]$  is a matrix of interpolation function values having 125 columns and *# of data points* rows.  $\{C\}$  is a column vector containing the 125 coefficients. The number of rows in  $[F]$  has to be greater than the number of columns; therefore, this is an optimization problem. The error between the experimental

dissipated energy and the FEA acquired function in Equation 7 needs to be minimized to find  $\{C\}$ .

$$|[F]\{C\} - \{\Phi\}| = e. \quad 7$$

7. Once  $\{C\}$  is found, it can be used to obtain a dissipated energy density map on a structure with similar material makeup but different geometry and loading than the tested coupon. This is done by solving the forward problem:

$$\{\Phi\} = [F]\{C\}. \quad 8$$

At this point,  $\{C\}$  is known and  $[F]$  is known from an FE model of the new structure.

Ritter [7] has run this procedure on a compact tension sample shown in Figure 7.

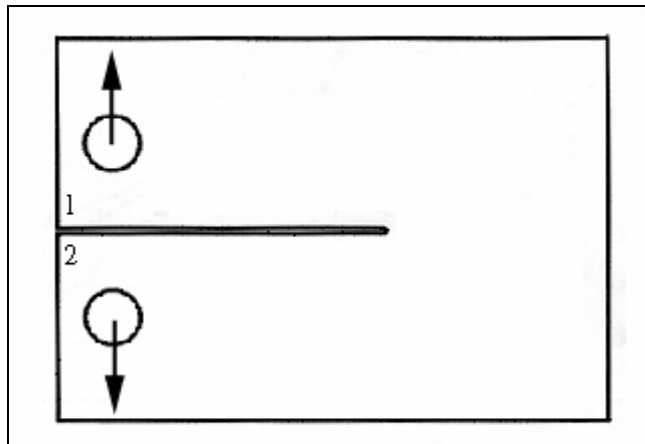


Figure 7. Compact tension sample used to run the dissipated energy density method [7]

Figure 8 contains the experimental dissipated energy curve and the predicted dissipated energy curve.

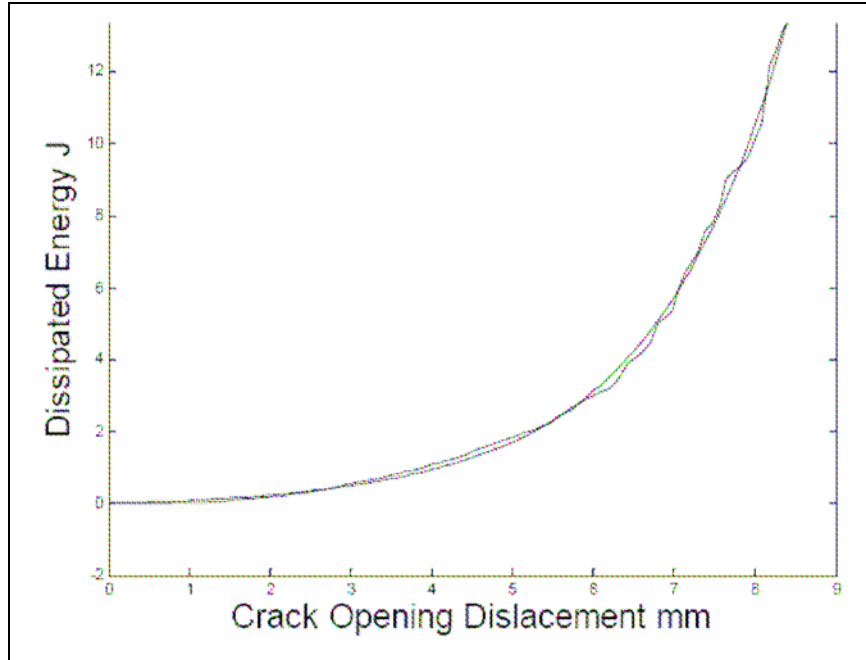


Figure 8. Experimental and predicted crack tip opening displacement on a compact tension sample using the DED method [7]

The results are very good and show promise in the method. The IPL can be a great tool in performing this analysis given the combinations of boundary displacements it can apply to one sample of material.

#### Other Uses of Energy Methods in Predicting Failure in Composites

##### Normalized Difference in Recoverable Energy (NDRE) [7]

A problem that becomes apparent in applying the dissipated energy density method to failure is that the different loading combinations used to acquire empirical data produce dissipated energy curves that vary in magnitude from one to the other. This is shown in Figure 9. The dissipated energy data is taken from tests on the IPL for seven different loading combinations.

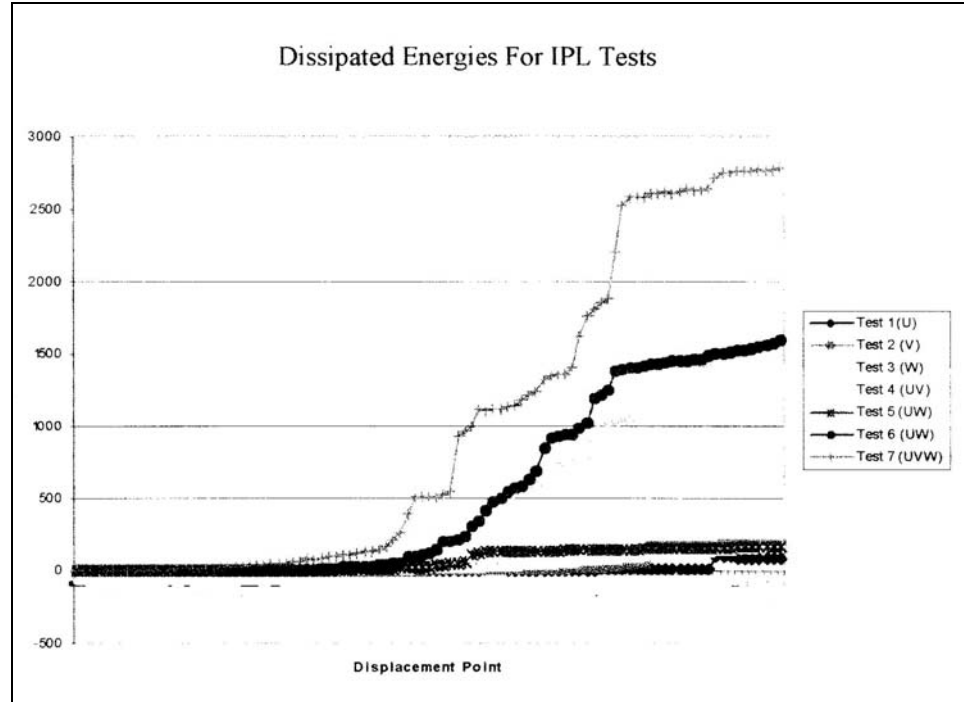


Figure 9. Dissipated energy test data from the IPL for seven different loading combinations [7]

The magnitude of dissipated energy varies widely from test to test. Using the DED method described would be problematic for this reason. Ritter [7] has proposed a different energy metric that normalizes the difference between the theoretical recoverable energy and the actual recoverable energy by the theoretical recoverable energy in a test sample. (The details are omitted here but a complete description is given in [7]). The same test data is shown in Figure 10 after being transformed into NDRE.

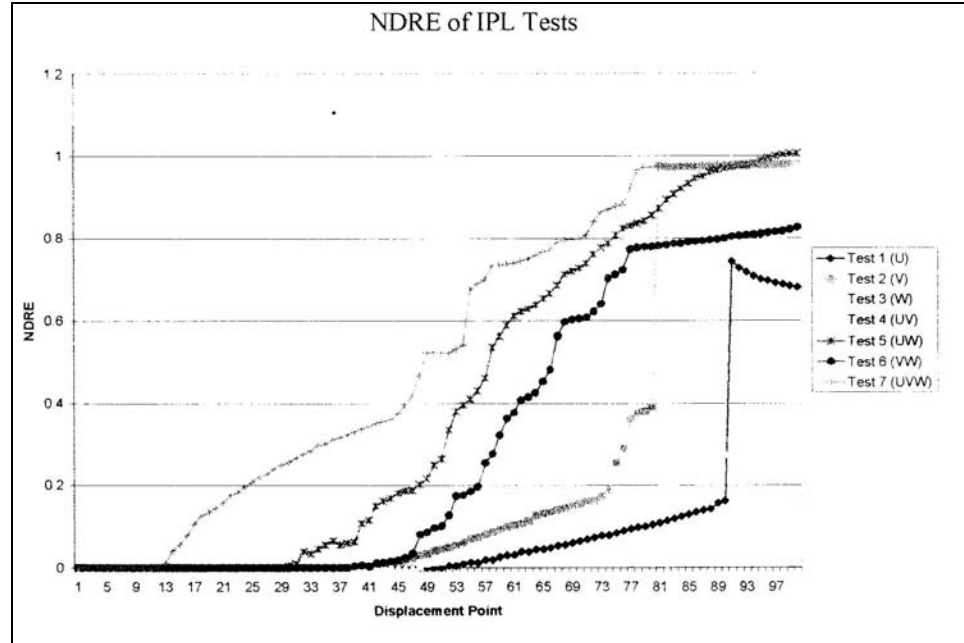


Figure 10. NDRE test data from the IPL for 7 different loading combinations [7]

The difference in magnitudes is much less severe after applying the NDRE to the test data. This energy parameter can be used in much the same way as DED to predict composite failure. The DED function from Equation 1 (and subsequent equations) can be replaced by an NDRE function.

#### Obtaining Material Properties in the Inelastic Region

A method currently under investigation at MSU is a procedure to update a material's properties as it experiences inelastic deformation. The approach is similar to the DED method. Instead of obtaining a dissipated energy function as a function of elastic strain, total strain energy is obtained as a function of elastic strain. In Equation 1,  $\Phi$  can be replaced by total strain energy. Once a map of total strain energy is obtained for a material using a FE model, the elastic modulus and Poisson's ratio can be derived. These material properties are then updated along the load displacement curve as linear

elastic strain states are mapped according to experimental data into non-linear strain states. This method also requires many experimental data points, which can be accommodated by the IPL.

### Validation of Damage Initiation and Progressive Damage Theories

There are many composite failure theories that have been proposed for composite materials. Swanson [2] describes the general procedure thus:

1. The elastic analysis of a laminate is performed which gives an overall strain state for the laminate.
2. This strain state can then be apportioned to the strains in the individual plies.
3. The ply strains are transformed into the direction of the ply fibers, which can then yield the stresses in the ply with reference to the ply fiber direction.
4. Failure can be estimated by comparing the ply strains and stresses to allowable values.

Most failure theories have been adapted from failure methods of materials other than composites and thus do not take into account two distinct mechanisms of failure in composites: matrix failure and fiber failure. This renders them inadequate according to Swanson [2] for predicting failure in composite materials. Failure theories that do work are therefore those that differentiate between the matrix and fiber failure. Tsai and Wu [8]; Hahn, Erikson, and Tsai [9]; and Hashin [10] have offered theories that do this and predict failure fairly accurately for certain composite systems [2]. One problem with these theories is that they neglect the strength afforded the laminate from adjacent plies although it has been suggested that the ply strength can be adjusted for this “in-situ”

effect. Accounting for the additional strength due to adjacent plies as well as the interaction between fiber and matrix requires an energy release method of laminate failure. Fracture mechanics describes the matrix cracking and three dimensional elastic analysis describes the fiber strength. This obviously becomes more complex.

Overall, failure theories are well accompanied by empirical data in order to validate their predictions. The IPL could be very useful for this task since it can produce multiple loading conditions in one test. Compression loading failure predictions could greatly benefit from easily obtained empirical data since compression failure is much more difficult to predict than tensile or shear failure.

A related method for using the IPL to predict failure is to establish a database of strain or stress allowable values for a composite system. Several tests are done on the IPL with different loading conditions and material architectures. FEA is run to get the element stresses and strains in the tested coupon. A correlation function is made similar to Equation 1 between the FEA derived values and the empirical data. This is then used with other geometries using a finite element model to predict failure.

### Obtaining Material Properties

Huang [11] has introduced a method of using the IPL to obtain macromechanical composite material properties using the properties of the constituents: fiber and matrix. Transversely isotropic materials have five unique material constants:  $E_1$ ,  $E_2$ ,  $\nu_{12}$ ,  $G_{12}$ , and  $G_{23}$ . To find these properties for a laminate, the following procedure is used:

1. Material properties of the individual components of a composite (fiber and matrix) are known through testing these raw materials. These are

micromechanical properties of the laminate (as opposed to macromechanical properties which would be the properties of the fiber and matrix together in the ply).

2. Micromechanical analysis is conducted to establish the bounds of the ply properties from the properties of the individual components. The six known parameters are: elastic modulus of the fiber, Poisson's ratio of the fiber, volume fiber fraction of the fiber, and three similar parameters for the matrix.  $E_1$  is found through the rule of mixtures [2][11].  $E_2$  is found using the Halpin-Tsai formulation [2][11].  $\nu_{12}$  is found through the rule of mixtures,  $G_{12}$  is found using the periodic microstructure model [11], and  $G_{23}$  is found using the stress-partitioning parameter [11].
3. Empirically derived laminate force and displacement values are obtained through coupon tests on the IPL. Data from different coupon boundary conditions are obtained.
4. FE models are run that simulate the empirical tests on the IPL. The material properties obtained through micromechanical analysis are used as an initial assumption.
5. An optimization scheme is run in the FE code to minimize the difference between the force/displacement (state variables) data from the IPL tests and the FE model. The five material properties are used as the design variables (the variables that are changed during optimization). This then gives the five optimized laminate material properties from empirical tests and micromechanical analysis.

## CHAPTER 3

### FIRST GENERATION IPL CHARACTERISTICS AND FEATURES

The IPL has gone through several modifications since its inception by the senior design group mentioned previously. These modifications fit into two main generations of the IPL. The validation studies presented in this thesis are on the second generation modifications. This chapter describes the state of the IPL after its first generation to illuminate the progress of the IPL and to more fully realize the quantity of work that has gone into the first generation described in this chapter as well as the second generation described in Chapter 4.

#### Frame

A picture of the first generation IPL is shown in Figure 11. It was positioned horizontally on a table with the larger frame piece rigidly attached to the table and the smaller frame piece allowed to roll via ball casters on a metal sheet.

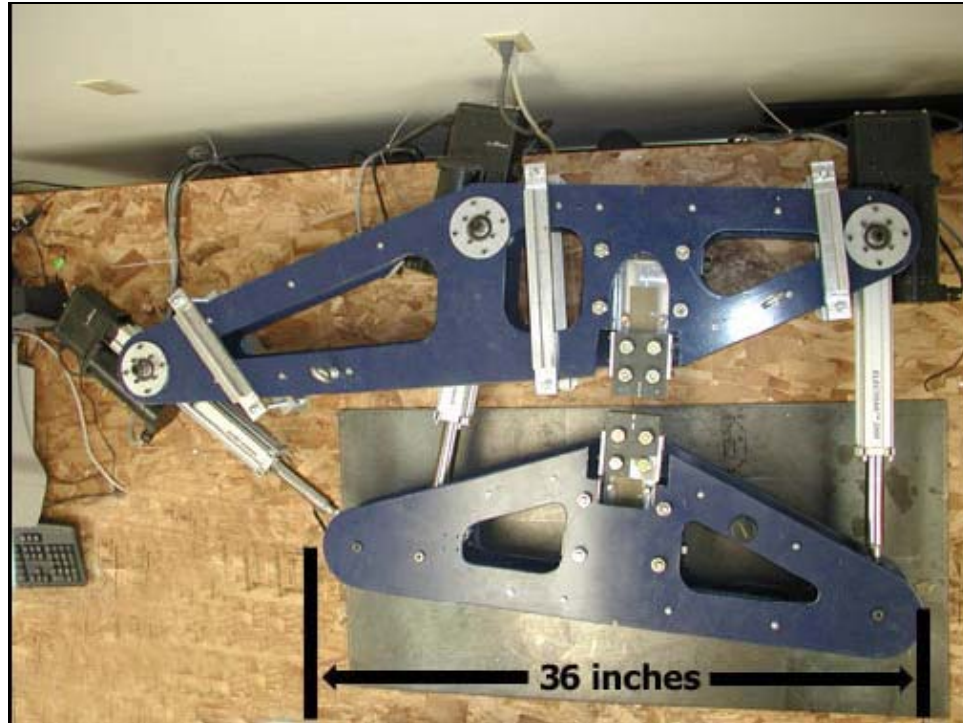


Figure 11. First generation IPL [7]

The IPL has subsequently been mounted vertically with the larger frame section mounted below the smaller frame section.

### Actuators

The actuators were attached to the larger frame piece via cylindrical roller bearings. This type of bearing allowed some play in the movement of the IPL. Since the displacement of the IPL was recorded by the actuators, the play between the actuators and frame was a factor in test data. The data in Figure 12 shows how the play affected the initial portion of the test data.

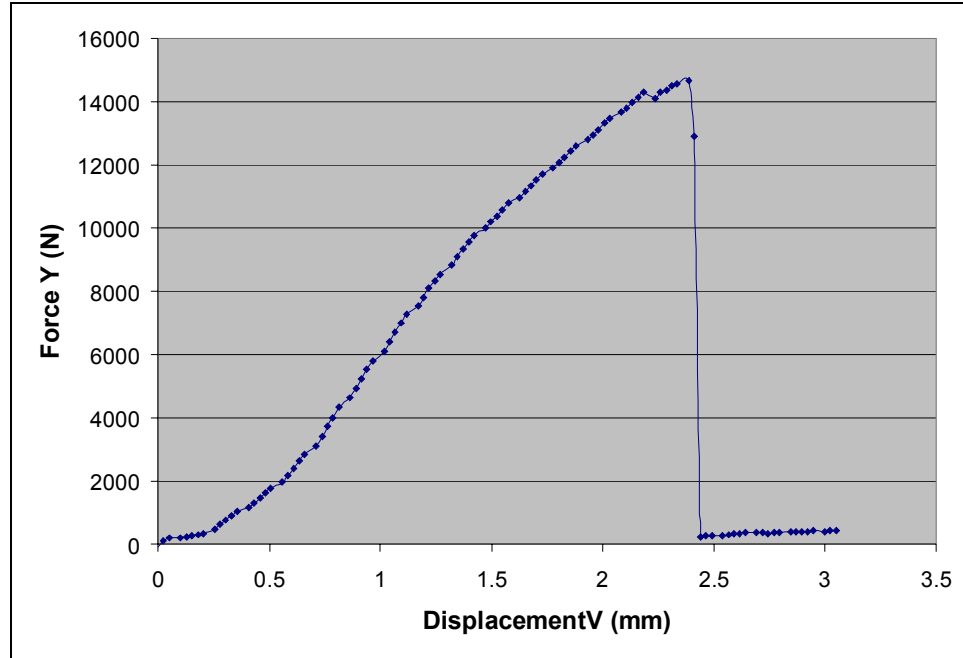


Figure 12. Tension test data on first generation IPL with play in the initial part of the elastic curve

The bearings were replaced with tapered roller bearings to eliminate the play between the actuators and the frame.

### Actuator Kinematics

The kinematic program that output how many steps each actuator should take for each move was run using Maple math software (Waterloo Maple Inc.) which output a text file which the Labview program then read into its “move” function (a sub VI). For each different combination of displacement boundary conditions for a test, the Maple program had to be run. This was replaced by a Matlab script inside Labview. It was only necessary to interact with the Labview program thereafter to specify the desired boundary displacements for a test.

### Grips

The former grips are shown in Figure 13. They function by clamping two 25.4 mm thick steel plates together via the eight bolts shown. The grip faces are attached to the inside surfaces of the steel plates.

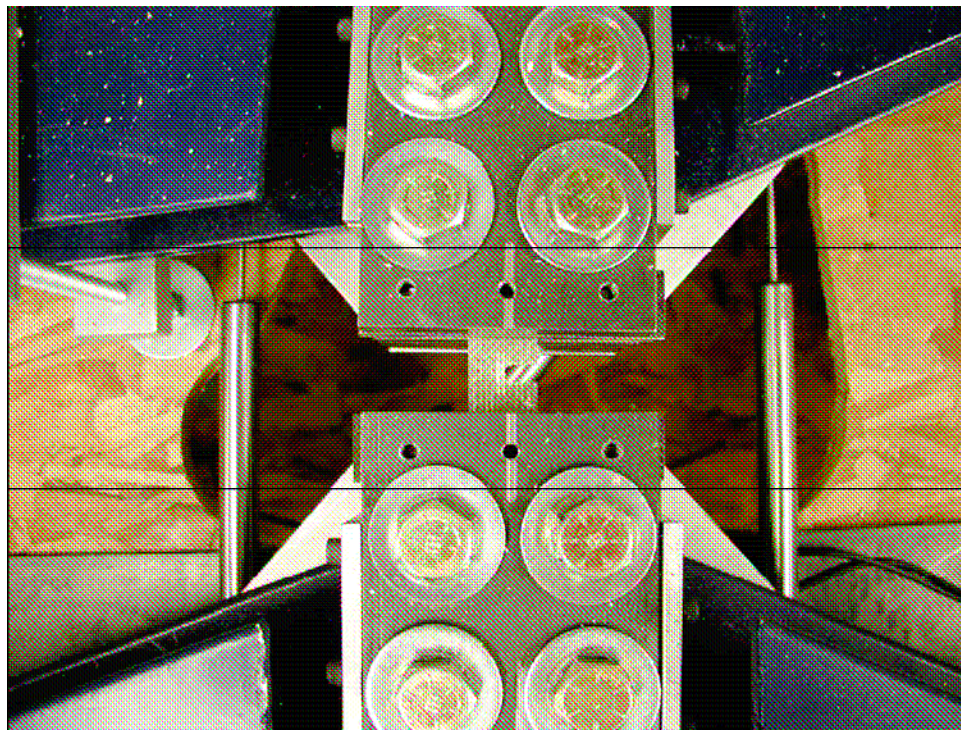


Figure 13. First generation IPL grips [7]

These grips were replaced by the ones described in Chapter 4 for a few reasons.

1. These grips did not keep the sample centered in the IPL because one of the steel plates was rigidly attached to the frame of the IPL and the other was attached to it via the eight bolts shown. Differing sample thicknesses altered the location of the center of the sample in the thickness dimension of the IPL. In other words, the sample was offset from the line-of-action of the actuators and therefore produced out-of-plane bending of the IPL. This was resolved by making self-centering

grips. This involved completely redesigning the grips and making them hydraulically actuated.

2. The grips started to permanently deform around the sample after being tightened repeatedly since the line-of-action of clamping force from the bolts was not in line with the sample. The old grips were replaced by machining vises which had the gripping actuator screw positioned in line with the sample. These vises are similar to ones used on milling machines for clamping the work piece.
3. The grip surfaces were only about 25 mm wide. This was too narrow to allow full gripping of the sample. The grip faces were changed to be 38 mm wide.

#### Displacement Acquisition

The actuators were initially used for position control as well as displacement acquisition. These proved to flex a lot as did the frame and all connecting mechanisms between the actuators and the grips. The LVDTs were added for displacement acquisition and were transferred to each different grip setup that was tried. The LVDTs were eventually implemented for position control by updating the position read by the actuators with the position read by the LVDTs.

#### Other Features

The loads were acquired in the same manner as they are with the second generation IPL. The third generation IPL has implemented new load cell amplifiers and changed the loads acquisition to 16 bit from 12 bit.

Out-of-plane constraining on the first generation IPL was accomplished by positioning the IPL horizontal to allow gravity to keep the smaller frame from deflecting out-of-plane. Compression tests still did not stay in-plane however and since the grips did not center the sample in the IPL, out-of-plane deflection on shear and tension tests was present.

## CHAPTER 4

## COMPONENTS OF THE IPL

This chapter describes the second generation IPL. The main components of the IPL are the frame, actuators, grips, out-of-plane constrainer, load acquisition system, and displacement acquisition system. Figure 1 is repeated here for clarity.

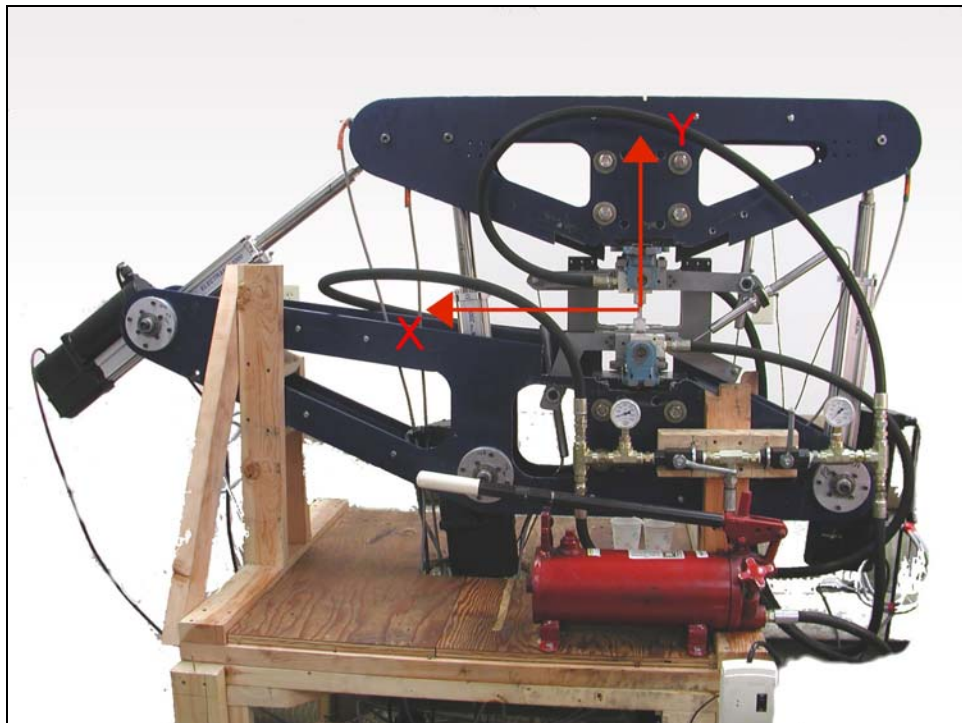


Figure 14. The Montana State University second generation In-Plane Loader

Frame

The frame of the IPL is divided into two separate frame sections: upper and lower. The reference coordinate system is located directly between the two frames with  $x$

to the left,  $y$  up, and  $z$  into the page. This coordinate system stays in the center of the machine at all times. Thus, kinematically, the two frames move opposite each other. With respect to the table, the lower frame is fixed and the upper frame moves with respect to the lower frame. The frame is 10.8 cm wide in the  $z$  direction and is made of 6.35 mm thick steel plate, which sandwiches 9.5 cm spacers. Mounting blocks are sandwiched between the steel plates to hold each end of the actuators and the grips.

### Actuators

#### Hardware

Three stepper motor driven ball screw actuators (Warner Linear Electrak 2000 BP9305-B5512-TIB) move the upper frame with respect to the lower frame. An encoder attached to the motor gives position control to 0.000508 mm accuracy (50000 steps = 25.4 mm). The maximum rated load for the actuators is 8900 N. The actuators are attached to the frame via bearing block pivot points on both the upper and lower frames (Figure 15).

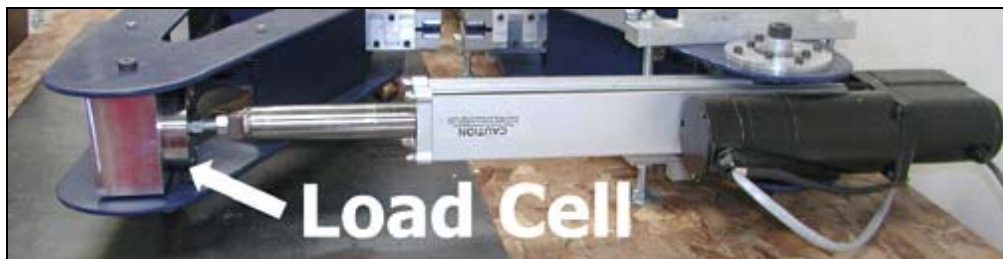


Figure 15. Actuator, load cell, and pivot block on the IPL [7]

The actuators are positioned at non-orthogonal angles to each other to prevent any kinematic constraints. Each actuator can thus move independently of the others without binding.

### Control and Data Acquisition

The actuators are powered and driven by Superior Electric SLO-SYN SS2000D6 Packaged Drives. Data acquisition and control is accomplished via a National Instruments UMI-7764 Accessory, which is tailored to control stepper and servo motors. The UMI Accessory is connected to a National Instruments PCI-7344 12 bit Controller mounted in the computer. National Instruments Labview 7 [12] provides the user interface for controlling the actuators. The kinematic program to resolve the individual actuator extensions or retractions into  $u$ ,  $v$ , and  $\omega$  is run in a Mathworks Matlab [13] script embedded in Labview.

### Kinematics

The schematic in Figure 16 shows the vector configuration of the actuator pivot points with respect to the IPL coordinate system.

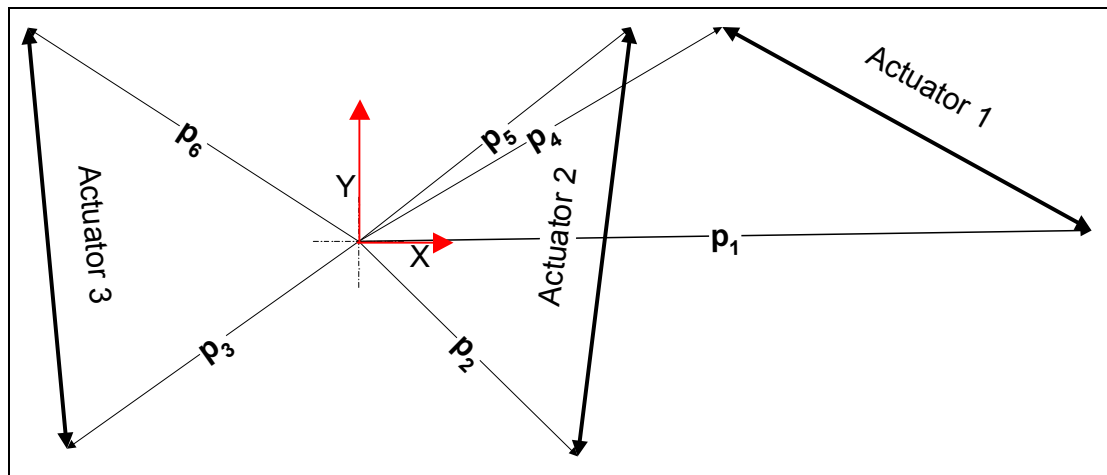


Figure 16. Vector schematic of the actuator positions on the IPL

The origin of the coordinate system in Figure 16 is physically located half way between the grips. This corresponds to the center point of a sample to be tested. The vectors  $p_1$ - $p_6$

locate the pivot points of the actuators. The actuators are controlled by specifying the number of steps each must take. This means finding the length of each actuator for a desired displacement ( $u$ ,  $v$ , and  $\omega$ ) of the IPL. This is done by adding the desired displacement vector  $ui+vj$  to each position vector  $p_1-p_6$  and adding the desired rotation  $\omega$  to the angle each position vector makes with the  $x$  axis. The actuator lengths after a specified displacement can then be determined via vector arithmetic. This is then converted into the number of steps each actuator must take given that 25.4 mm=50000 steps. The Matlab program is found in Appendix B.

### Test Program

A test on the IPL is run for a user-specified number of moves, which also specifies the number of data points that will be acquired during the test. Each move is calculated by dividing the total displacement in each direction ( $u$ ,  $v$ , and  $\omega$ ) by the number of moves. For example, if a test is to be run for  $u=0.2''$ ,  $v=.2''$ , and  $\omega=5^\circ$ , and the number of data points desired is 10, then the first move moves to  $u=0.02''$ ,  $v=0.02''$ , and  $\omega=0.5^\circ$ . During the test, the IPL moves to the first data point location, stops, records load and displacement data then continues to the next step. This is done to increase the accuracy of both load and displacement data collection since several data points of each can be acquired and averaged while the IPL is stopped. It also helps implement a feedback loop, which will be discussed later. The Labview code is found in Appendix A.

### Grips

The picture in Figure 17 shows the top and bottom grip assemblies.

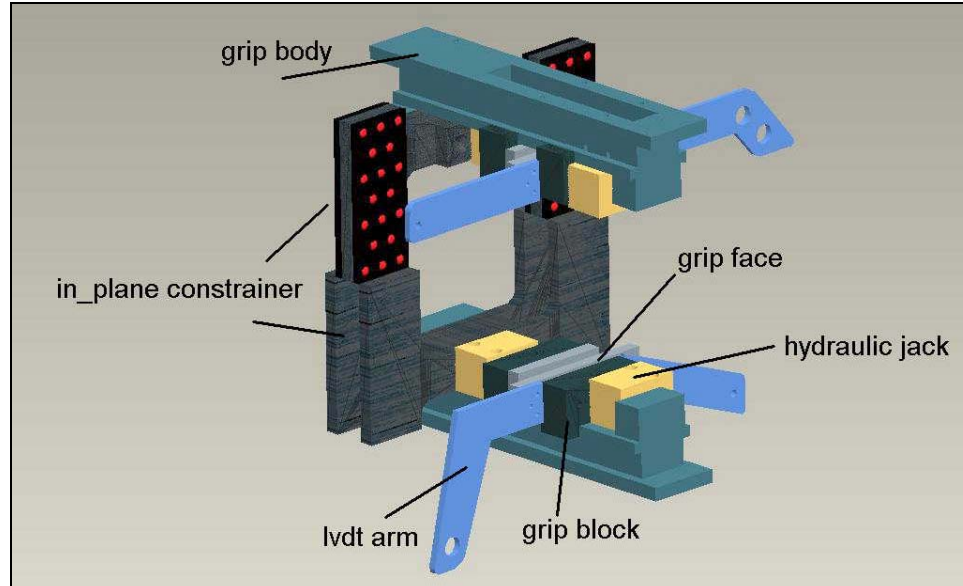


Figure 17. Grip assembly without LVDTs attached to the LVDT arms

The grip body sandwiches the rest of the grip components and provides a reaction force to the gripping forces. The hydraulic jacks (Ram-Pac RC-5-LP-.5S) are sandwiched between the grip body and the grip blocks. The piston from the jack pushes the grip block to which is attached the grip face. The sample is inserted between the grip faces. The hydraulic jacks receive pressure from the hydraulic hand pump (Prince PM-HP\_10B) of maximum 20.7 MPa. The samples have a gripping surface of around  $6.45 \text{ cm}^2$  so the gripping force can be a maximum of 13,340 N. This is enough force to grip soft steels.

It is imperative that the sample be centered about the  $x$ - $y$  plane of the IPL, otherwise, the upper frame bends out of plane of the lower frame with applied loads. The hydraulic system is set up such that a force applied against one of the pistons causes fluid to leave that piston and extend the opposing piston. This causes the sample to be off center from the center line of the IPL. It is thus necessary for the grips to be self-centering about the  $x$ - $y$  plane. This is accomplished by a rack and pinion gear mechanism

located in the grip body as shown in Figure 18. As one grip block is moved, its attached rack gear turns the pinion gear, which in turn causes the opposing grip to move in the opposite direction via its rack gear.

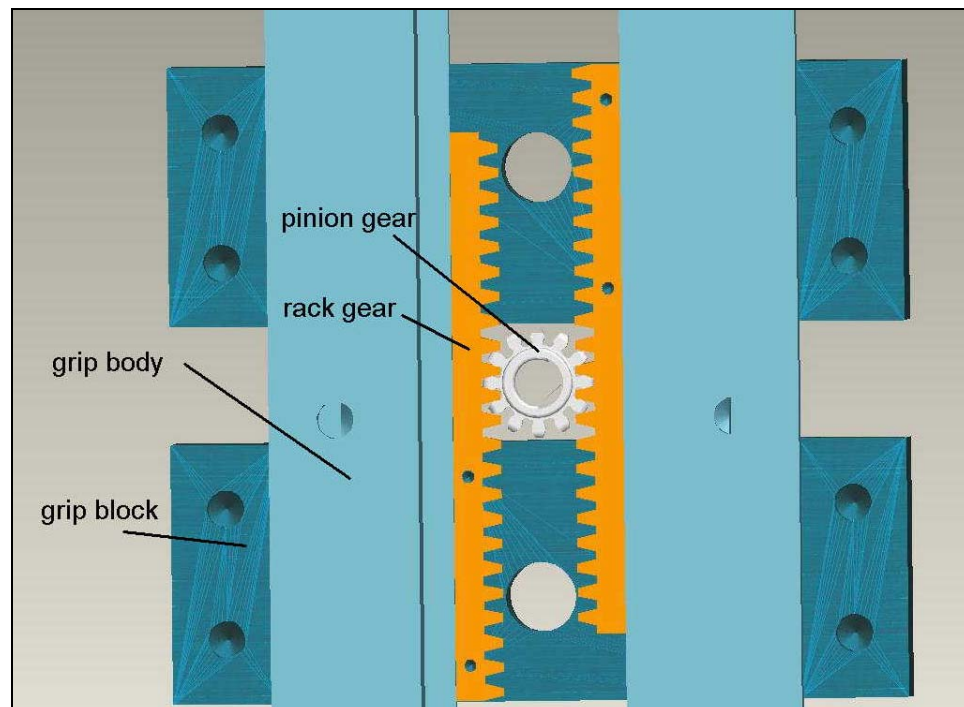


Figure 18. Assembly of the rack and pinion gears mounted to the grip body and grip blocks

The grip blocks are held securely to the grip body by grip block constraining bars attached to each side of the grip blocks. After the sample is gripped, a bolt is tightened that holds the grip block down to the grip body (Figure 19).

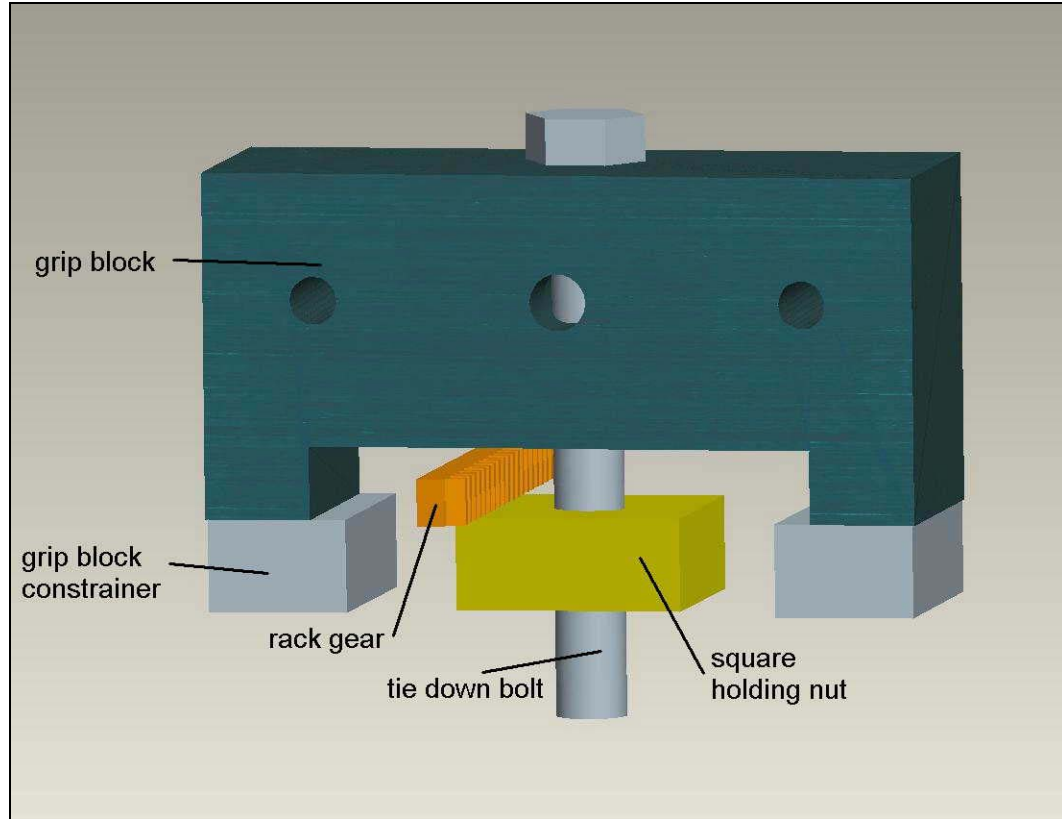


Figure 19. Assembly of the grip block showing the tie down bolt, rack gear, and grip block constrainters (grip body is not shown)

### Out-of-plane Constrainer

A tongue-in-groove connector between the top and bottom of the IPL prevents the IPL frames from moving out of plane with respect to each other (Figure 17). This is especially important when doing compression tests to prevent buckling of the sample. The upper and lower pieces of the out-of-plane constrainer are attached to their respective grip bodies. Ball bearing plates attached to the upper out-of-plane constrainer plates ride in between the lower out-of-plane constrainer plates to decrease friction.

### Load Acquisition System

### Load Cells, Hardware, and Data Acquisition

Load data is acquired via three Omegadyne LCHD-2K pancake load cells attached to the upper ends of each of the actuators (Figure 15). This makes the load vector parallel to the actuators and enables the loads to be resolved into  $x$  and  $y$  components. The load cells do not have to be located near the sample because force equilibrium ensures that the load cells read the reaction force from the sample as long as there is not significant friction or other force dissipative mechanisms along the way. The load cells are powered by an Agilent E3610A power supply set to 10 volts. Data is acquired from the load cells via the National Instruments UMI Accessory, which has extra modules for attaching peripheral devices other than the servo and stepper motor devices.

The load cells rated sensitivity is 3 mV output voltage per volt of input voltage. The input voltage is 10 volts which gives 30 mV full-scale output voltage.. The maximum input voltage into the UMI board is 10 volts. The UMI board converts the analog signal to 12 bit digital which gives a resolution of 4.88 mV/bin if all 10 volts of input voltage is used. If only 30 mV are used then the load resolution is 1414 N. To increase the resolution, an amplifying circuit was built for each load cell, which amplifies the signal before being read by the UMI board. A second power supply (Extech 382213) set to  $\pm 12$  volts powers the amplifier.

### Resolving Loads into Components

Each actuator must have a load cell somewhere along its line of action. This means that three load cells are required on the IPL. They are located on the ends of the

actuators and make the connection between the actuator and the upper frame. They are numbered according to the actuator to which they are attached: i.e. load cell 1, 2, and 3 (reference Figure 16). The force each load cell reads can be resolved to give three directional loads:  $F_x$ ,  $F_y$ , and  $M_z$ . To get  $F_x$  or  $F_y$  for each actuator, the magnitude of the force is multiplied by the cosine or sine of the angle (respectively) the actuator makes with the  $x$ -axis (Figure 16). The force components of each actuator are then summed to get the total  $F_x$  and  $F_y$ .  $M_z$  for each actuator is calculated by taking the cross product of each moment arm (measured from the origin of the IPL to any point on the actuator) with each force vector. The total  $M_z$  is obtained by summing the three moments. Matlab script called from Labview is used to resolve the loads into direction components (Appendix B).

#### Frictional Loads and Load Offset Files

The out-of-plane constrainer adds some frictional forces to the movement of the IPL due to the upper out-of-plane constrainer plate sliding in between the lower out-of-plane constrainer plates. The bearing plates are designed to minimize this friction. The bearing plates are attached to the top out-of-plane constrainer plate via two bolts. Each of these bolts connects the bearing plates on the front and back side to each other through a hole in the out-of-plane constrainer plate. Rigidly attaching the bearing plates to the upper out-of-plane constrainer plates would cause the ball bearings to slide across both surfaces instead of roll. To facilitate rolling action of the ball bearings, the holes in the upper out-of-plane constrainer plate are larger than the bolts that hold the bearing plates in place. This leaves some room for the ball bearings to roll before the bolts contact the

edge of the hole and the ball bearings have to slide. The holes are 12.7 mm in diameter and the bolts that hold the bearing plates together are 5.08 mm in diameter (Figure 20). This leaves 15.24 mm of play before the movement of the IPL forces the bearing plates to slide across the surface of the lower out-of-plane constrainer instead of roll. (15.24 mm is two times the gap distance between the bolt and the hole. When rolling, the bearing plate only moves half as much as either plate between which it is sandwiched).

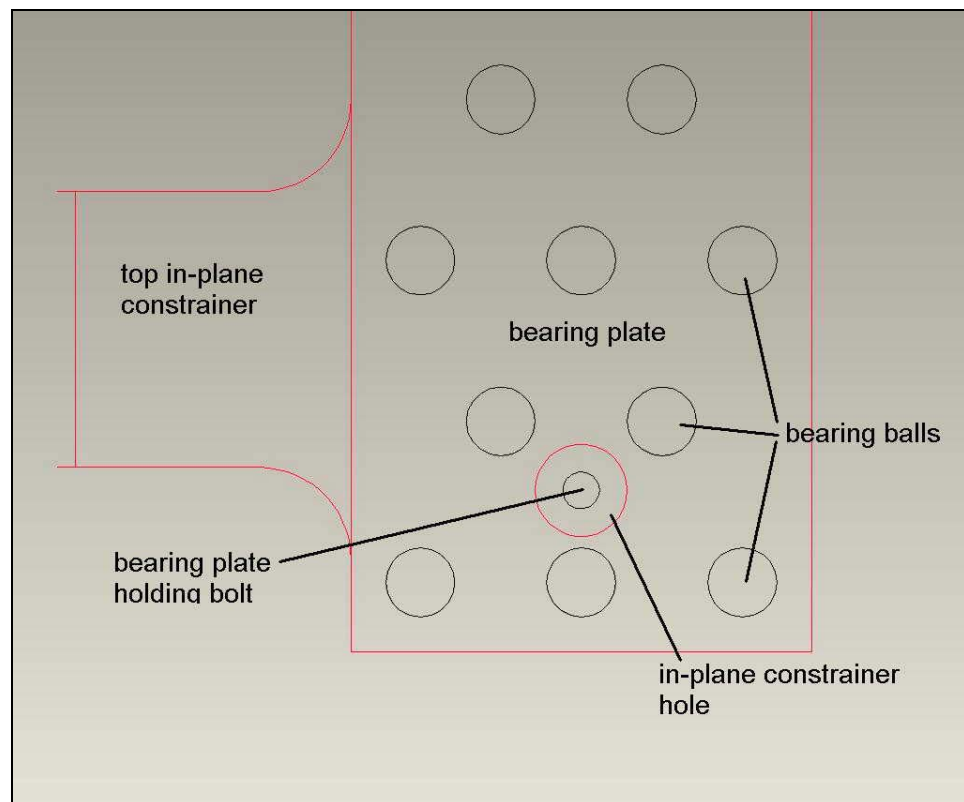


Figure 20. Diagram showing the loose fit of the bearing plates to the top in plane constrainer plate

Figure 21 contains a force versus displacement curve of the IPL with no sample. The force ranges from 60 N to 100 N between 2 mm and 13 mm of displacement. This is the force reading due to rolling friction (not the actual force since the load cells are not zeroed at this point). From about 13 to 18 mm of displacement, the force jumps about

110 N to over 200 N where it remains. This is due to sliding friction. In an actual test, 13 mm is quite a large displacement; therefore, sliding friction is probably not going to take place in a normal test.

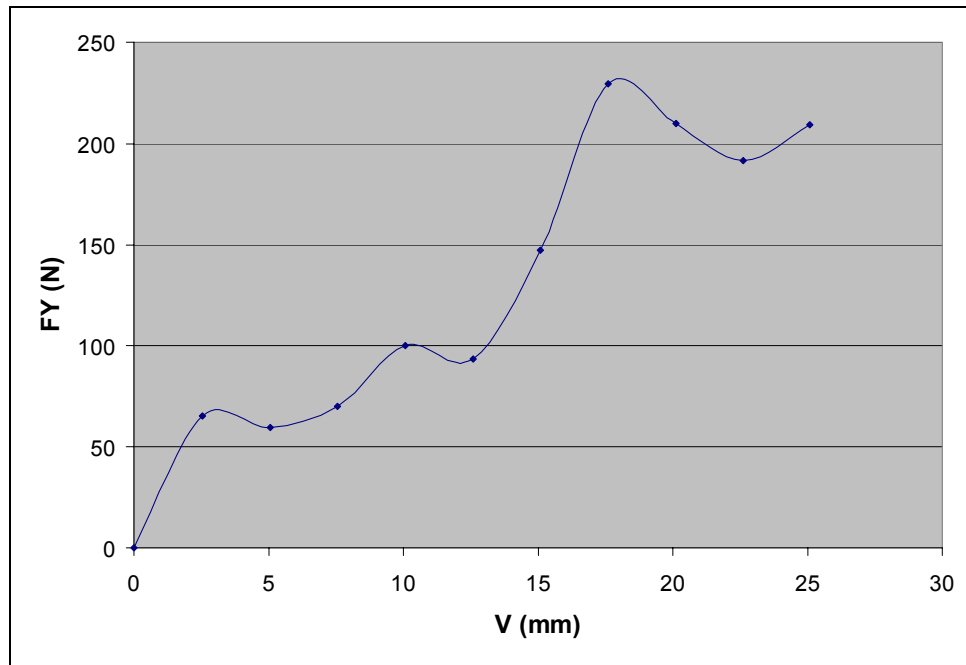


Figure 21.  $F_y$  versus  $v$  curve with no sample

In Figure 21, there is no additional loading on the IPL other than the weight of the upper frame and the friction between the out-of-plane constrainer plates. The program of the IPL allows the friction loads and frame weight to be subtracted from loads due to sample reactions. This is accomplished by running a test without a sample loaded, storing that data file, and then calling that data file while a test with a sample is being run and subtracting the loads. This also zeroes initial gripping loads since a load-zeroing scheme cannot be run as it can on uni-axial testing machines due to the kinematic complexity of trying to zero  $F_x$ ,  $F_y$ , and  $M_z$  loads simultaneously while keeping the sample from being displaced.

## Displacement Acquisition System

### LVDTs

Displacement data are acquired with linear variable differential transducers or LVDTs. These are used instead of the actuator encoders to measure displacement because there is a lot of flex in the IPL between the location of the encoders and the sample. Flex happens in the ball screws in the actuators, the frame of the IPL, the grips, and the joints holding it all together. All of these flexures store elastic strain energy which presents displacement control problems. This will be discussed later. Figure 22 shows a force-displacement curve of a tension test with one curve measuring displacement with the actuators and the other curve measuring displacement with LVDTs mounted to the grips.

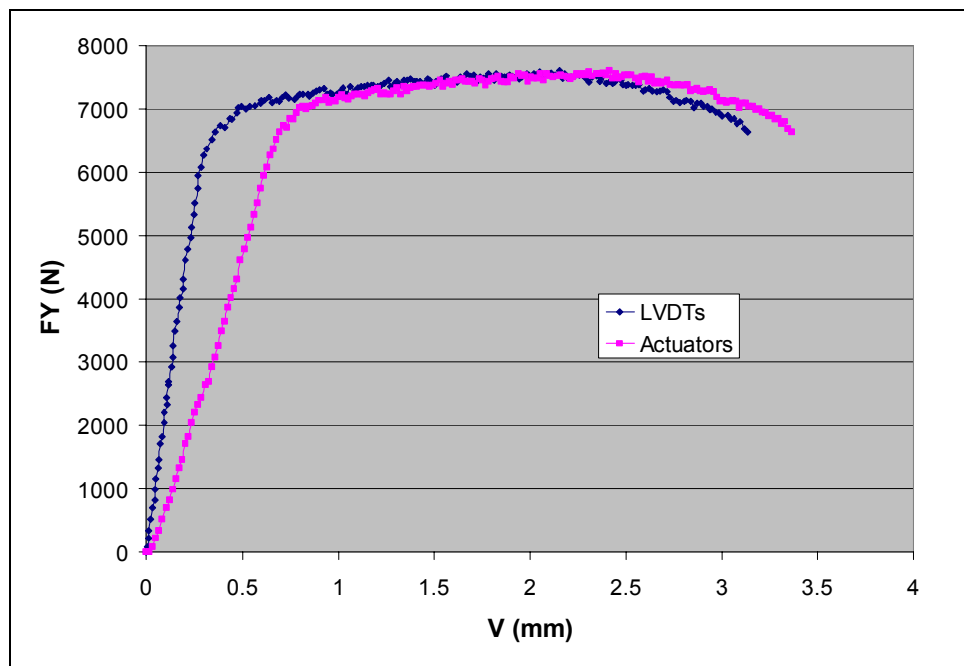


Figure 22.  $F_y/v$  curve with displacement measured by the LVDTs and the actuators

The actuator displacement measurements show a 52% softer constitutive material response than the LVDTs. Attaching strain gauges or some other sample-mounted displacement sensor is impractical, cumbersome, and expensive given the combination of displacements possible with the IPL. Any sample mounted displacement recorder would have to be able to detect the three motions of the IPL. It would also defeat the original goal of obtaining extensive, low cost and low labor data. Figure 23 is a picture of the LVDTs mounted to the grip assembly.

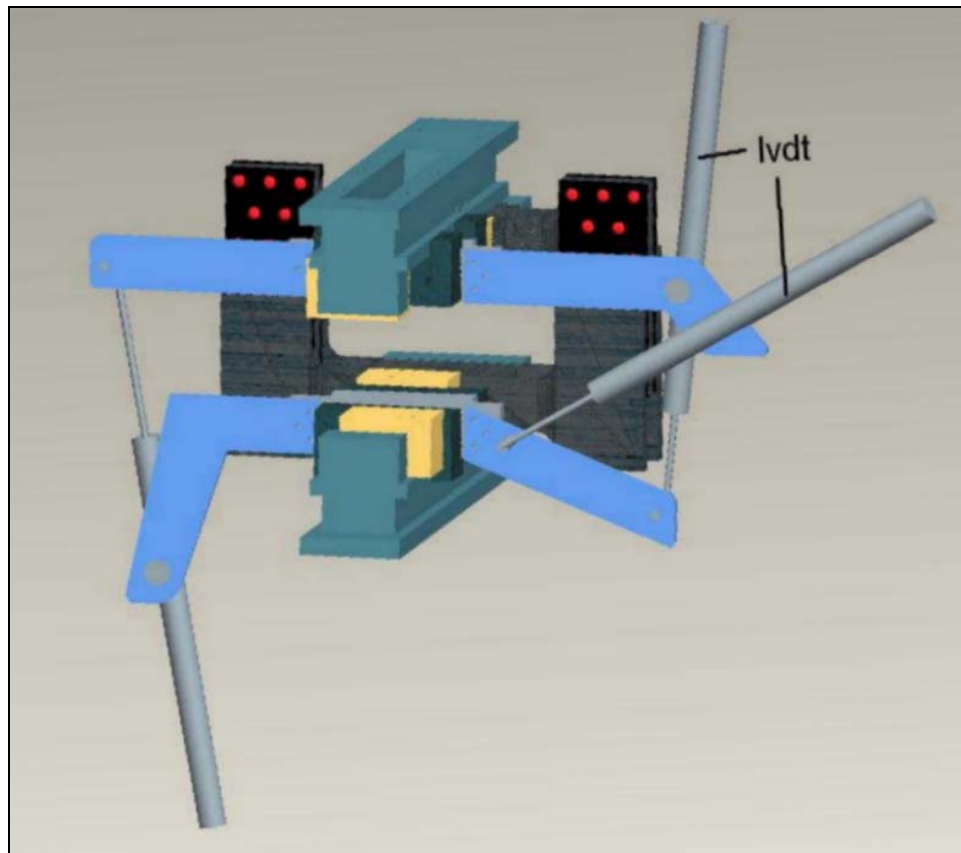


Figure 23. IPL grip assembly with LVDTs

The LVDTs are attached to the  $-z$  grips via the LVDT arms.

### LVDT Kinematics

The displacements  $u$ ,  $v$ , and  $\omega$  are derived from the lengths of the LVDTs by three vector loop equations shown in Figure 24.

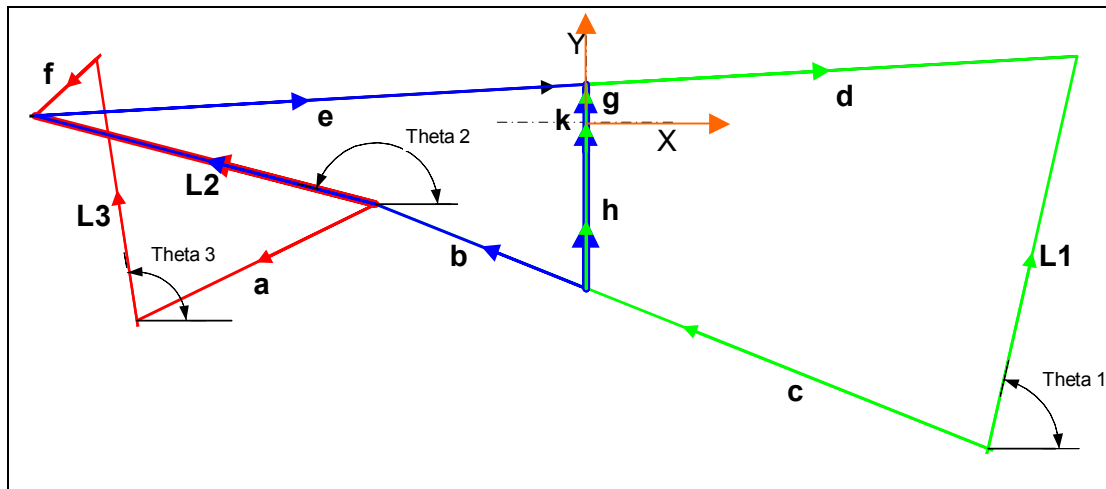


Figure 24. Vector schematic of the LVDTs

The  $L$  vectors represent the LVDTs. The components of  $k$  are  $u$  and  $v$  (measured between the center points of the top and bottom grips).  $\omega$  is the angle  $k$  makes with the  $y$  axis of the IPL. Vectors  $a$ ,  $b$ ,  $c$ , and  $h$  are rigidly connected to each other and represent the physical configuration of the LVDTs.  $h$  is always in line with the  $y$  axis of the IPL and its distal end is located on the top edge of the bottom grip face.  $b$  and  $c$  are always parallel to each other. Vectors  $e$ ,  $f$ ,  $g$ , and  $d$  are also rigidly connected to each other. The proximal end of  $g$  is located on the bottom edge of the top grip face.  $e$  is always parallel to  $d$  and the combination of  $f$ ,  $g$ ,  $d$ , and  $e$  move with respect to  $a$ ,  $b$ ,  $c$ , and  $h$  by a change in  $k$ . In contrast to the kinematics of the actuators, the LVDT kinematic schematic assumes that the lower frame of the IPL is fixed and the upper frame moves. Therefore, vectors  $c$ ,  $b$ ,  $a$ , and  $h$  are completely specified by their  $x$  and  $y$  components whereas vectors  $L1$ ,  $d$ ,  $g$ ,  $e$ ,  $f$ ,  $L2$ , and  $L3$  are only known by their lengths. The lengths are

resolved into  $x$  and  $y$  components by using the angles that the LVDTs make with the positive  $x$  axis:  $\theta_1$ ,  $\theta_2$ , and  $\theta_3$ . The vector loop equations are then:

$$\text{Green Loop: } L1+c+h+k+g+d=0$$

$$\text{Blue Loop: } b+L2+e-g-k-h=0 \quad . \quad 1$$

$$\text{Red Loop: } a+L3+f-L2=0$$

This provides six equations (two component equations for each vector loop) for six unknowns ( $u$ ,  $v$ ,  $\omega$ , and  $\theta_1$ ,  $\theta_2$ , and  $\theta_3$ ). To solve this system of non-linear equations, Matlab's numerical non-linear equation solver *fsolve* is used. This is run in a Matlab script in Labview (Appendix B).

To facilitate different gage lengths (different initial distances between grips) on the IPL, the initial LVDT lengths are the variables in the set of vector loop equations ( $L1$ ,  $L2$ , and  $L3$ ) along with the angles the LVDTs make with the  $x$ -axis. The  $k$  vector, or  $u$ ,  $v$ , and  $\omega$ , is set to (0, gage length, 0). This set of equations is solved with the IPL in its initial configuration before a move is made. These initial lengths of the LVDTs are stored for the rest of the test and subsequent LVDT lengths are referenced from them.

Measuring the locations of the pivot points has been problematic. A digitizer arm was initially used but the accuracy was not good enough. Calipers, straight edges, and machinist squares are used currently. The accuracy of this method is questionable.

### Position Control

Another problem that arises by using the actuators to acquire displacement data is the use of the actuators to control the position of the IPL. Accurate positioning of the IPL is important. Flex in the IPL makes positioning the IPL inaccurate indeed if the positioning is not controlled. A feedback loop to update position is implemented so that a

move controlled by the actuators is corrected by the LVDTs until a certain minimum difference is reached. This works by the IPL first making a big move to the position of its calculated big move and then making a series of small moves until the specified minimum distance is obtained. The maximum acceptable error is presently set to 10 stepper motor steps per actuator. This corresponds to 0.00508 mm per actuator. Two separate feedback schemes are used: one for the big moves and one for the little moves. The big move scheme is implemented to avoid a scenario where loads are decreasing in a test because the sample has yielded or acquired damaged and the strain energy from the IPL is then released into the sample causing the displacement for a big move to be greater than specified. To correct this problem, the position of the IPL read by the LVDTs before a big move is taken is subtracted from the desired position after the big move. This difference is input as the big move size. A simple subtraction of the LVDT read position from the target position is not possible however. Since the actuators are what move the IPL, all movements must be in terms of the actuator coordinate system (CS). A position read by the LVDTs is the position of the IPL with respect to the LVDT CS. A transformation between the LVDT CS and the actuator CS must therefore take place. The schematic for the vector transformation is shown in Figure 25.

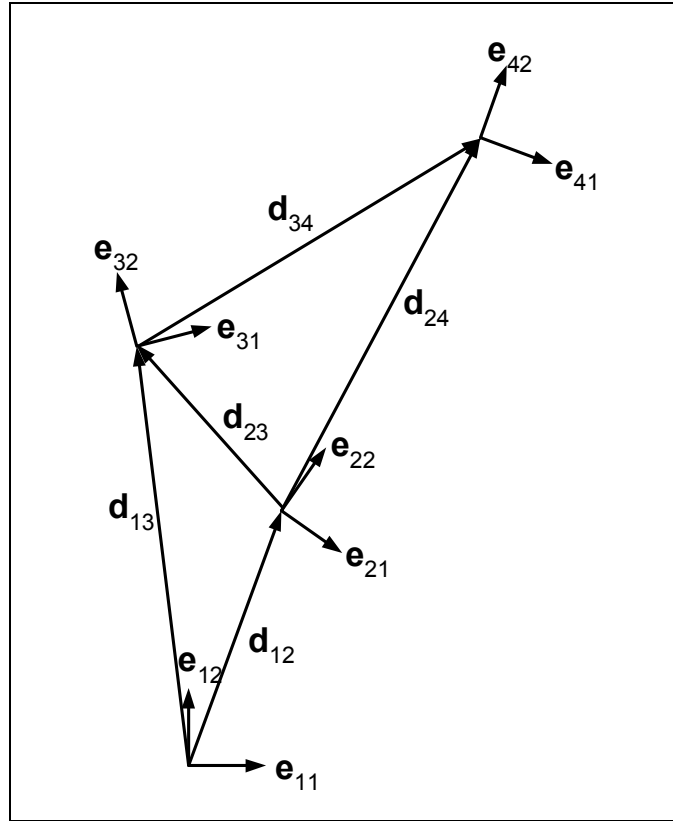


Figure 25. Vector schematic for the feedback loop

The  $e$  vectors represent the basis vectors of the coordinate systems. The first subscript of the  $e$  vectors is the coordinate system number. The second subscript is the first or second base vector. The  $d$  vectors represent a translation from the first subscript CS to the second subscript CS. All CSs are randomly oriented in the figure except where specified. CS 1 is the actuator CS and represents the center point of the IPL centered between the grips (only half of the IPL is shown since the bottom half mirrors the top half). CS 2 is the LVDT CS (with a highly exaggerated offset from CS 1 for illustration purposes). CS 3 is the location of the grip before a big move. CS 4 is the location after a big move. The known quantities are:  ${}^1d_{13}$  (the superscript to the left signifies the reference CS) and  $\theta_{13}$ , which is the position of the grip before any big move with respect to CS 1; and  ${}^2d_{23}$  and

$\theta_{23}$ , which is the grip position read by the LVDTs before any big move.  ${}^2d_{24}$  and  $\theta_{24}$  are the same as  ${}^1d_{13}$  and  $\theta_{13}$  because the LVDTs should read the same as the actuators after a move. The goal of the feedback loop is to minimize  $d_{34}$  and  $d_{12}$ , make  $d_{23}$  equal to  $d_{13}$ , and align  $d_{24}$  with  $d_{13}$ . This is accomplished by finding  ${}^1d_{34}$  and  $\theta_{34}$  through vector algebra and then inputting these quantities into the actuator kinematic program.

The vector schematic for the small move CS transformation is similar to the big move schematic in Figure 25. CS 1 is the actuator CS. CS 2 is the LVDT CS origin. CS 3 is where the grip is located at any time during a small move update. CS 4 is where the grip should end up. Note again that  ${}^2d_{24}$  is the same as  ${}^1d_{13}$  and  $\theta_{24}$  is the same as  $\theta_{13}$ . The known quantities are  ${}^2d_{23}$  and  $\theta_{23}$ , which is what the LVDTs read for any small step, and  ${}^1d_{13}$  and  $\theta_{13}$ , which is what the move specifies. The goal again is to solve for  ${}^1d_{34}$  and  $\theta_{34}$  and is done in the same manner as it is for the big move update. These quantities are then input into the actuator kinematics program. The Matlab code is found in Appendix B.

### Unloading Loop in Feedback

The position feedback from the LVDTs works fine in the elastic region but breaks down in the plastic or material softening region. Figure 26 shows the unloading that happens when the force/displacement curve has a negative slope. When the slope goes negative, the elastic strain energy stored in the IPL must decrease because the loads decrease. This energy is released into the sample causing a proportional increase in sample displacement. This extra displacement is corrected by the LVDT position control

feedback loop by back driving the actuators. The unloading portion of the curve is the result of the displacement decreasing,.

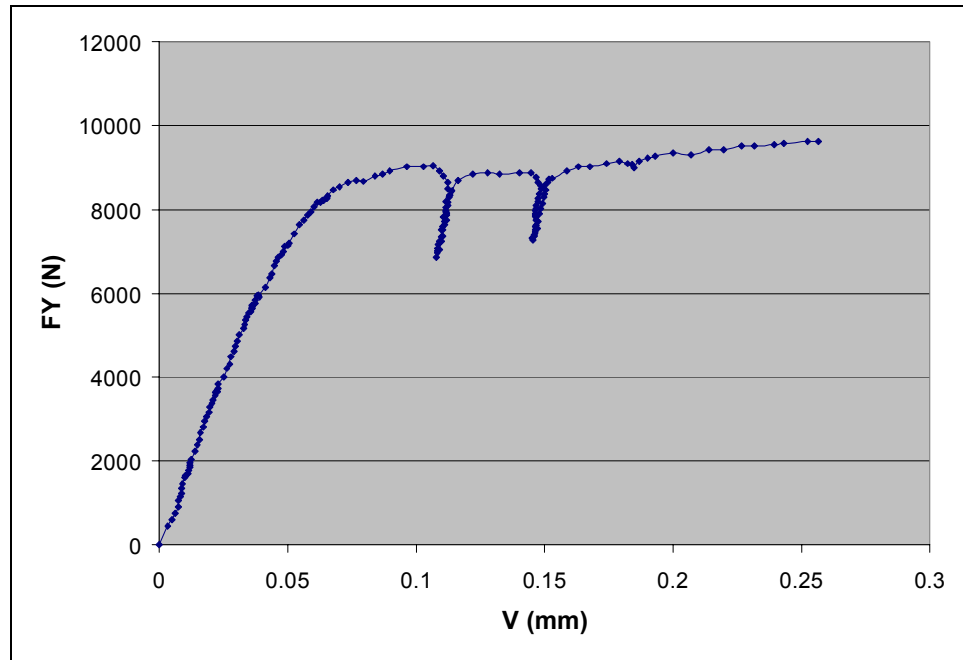


Figure 26.  $F_y/v$  curve with backdrive due to LVDT feedback

This of course is not a desirable feature of the displacement feedback loop. To correct this, an algorithm is implemented to prevent the actuators to back drive. This is done by kicking the program out of the feedback loop if any of the actuators have to back drive to get to the correct position. Figure 27 shows an improved curve.

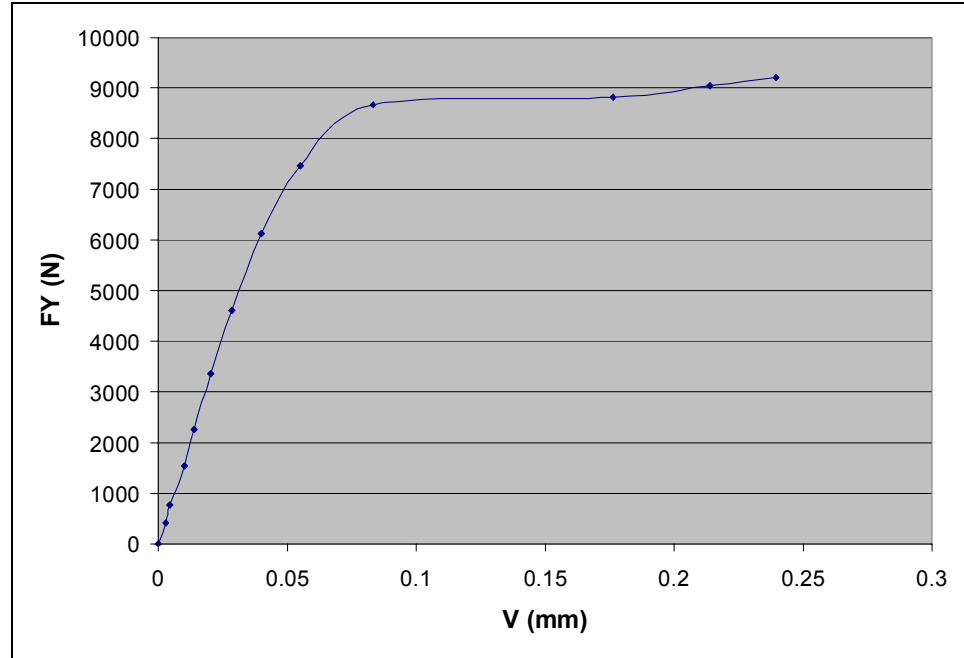


Figure 27.  $F_y/v$  curve without backdrive

Notice that the number of data points decreases significantly from Figure 26. This is not desirable. Solving the back drive issue while maintaining a high number of data points in a test is recommended as future work. Currently, the program is set up for the user to be able to toggle between back drive prevention or not depending on whether a test is expected to run in the inelastic region or not, respectively.

## CHAPTER 5

## VALIDATION TESTS CONDUCTED ON THE IPL

Displacement ReadingsLVDT Precision

The first validation test performed on the LVDTs was to check their individual precision. During a test, 100,000 readings are averaged to output one LVDT value for every move of the IPL. Figure 28 contains data from a tension test and Figure 29 contains shear test data. The precision and smoothness of the curves shows that after averaging over 100,000 data points the displacement readings are acceptably precise (as are the loads).

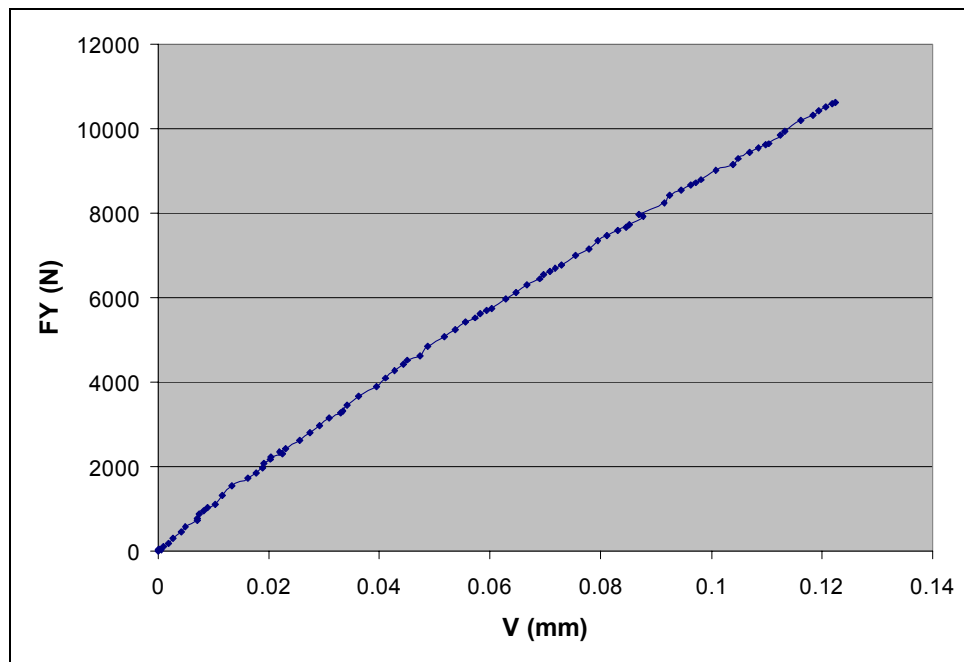


Figure 28. Typical  $F_y/v$  test with a sample showing the precision of the LVDTs after averaging each data point over 100,000 readings

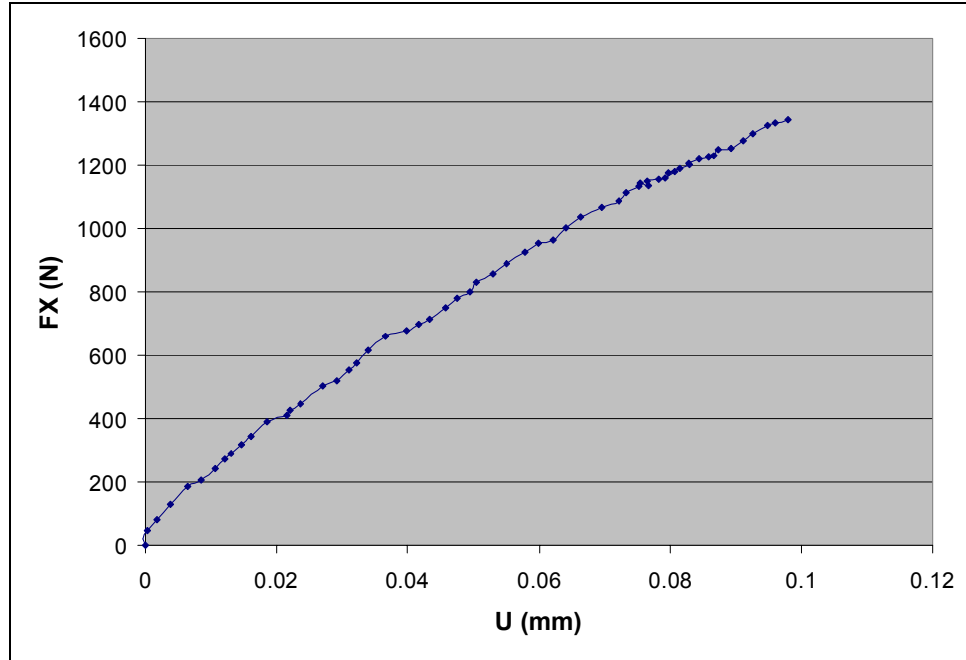


Figure 29. Typical  $Fx/u$  curve using the average of 100,000 readings for both force and displacement

Given the precision of the data during tests, no further precision testing was pursued.

### LVDT Accuracy

The LVDTs were individually calibrated to give accurate displacements. They were then tested in their configuration on the IPL to see if they still gave accurate displacements with no sample (this is the accuracy of reading displacement  $v$ ). The LVDT readings were compared to the readings from a dial gage mounted parallel to the  $y$ -axis between the top and bottom grip faces; positioned at  $x=0$ . Figure 30 and Figure 31 contain the results. The data in Figure 30 show the displacement error versus the displacement read by the dial gage and the data in Figure 31 show the percent error versus the displacement read by the dial gage. The following formula was used to calculate the percent errors:

$$\%error = \frac{IPL\ data - dial\ gage\ data}{dial\ gage\ data} * 100\% . \quad 9$$

Testing  $u$  and  $\omega$  displacements wasn't necessary because the distinction between the three displacements is only a matter of specifying what variable is desired from the vector loop equations.

To gauge the accuracy of the IPL displacement readings compared to the ASTM standard on extensometer verification [14], classification lines are included in the plots. The ASTM standard classifies extensometers according to strain which is the displacement divided by the gage length. The general use of the IPL is to obtain force and displacement data instead of stress and strain data. This is because the coupons generally used in the IPL don't lend themselves to stress and strain measurements. The normal mode of operation is to collect force/displacement data from the IPL and compare that to an FE model of the coupon. Therefore, to be able to compare the IPL displacement accuracy data to the ASTM standard, a gage length of 25.4 mm was used to acquire the classification lines in the figures. This is an arbitrary gage length and was chosen given the IPL coupon that has been used in the past (Figure 3). If a larger gage length value was assumed or the actual tested coupon had a larger gage length, the first piecewise sections of the classifications lines in both Figure 30 and Figure 31 would be higher (these sections come from absolute or fixed errors and are dependent on gage length) and thus more test points would fall between the classification lines. The second piecewise curve sections would not change since they are relative errors and are not dependent on gage length. The data in Table 1 show the ASTM specified values that

constitute the extensometer classifications. Only classifications B-1, B-2, and C are shown in the figures since those are the ones closest to the test data points.

Table 1. ASTM classification of extensometer systems [14].

	Error of strain not to exceed the greater of:	
Classification	Fixed Error (mm/mm)	Relative Error (% of strain)
A	$\pm 0.00002$	$\pm 0.1$
B-1	$\pm 0.0001$	$\pm 0.5$
B-2	$\pm 0.0002$	$\pm 0.5$
C	$\pm 0.001$	$\pm 1$
D	$\pm 0.01$	$\pm 1$
E	$\pm 0.1$	$\pm 1$

To obtain the first piecewise curves in Figure 30, the fixed error values in Table 1 were multiplied by the gage length (25.4 mm). The second piecewise curves were obtained by multiplying the relative error values in Table 1 by the displacement read by the dial gage. The first piecewise curves in Figure 31 were obtained by dividing the fixed error values in Table 1 by the displacement read by the dial gage and multiplying by the gage length. The second piecewise curves are the relative error values from Table 1.

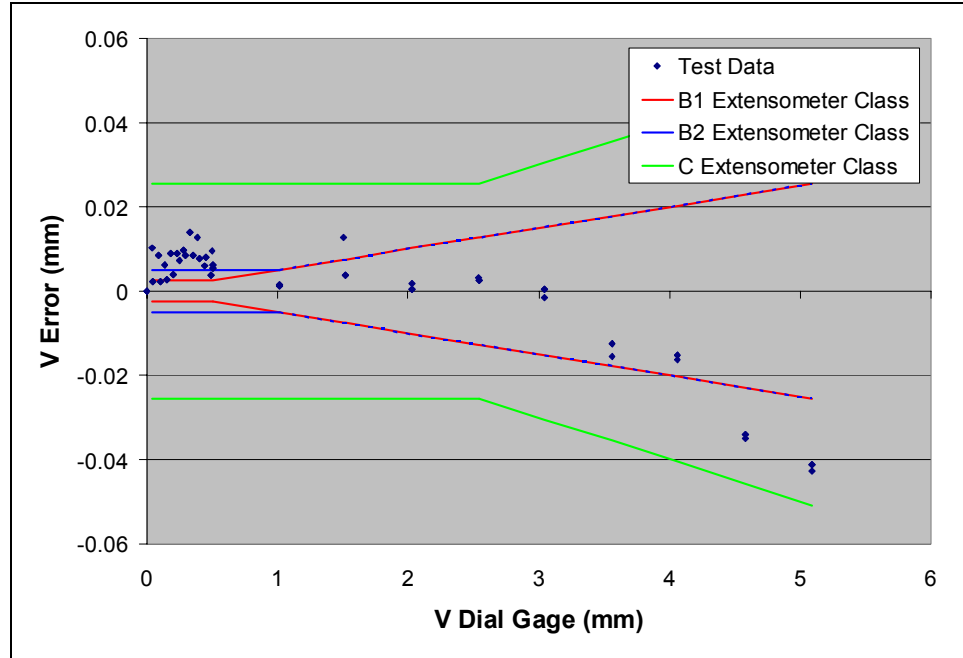


Figure 30. Displacement error of  $v$  read by the LVDTs compared to a dial gage mounted between the top and bottom grip faces

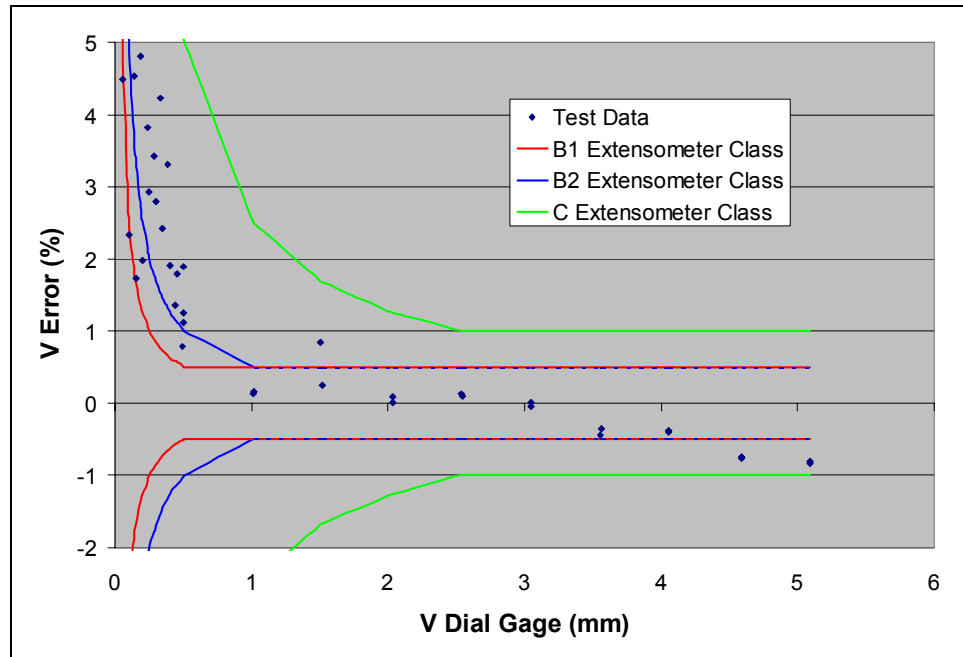


Figure 31. Percent error of  $v$  read by the LVDTs compared to a dial gage mounted between the top and bottom grip faces

Out-of-plane movement of the upper frame with respect to the lower frame adds error to the displacement data of a test on the IPL because the kinematics of the LVDTs do not take into account out-of-plane displacement. Out-of-plane bending forces are also applied to the sample which can't be accounted for in the load cells for the same reason. Self-centering grips and an out-of-plane constrainer were designed to keep the sample in the  $x$ - $y$  plane of the IPL. This was meant to ensure that the forces on the sample were in-line with the actuators and load cells. Tests were run to check the efficacy of these two features. Out-of-plane movement of the upper frame was read by a dial gage attached to the end of a bar which had its other end attached to the lower frame. Many different samples of differing thickness and length were tested to get an idea how these two parameters affected the out-of-plane displacement of the IPL. The data in Figure 32 show the out-of-plane deflection as a function of sample thickness. It was desirable to normalize the data at a common sample load and a common sample strain. 5000 N was chosen as the common load since that is a common yield load for IPL samples. Percent strain at 5000 N was thus the correlating strain. The data in Figure 32 was normalized using Equation 10.

$$\frac{\text{Out-of-plane deflection @ 5000 N}}{\% \text{sample strain @ 5000 N}}$$

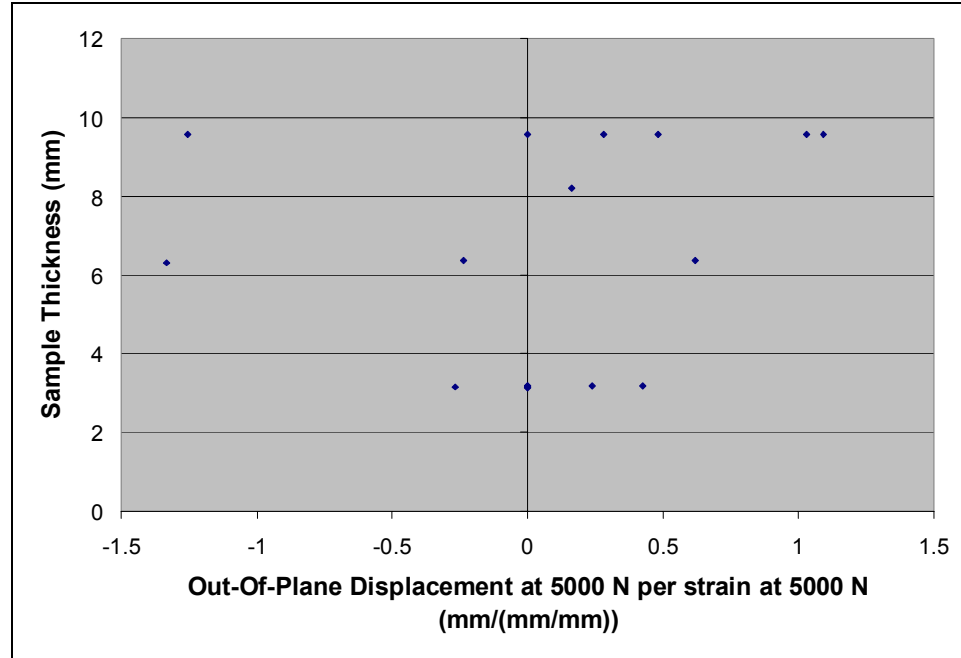


Figure 32. Out-of-plane displacement as a function of sample thickness

The distribution seems to be random except a slight weighting towards bending in the  $+z$  direction.

The magnitude of out-of-plane movement can be understood by Figure 33. It is a load displacement curve of a tension test read by the LVDTs as well as two dial gages; one mounted between the  $+z$  (front) grip faces and the other mounted between the  $-z$  (back) grip faces; both dial gages located at  $x=0$ . A third dial gage measured out-of-plane deflection of the upper frame according to the setup introduced previously.

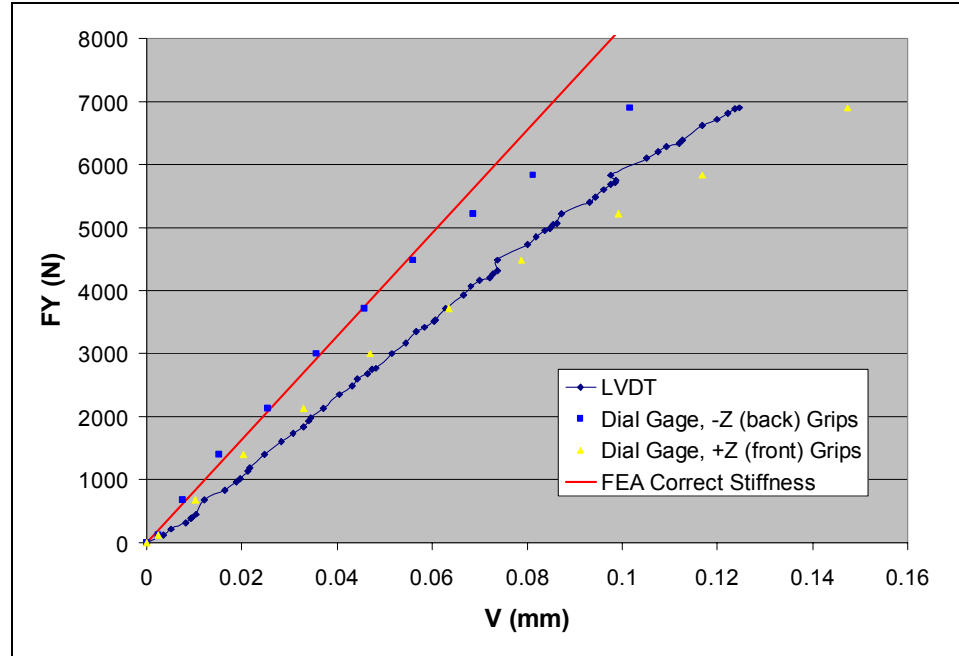


Figure 33. Aluminum sample in tension. Out-of-plane bending measured with dial gages mounted to the front (+z) and back (-z) grips

This is an extreme example of out-of-plane bending. (This sample was made of aluminum and had a stiffness of 81843 N/mm. This should give an accuracy error of about 25% according to Figure 52. The data show that the sample is starting to yield at about 0.1 mm of displacement). This test deflected out-of-plane 1.33 mm at 5000 N per % strain at 5000 N in the -z direction. The data read by the LVDTs shows a slope that is 25 % lower than the slope measured by the dial gage positioned between the -z grips. This is analogous to a 25 % lower elastic modulus. For comparison purposes, the plots in Figure 34 show a tension test that did not deflect out-of-plane evidenced by the similar readings of the two dial gages.

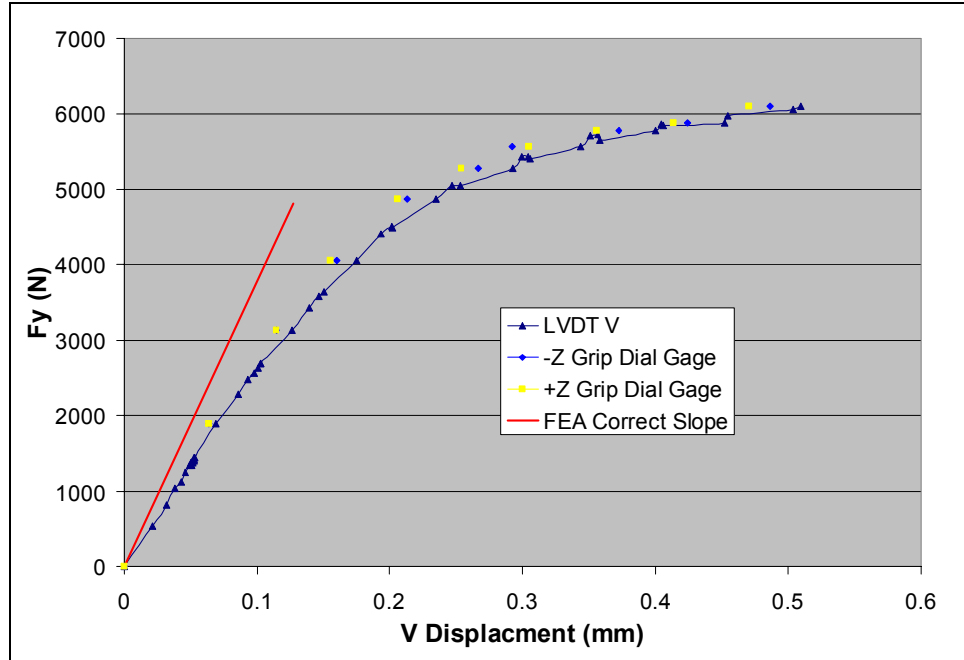


Figure 34. Tension test with dial gages mounted between the  $-z$  and  $+z$  grips to show no out-of-plane deflection

### Grip Bending

Given the way the grip faces are mounted to the grip blocks, there is the possibility of the grip faces bending especially during tension and compression tests.

Figure 35 is a drawing of a grip face.

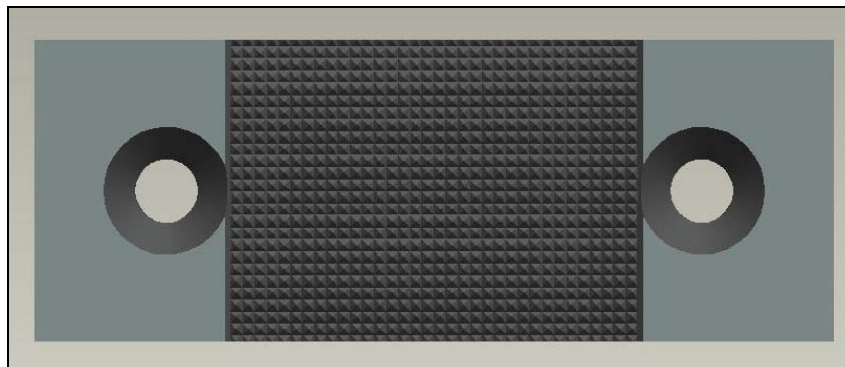


Figure 35. Grip face with two mounting holes

The grip faces are fastened to the grip blocks via bolts inserted through the two holes. In tension and compression tests, this creates a three-point-bending condition. The deflection between the middle of the grip and the point where the bolts hold the grip is not expected to deflect much, but the LVDT arms are attached to the grip faces and extend by as much as 23.5 cm out from the center of the grip face as shown in Figure 36.

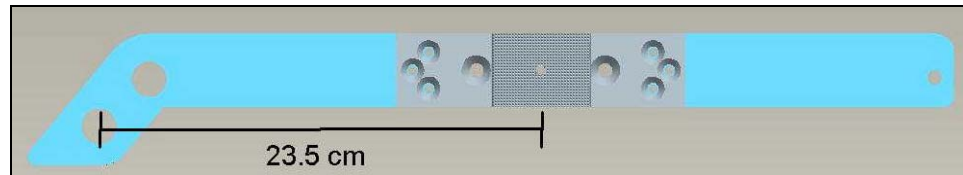


Figure 36. Grip face with LVDT arms attached

Any small amount of bending of the grip face can cause significant deflections where the LVDTs are mounted, thus compromising their accuracy. Tests were done on the grip to see if this bending actually occurs and if so, how much. The data in Figure 37 show a tension test wherein dial gages measured the  $v$  displacement between the top and bottom LVDT arms extending in the  $+x$  direction on the IPL, between the top and bottom grip in the center of the grip face (at  $x=0$ ), and between the top and bottom LVDT arms extending in the  $-x$  direction.

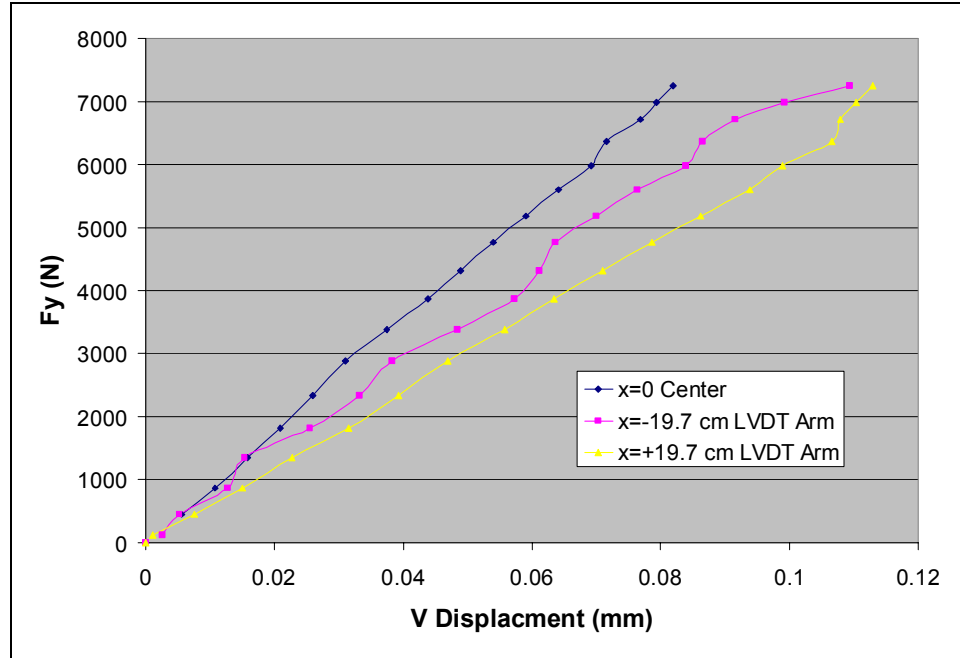


Figure 37.  $F_y/v$  displacement test measured by dial gages between the top and bottom  $+x$  LVDT arms, between the top and bottom grips in the center of the grip face (at  $x=0$ ), and between the top and bottom  $-x$  LVDT arms

The displacements measured on the LVDT arms show deflections greater than the deflection in the center of the grip face and thus lower stiffness curves. There seems to be some overall  $+\omega$  rotation of the IPL as well given that the left and right LVDT curves are not the same slope.

To give further evidence that bending of the grip faces was the cause of lower stiffness curves from the LVDT arm readings, a simple 3-point-bending analysis was done on the grip face with subsequent analysis of the deflections of the ends of the LVDT arms. The resulting deflection was subtracted from the displacement values of the LVDT arm curves to see if all three curves then lined up. Equation 11 gives the angle the grip face makes with the  $x$  axis at the fastening bolts with a center load applied for a beam in three-point bending.

$$\theta_{\max} = \frac{PL^2}{16EI}. \quad 11$$

The sine of this angle was then multiplied by the length of the LVDT arm (16.25 cm, measured from the bolt to the connection point of the LVDT) to get the amount of  $v$  deflection that occurs in the LVDT arm. (The angle in reality is so small that the approximation  $\sin(x) \sim x$  can be made without losing any accuracy). The resulting deflection was multiplied by 2 since both the  $+y$  and  $-y$  LVDT arms flex and then divided by 2 since both of the  $+z$  and  $-z$  grips take half the load (of course these both cancel out and don't need to be done). In Equation 11,  $P$  is the applied force,  $L$  is the length between the bolts (6.8 cm),  $E$  is taken to be the elastic modulus of steel (200 GPa), and  $I$  is equal to  $bh^3/12$  ( $b$  is equal to the thickness of the grip face (12.7 mm), and  $h$  is the height of the grip face (38.1 mm)). Adjusting the deflection of the LVDT arms in Figure 37 results in Figure 38.

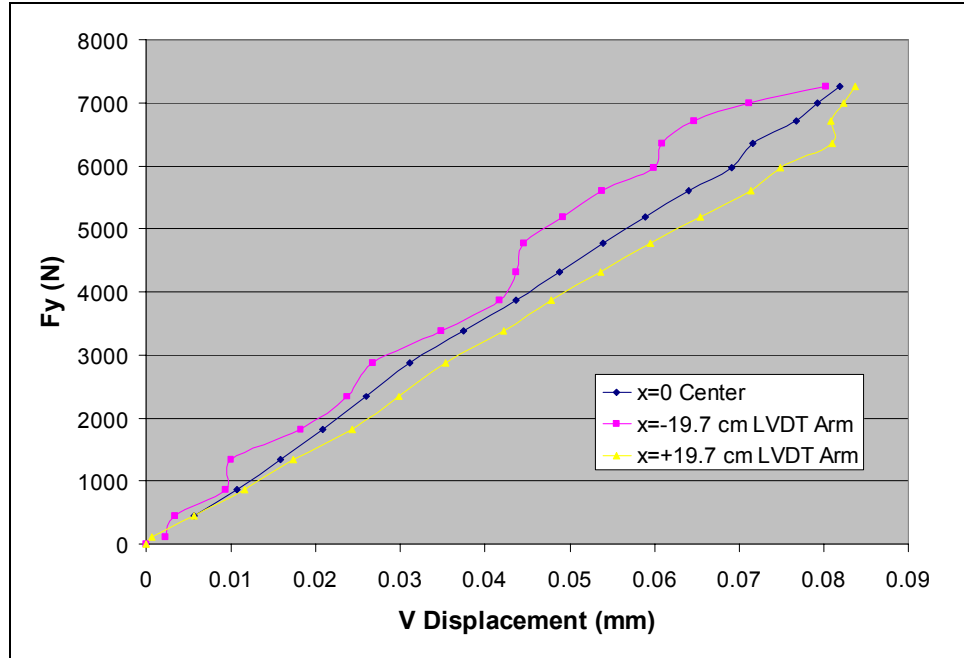


Figure 38.  $F_y/v$  curves after correcting the grip bending of the  $-x$  and  $+x$  LVDT arm curves

The LVDT arm curves are centered around the curve obtained from the dial gage positioned in the center showing that the grip bending effects are taken out.

### Gripping Effects

Gripping effects can be separated into two mechanisms that both produce the same effect: namely, showing more compliance in a test sample than actually happens. The first mechanism is stress induced into the sample from the pressure of gripping. A compression stress on the part of the coupon that is gripped causes Poisson effects that extend into the gage section of the sample thereby introducing more compliance in the sample. The second mechanism is the sample slipping in the grips. This slipping is not measured since the IPL measures how much the grips displace. On a standard uni-axial testing machine, displacement is measured directly on the sample via a sample mounted

extensometer or strain gage; therefore, gripping stresses and grip slipping are of no consequence. These two mechanisms are difficult to distinguish from one another and thus will be lumped into the same mechanism since the consequence is the same.

The test was run on an aluminum sample that had a circular cross section in the gage section and rectangular cross sections at the ends for gripping. The transition between the circular cross section and the rectangular cross section was relatively sharp and the entire rectangular cross section area was gripped. The diameter was 4.1 mm and the gage length was 96.5 mm. The gage length was long to minimize the gripping effects. To test for gripping effects, the other sources of testing error had to be eliminated. The test was run by measuring displacement between the top and bottom grips using two dial gages; one mounted between the  $+z$  grips and the other mounted between the  $-z$  grips. Both dial gages were positioned in the center of the grip faces (at  $x=0$ ) which ruled out grip bending affecting the results. Out-of-plane bending could be accounted for by comparing the  $+z$  and  $-z$  dial gage curves. If they were similar, out-of-plane bending could be discounted. An independent test was run on a uni-axial testing machine with a sample mounted extensometer for comparison. Figure 39 contains the test results.

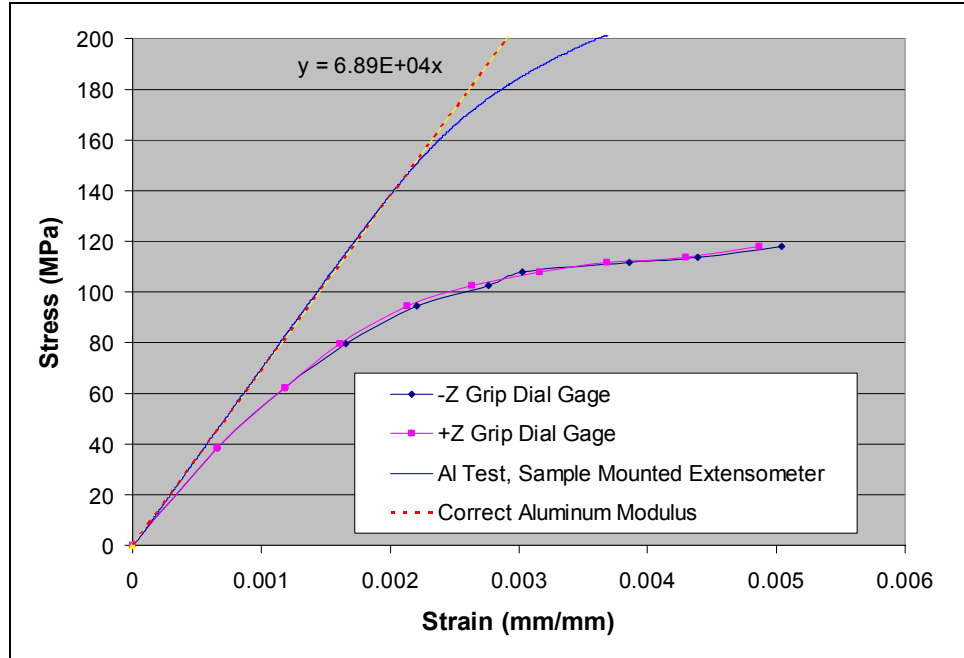


Figure 39. Tension stress/strain curve of 6061-T651 aluminum measured by two dial gages; one located between the  $-z$  grips and the other located between the  $+z$  grips; compared to the true modulus and an independent extensometer mounted tension test

The two dial gage readings are similar thus eliminating out-of-plane bending as a factor. Gripping effects are thus the difference in slope of the true stress strain curve and the curves measured by the dial gages. The elastic region of the curve doesn't remain linear until yield. This could be a sign of grip slippage (but not grip stress. Gripping stresses are assumed to be constant if the gripping pressure remains constant throughout a test, which it is supposed to do). The low yield point of the IPL sample is also a sign of grip slipping.

Examining some other IPL tests, some remain linear in the elastic region and some do not. The following figures show some curves of each.

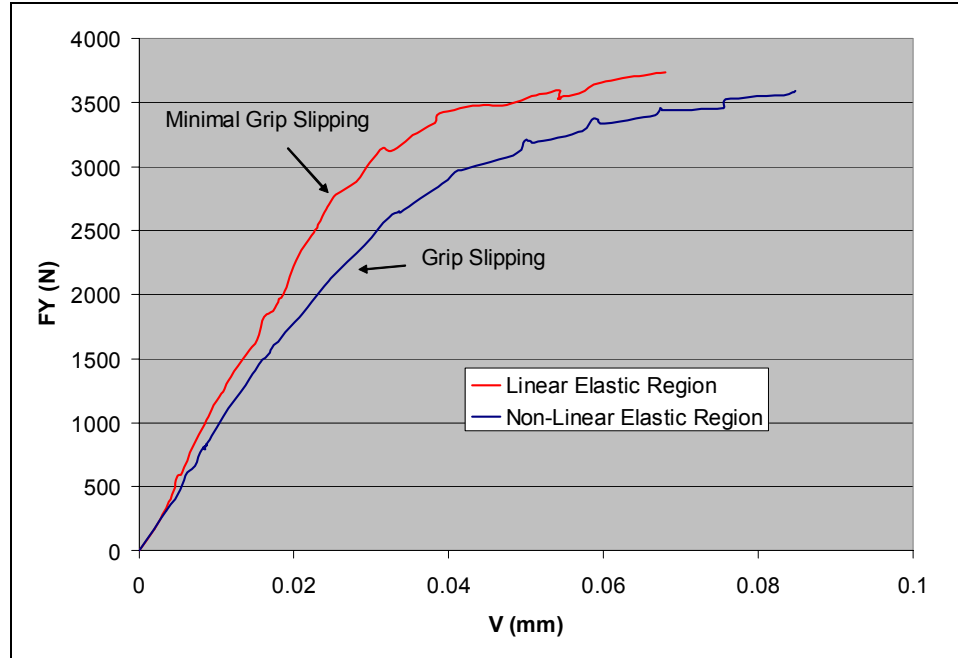


Figure 40. Aluminum tension tests on the IPL, linear and non-linear elastic regions

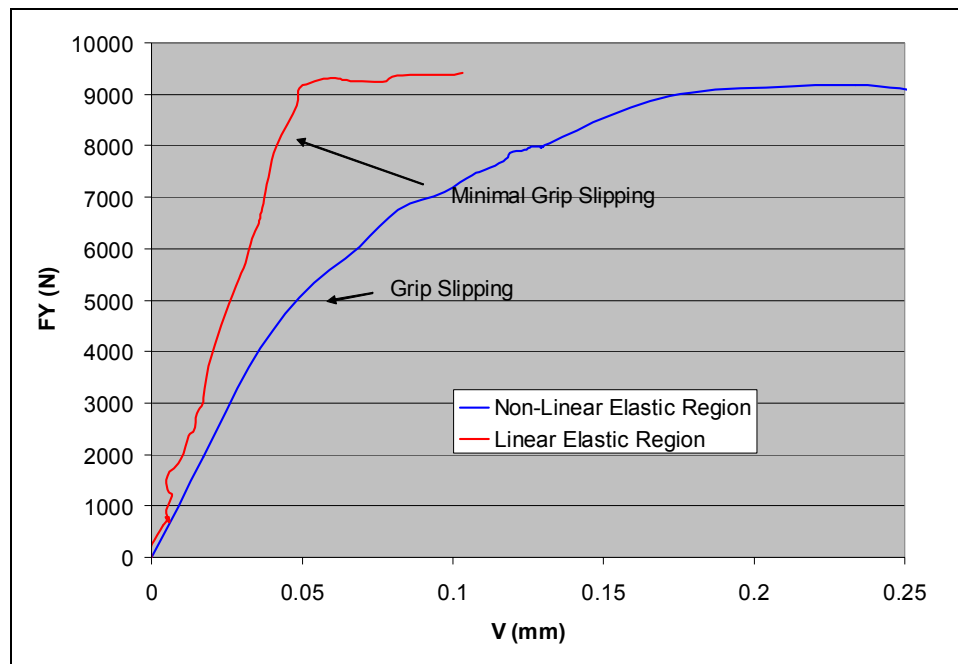


Figure 41. Steel tension tests on the IPL, linear and non-linear elastic regions

The curves in Figure 40 and Figure 41 show that the IPL can produce force/displacement test data that have linear and non-linear elastic regions for steel and aluminum tension

test samples. The presence of a non-linear elastic region in a test is a sign of the sample slipping in the grip. A modulus that differs from the true modulus of the material (if correct sample geometry is used to produce a stress/strain graph) is also a sign of grip slippage and could also be a sign of grip induced stresses within the sample.

### Load Readings

#### Precision of Loads

The precision of the load cells was first examined by acquiring 100,000 readings from the three load cells with constant loads applied (Table 2). The data were taken while the load cells were installed on the IPL with a gage length of 63.5 mm between the grips and no  $u$  or  $w$  displacements. The difference in the mean load values among the three load cells in Table 2 reflects the portion of weight each load cell carries in its home kinematic configuration (reference Figure 16). Absolute and relative standard deviation values were obtained. The second precision test was to test the precision of the resolved load components  $F_x$ ,  $F_y$ , and  $M_z$ . These were tested in the same IPL configuration as the previous test and 100,000 readings were again taken.

Table 2. Precision load tests performed with in-house built amplifiers and a 12-bit A/D converter

	Absolute $\sigma$	Relative $\sigma$	Mean
Load Cell 1	12.9 N	6.3 %	-203 N
Load Cell 2	18.1 N	13.4 %	135 N
Load Cell 3	17.8 N	3.7 %	478 N
$F_x$	10.8 N	7.5 %	145 N
$F_y$	28.2 N	5.8 %	489 N
$M_z$	9.2 N-m	7.8 %	-117 N-m

The data in Table 2 show that the three load cells have similar absolute standard deviations with an average of the three being about 16 N. By contrast, the relative standard deviation values vary quite a bit.  $F_y$  has a much larger absolute standard deviation than  $F_x$  but the relative standard deviations are similar. The relative standard deviation of  $M_z$  is also similar to  $F_x$  and  $F_y$ .

To get a feel for the values shown in Table 2, typical results from IPL tests are presented. Figure 42 contains data from a representative  $M_z$  versus  $\omega$  test on a standard coupon tested on the IPL. This test was run with no load data averaging. The absolute standard deviation lines shown are from Table 2 and are  $\pm 9.2$  N-m.

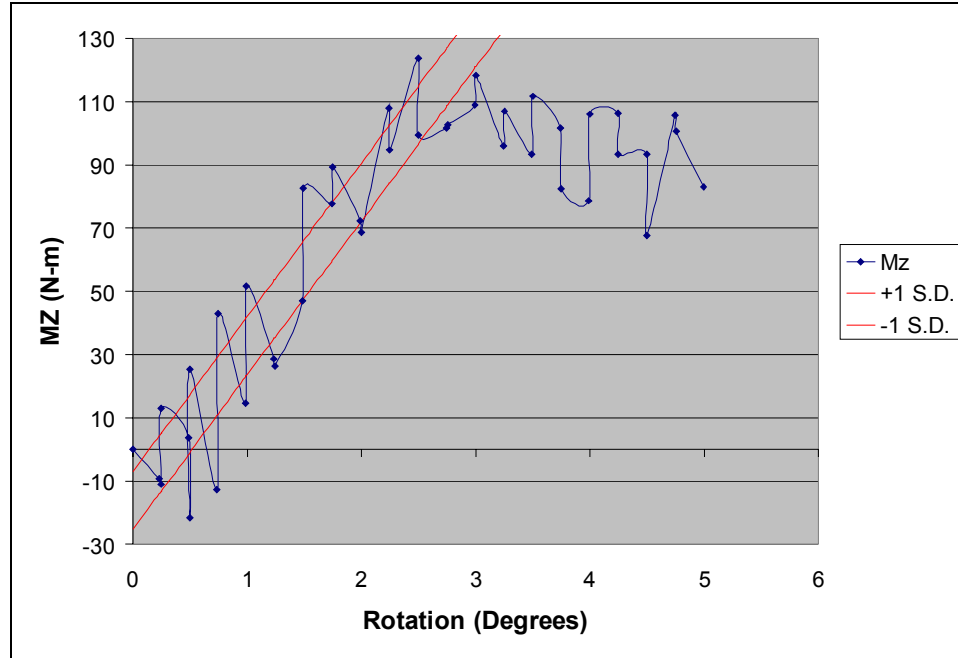


Figure 42. Typical  $M_z$  versus  $\omega$  curve from an IPL test with no force or displacement data averaging

The moment precision error is about a fifth of the largest moment in the test. A test that averages 100,000 load and displacement readings for each data point on the curve, the moment standard deviation decreases to about 2.5 N-m as seen in Figure 43. The same absolute standard deviation lines of  $\pm 9.2$  N-m are shown for comparison (these data in Figure 43 only show a portion of a test for clarity).

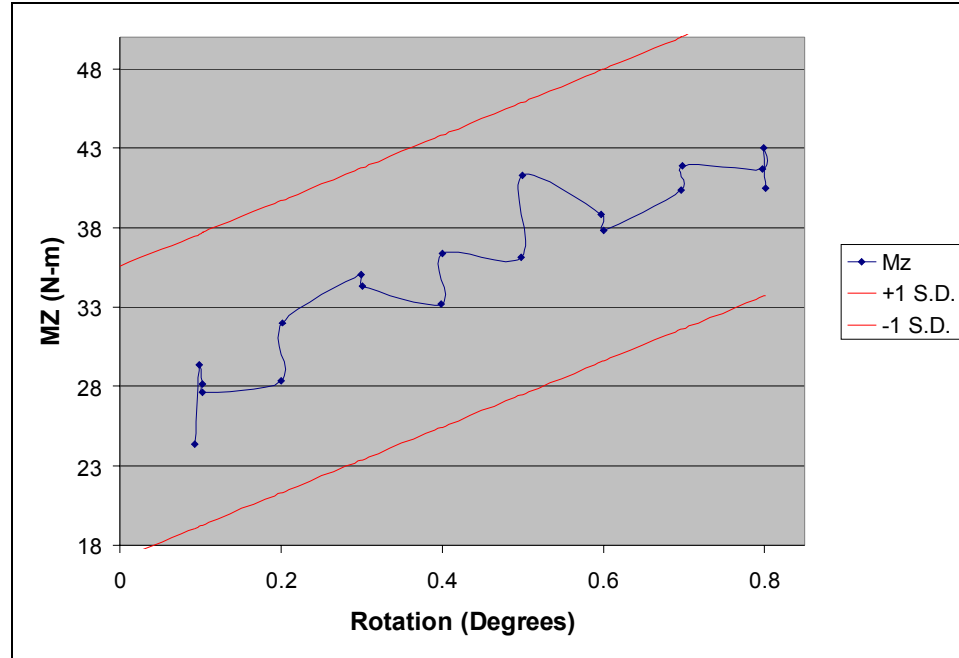


Figure 43. Typical  $M_z$  versus  $\omega$  curve from an IPL test that averages 100,000 load cell and LVDT readings for each data point on the curve

The precision error of 5 N-m is still about 5 % of the maximum moment in a standard sample test (considering the data in Figure 42 to represent a standard test and assuming the maximum moment is about 100 N-m). This is a large imprecision compared to a  $F_x/u$  curve shown in Figure 45 and a  $F_y/v$  curve shown in Figure 44; both of which have much higher precision in the loads (100,000 load and LVDT readings are averaged for each data point on these curves).

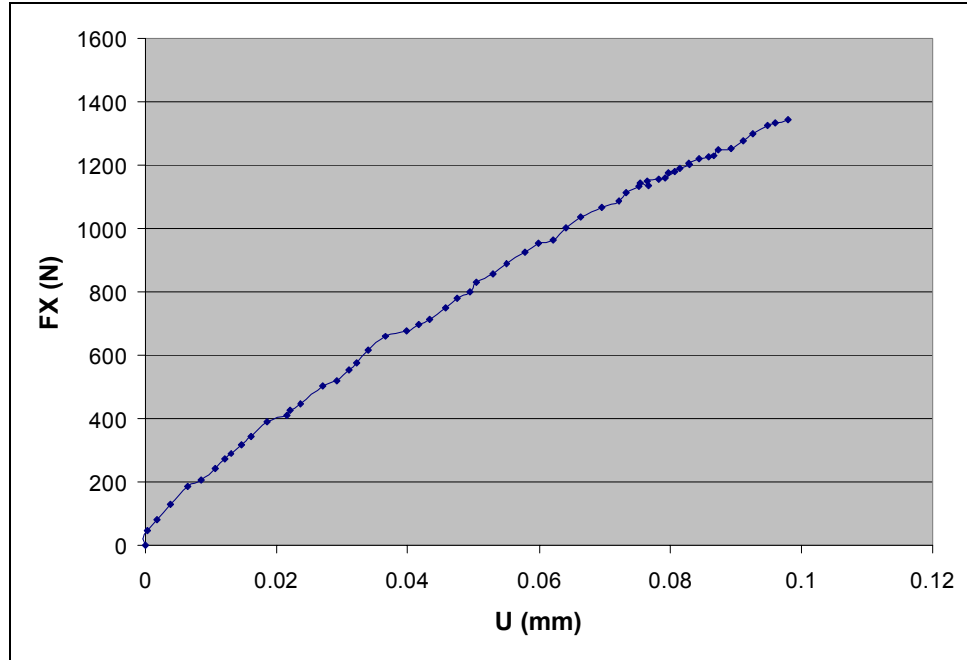


Figure 44.  $F_x/u$  curve using the average of 100,000 readings for both force and displacement

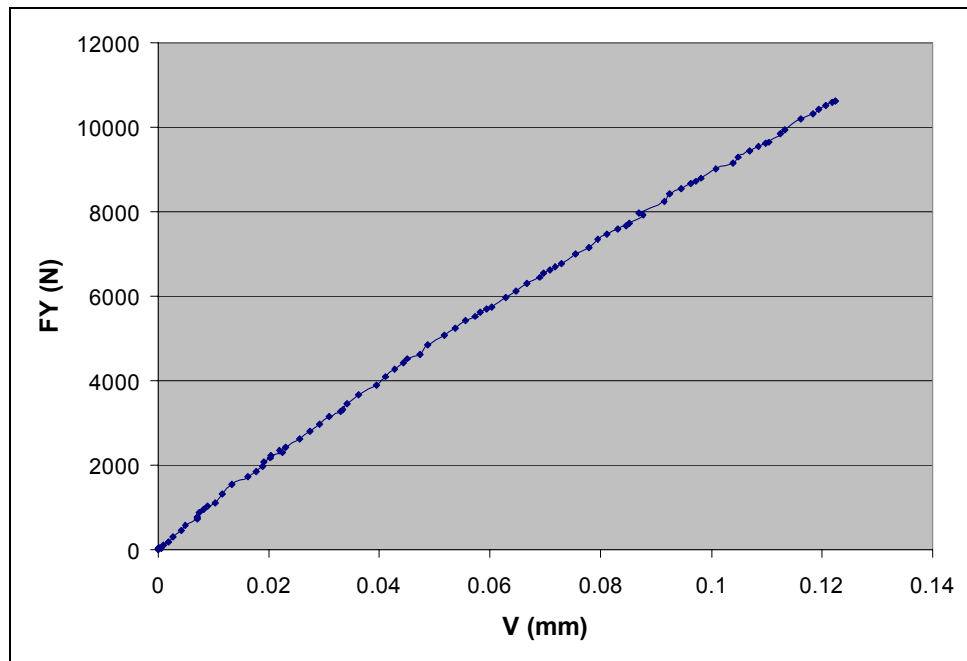


Figure 45.  $F_y/v$  curve using the average of 100,000 readings for both force and displacement

### Accuracy of Loads

Each individual load cell was calibrated before being installed on the IPL. After installation, the resolved loads were tested to verify their accuracy.  $F_x$ ,  $F_y$ , and  $M_z$  loads were compared with loads from an independent load cell.  $F_x$  was generated by compressing the load cell between two bars attached to the  $+y$  and  $-y$  grips.  $F_y$  was generated by simple compression forces and  $M_z$  was created by offsetting the independent load cell in the  $x$  direction by 217.49 mm. The results are shown in Figure 46 through Figure 50. Each data point is the average of 100,000 data points which was done to minimize the effect of imprecision and focus on accuracy. Equation 9 was used to calculate percent error.

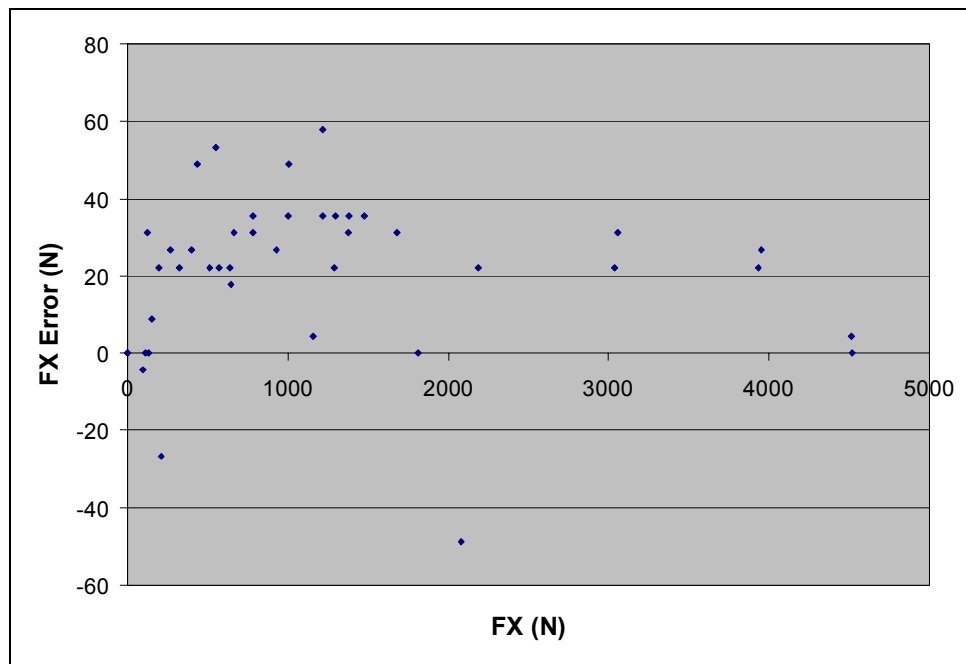


Figure 46. Load error of  $F_x$  loads versus true  $F_x$  loads

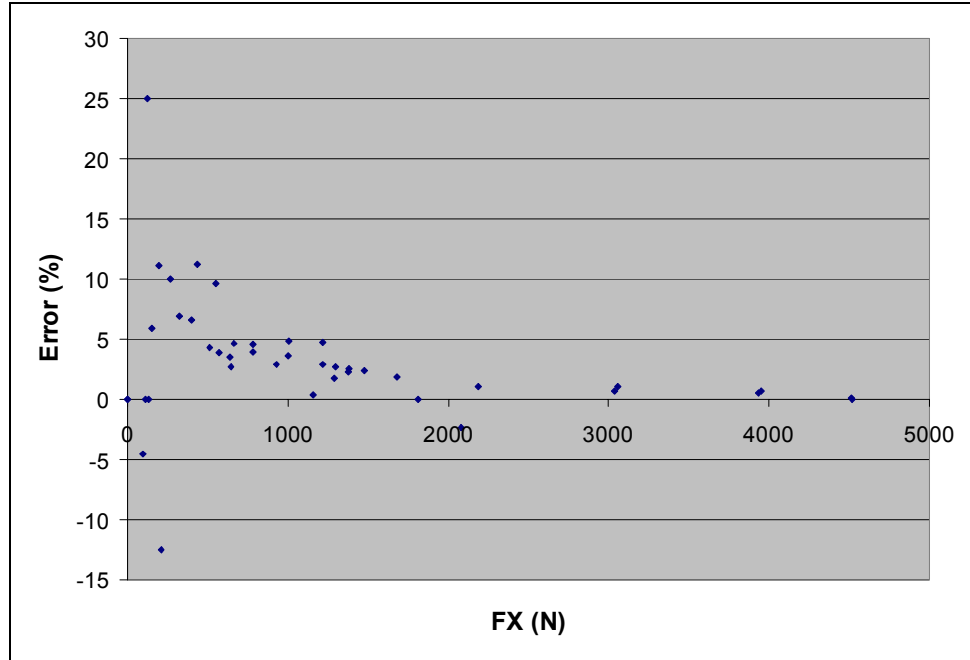


Figure 47. Percent error of  $F_x$  loads versus true  $F_x$  loads

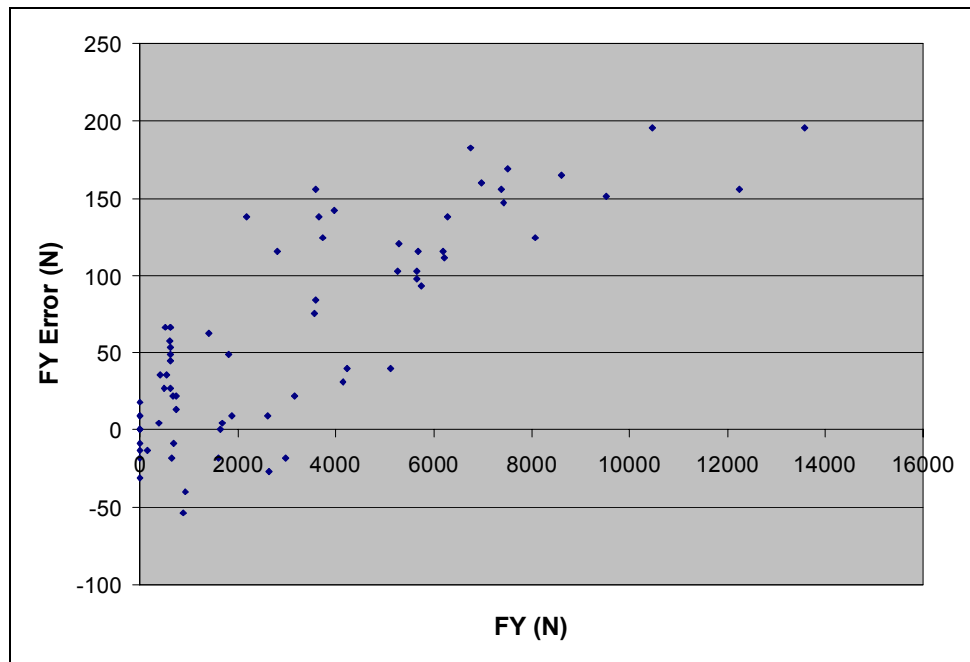


Figure 48. Load error of  $F_y$  loads versus true  $F_y$  loads

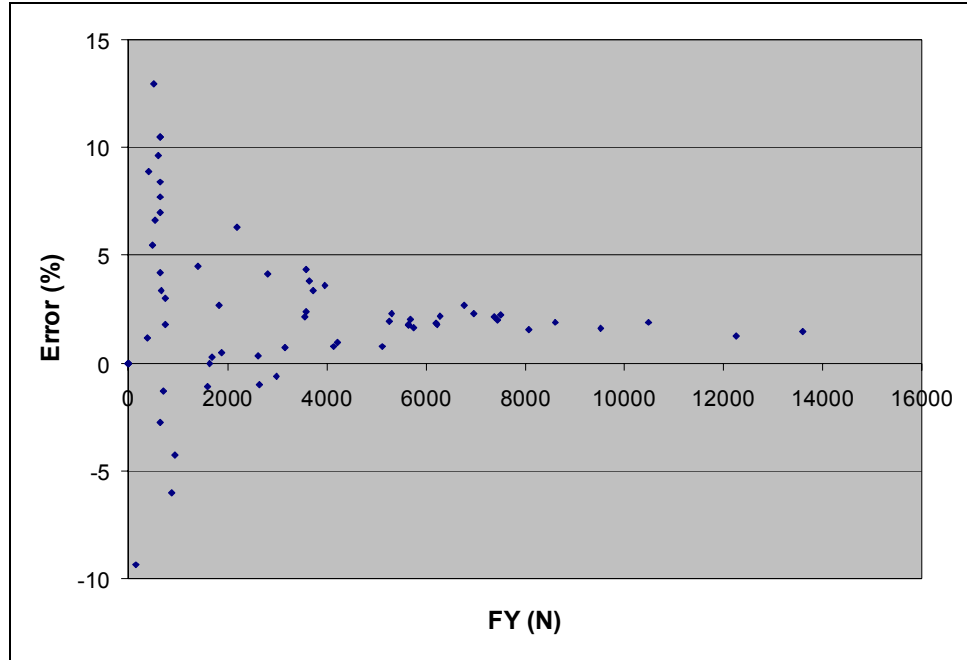


Figure 49. Percent error of  $F_y$  loads versus true  $F_y$  loads

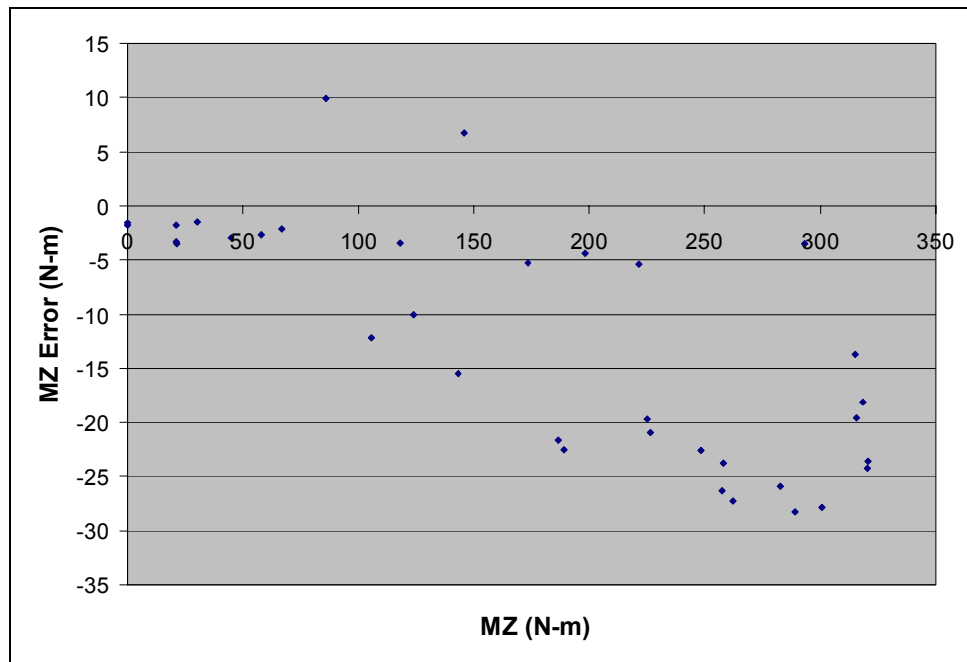


Figure 50. Moment error of  $M_z$  loads versus true  $M_z$  loads

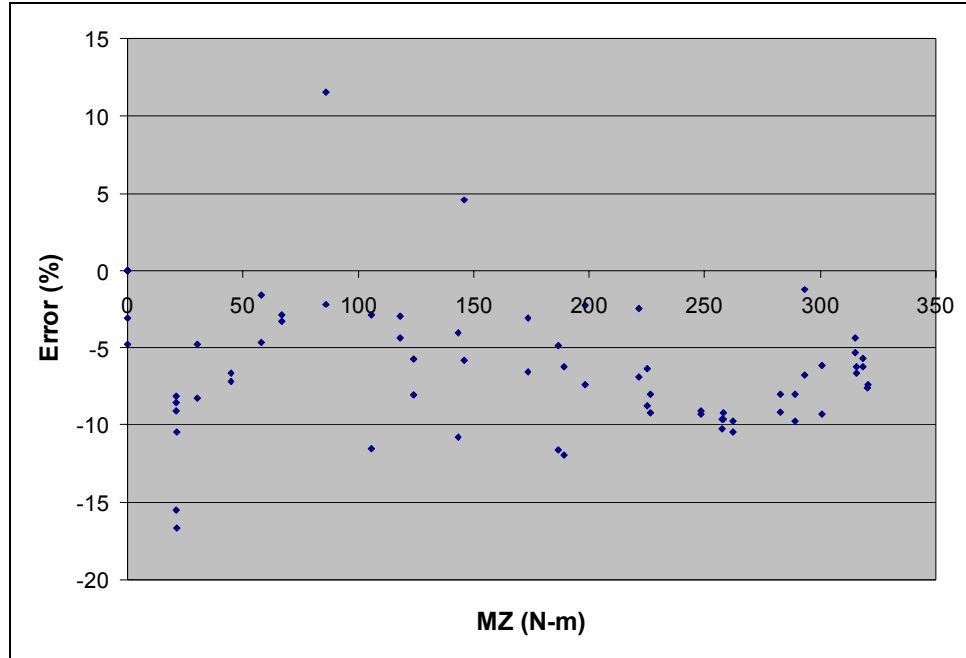


Figure 51. Percent error of  $M_z$  loads versus true  $M_z$  loads

Percent errors are greatest when loads are the smallest as seen in Figure 47 and Figure 49.  $F_x$  and  $F_y$  loads stay within  $\pm 5\%$  as the loads get larger. The moments vary by about  $\pm 10\%$  as the loads get larger. These errors are expected to decrease significantly by updating the load cell amplifiers and increasing the data acquisition digitizer to 16 bit.

#### Displacement Tests with Samples

Sample tests were done in tension, shear, and compression. Moment tests were not done given the large moment errors shown in Figure 42, Figure 43, Figure 51, and Figure 50. The materials used in the tests were 1020 steel, 6061-T651 aluminum, and Newport NCT307-D1-E300 Glass prepreg. The steel had an elastic modulus of 200 GPa and a Poisson's ratio of 0.29. The aluminum's elastic modulus was 68.9 GPa and Poisson's ratio was 0.33. The fiberglass material properties are shown in Table 3.

Table 3. Material properties of fiberglass coupons used for IPL validation testing

Fiber/Resin	Layup	V <sub>f</sub> (%)	E <sub>L</sub> (GPa)	E <sub>T</sub> (GPa)	G <sub>LT</sub> (GPa)	ν <sub>LT</sub>
NCT307-D1-E300 Glass	[0,±45,0] <sub>s</sub>	47	35.5	8.33	8.55	.33

The geometries of the samples varied widely. There was a mixture of constant cross section, double-notched, and dog bone samples. The radii in the dog bone and notched samples varied as well as the thickness and lengths of the samples. Samples were compared to FEM obtained force versus displacement elastic curves using the material properties specified above. Experimental data was compared to FEM data using the following equation:

$$\% \text{ diff} = \frac{IPL \text{ data} - FEM \text{ data}}{FEM \text{ data}} * 100\% . \quad 12$$

### Tension Testing

The data showed percent differences ranging from 7% up to 50%. Thus the experimental data was always more compliant than the FEM data. The percent error difference had no correlation to shape or thickness of sample but examining a graph of percent error versus sample stiffness, a trend emerges (Figure 52).

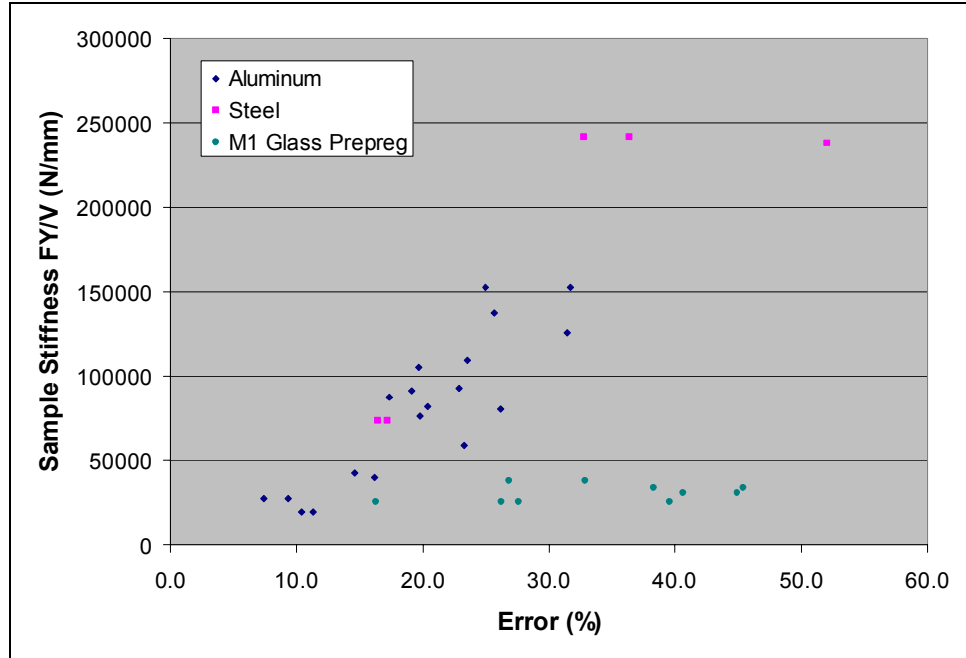


Figure 52.  $Fy/v$  slope versus % error for aluminum, steel, and fiberglass samples

The aluminum and steel samples follow a trend that the percent error is proportional to the stiffness of a sample (this is not the same as the stiffness of a material). Sample stiffness or force divided by displacement is a function of cross sectional area of the sample  $A$ , the modulus  $E$ , and the gage length of the sample  $L$  ( $F/D=AE/L$  for a constant cross section sample). None of the other parameters of the tests showed as great of influence on the accuracy as the force divided by displacement value. The fiberglass samples don't follow such a clear trend.

### Shear Testing

Shear test results follow a similar trend as the tension tests for aluminum; the percent error is dependent upon the force/displacement slope (Figure 53).

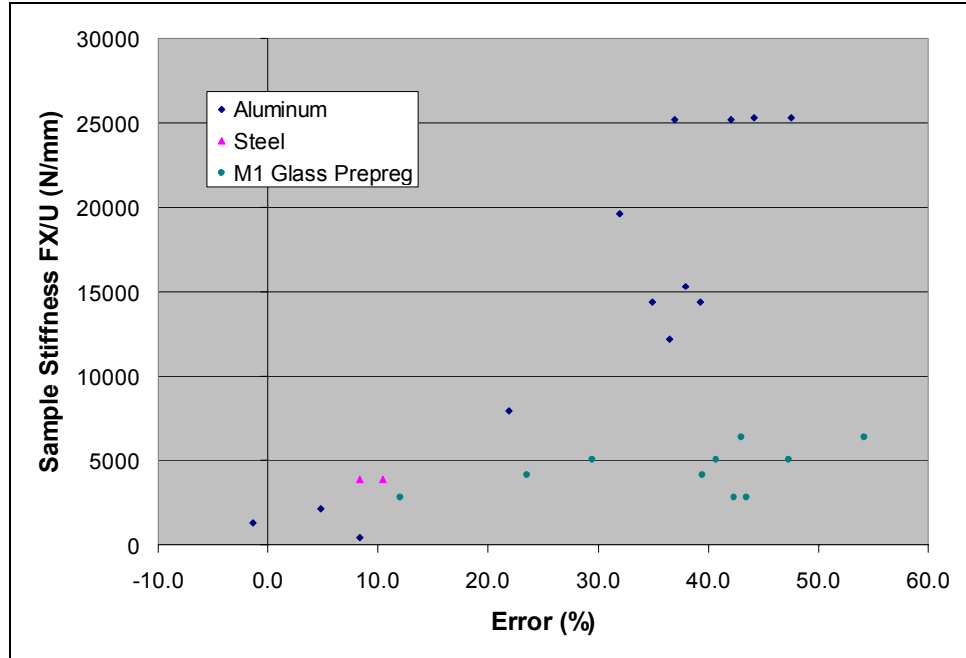


Figure 53.  $Fx/u$  slope versus percent error for aluminum, steel, and fiberglass samples

Again, the fiberglass samples have much higher percent errors for similar sample stiffness values than the aluminum and steel.

### Compression Testing

The data in Figure 54 show the force/displacement slope versus percent error for compression tests.

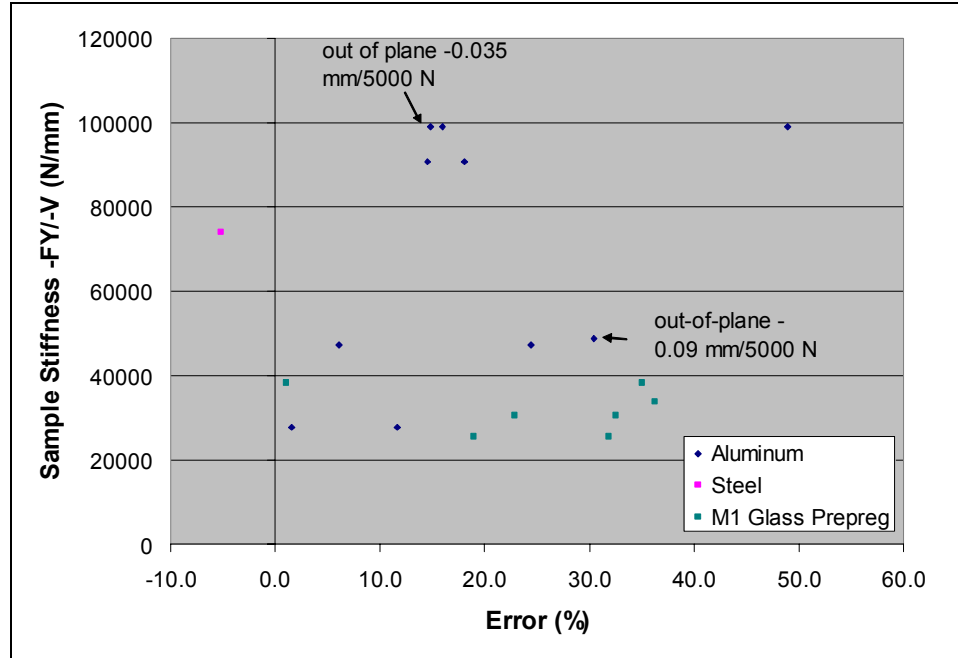


Figure 54.  $-F_y/-v$  (compression) slope versus percent error for aluminum, steel, and fiberglass samples

Compression data also follows the trends established in the previous tension and shear tests although the data are more scattered. The fiberglass composite coupons show more error for a given sample stiffness which is consistent with the other tests.

## CHAPTER 6

## DISCUSSION OF THE TESTING RESULTS

The IPL records two parameters during a test: displacements and loads. Four sources of displacement error and one source of load error were identified in Chapter 5. The sources of displacement error are: LVDT readings, out-of-plane bending, grip deflection, and gripping effects. The load error is the load readings. The following discussion addresses each of these and how they contribute to the errors in the tension, shear, and compression tests. A specific discussion of the tension, shear, and compression tests then follows.

Displacement ReadingsLVDT Precision

The voltage signals output from the LVDTs pass through several signal manipulators before the combined readings of the three LVDTs give  $u$ ,  $v$ , and  $w$  of the IPL. Let's start at the LVDTs and discuss the effect on error each manipulation can have.

The Omega LD600-50 LVDTs have a rated sensitivity of 6 mV/V/mm and a total stroke length of 100 mm. The input voltage is 10 V. The full scale output is then 6 V or  $\pm 3$  V. This signal is passed to the National Instruments SCXI-1303 Terminal Block which is connected to the SCXI-1100 Module. This is connected to a SCXI-1000 Chassis which is connected to a NI PCI-6034E DAQ Device. The signal remains analog until the NI 6034E DAQ device which converts it to 16 bit digital. This gives 65,536

binary values over  $\pm 10$  V input. The resolution is then 0.31 mV/bin or 0.00508 mm/bin. If the full scale output voltage from the LVDTs could be amplified to  $\pm 10$  V, the resolution could be 0.00153 mm/bin although a resolution of 0.00508 mm is acceptable for the IPL. After averaging 100,000 readings per data point as seen in Figure 28, the resolution is much better than 0.00508 mm.

### LVDT Accuracy

The lengths of the LVDTs are part of the vector loop equations explained in Chapter 3. For the vector loop equations to output correct  $u$ ,  $v$ , and  $\omega$  values, the locations of the LVDT pivot points have to be known to some accuracy. The method of determining these pivot point locations is by using calipers and can only be considered accurate to within  $\pm 0.1$  mm. Even so, the data in Figure 30 show the accuracy to be much better than 0.1 mm. The reason for this is that the LVDTs are zeroed at the start of every test so the inaccuracy of the pivot point locations is negated at that point. From there, the change in the LVDT lengths as the IPL moves is a couple orders of magnitude smaller than the measured distance from the LVDT pivot points to the center of the IPL. This produces much more accurate displacement readings from the LVDTs compared to the accuracy to which the LVDT pivot points are known.

The data in Figure 30 show that the displacement error is somewhat constant at an average of 0.007 mm until about 1 mm of displacement. After a displacement of 3 mm, the accuracy drops off dramatically but the percent error remains under  $\pm 1\%$  (Figure 31). The percent error reaches 5% from 0 to 0.5 mm of displacement. 0.5 mm of displacement covers the entire elastic region in a standard tension test. However, if the

error data from Figure 30 is used to correct a representative tension test curve, the slope increases by at most 1.5% (because the error only changes by 1.5 % over the elastic region). The data show that the IPL is classified as a C extensometer system [14]. The fixed error is within  $\pm 0.001$  mm/mm (for a gage length of 25.4 mm) and within  $\pm 1\%$  (Figure 30, Figure 31, Table 1).

The displacement error does not have a large effect on the slope of an elastic region of a test and is thus not considered a major error in the tension, shear, and compression tests. If increased accuracy is desired however, the position of the pivot points needs to be measured more accurately.

### Out-Of-Plane Deflection

#### Causes of Out-Of-Plane Deflection

The scatter of data about the centerline in Figure 32 shows that out-of-plane deflection of the IPL during a test does not depend on sample thickness. If all the data fell to one side of the centerline then it would indicate an off-centered sample. Since sample thickness does not affect the out-of-plane deflection, the self-centering grips can be assumed to keep the sample centered front-to-back in the IPL.

The out-of-plane deflection could be caused by an unsymmetrical sample about the  $x$ - $y$  plane. The samples tested were theoretically symmetrical so this cannot be a major contribution to out-of-plane deflection. If grip slippage occurs more on one side than the other however, an imbalance could occur. Another contribution to imbalance could come from the bolts that hold the grip blocks to the grip body shown in Figure 19. They need to be tightened equally between the  $+z$  and  $-z$  sides to prevent an imbalance.

In any case, the out-of-plane-constrainer was designed to limit out-of-plane deflections. It is not stiff enough to do so with the amount of accuracy needed by the IPL as shown in Figure 33.

#### Effects of Out-Of-Plane Deflection on Sample Tests

Out-of-plane deflection does not explain the trend in Figure 52, Figure 53, and Figure 54 that higher stiffness samples have more error. If out-of-plane deflection was the problem, these three figures would show errors scattered about 0% since sometimes the out-of-plane deflection would be  $+z$  with positive percent errors (the LVDTs are connected to the  $-z$  grips and would show more displacement) and sometimes the out-of-plane deflection would be  $-z$  with negative percent errors (the LVDTs would show less displacement). The figures show positive error meaning the LVDTs record more displacement than they should.

A major effect of out-of-plane deflection is seen in Figure 54 of the compression test data. There is not as clear a trend between higher percent errors and higher force/displacement slopes as there is for the tension and shear tests, although it is still generally seen. The scatter is likely due to out-of-plane deflection since compression tests are inherently susceptible to buckling and thus prone to out-of-plane deflection.

In summary, out-of-plane deflection does not contribute consistently to the trend of a generally softer material response in tension, shear, and compression tests. It does greatly affect the displacement readings in a test however; the elastic force/displacement slope can be as much as 25% lower (Figure 33). The occurrence of out-of-plane deflection is much more random than other effects and difficult to predict. A better out-

of-plane constraining system that eliminates out-of-plane deflection would greatly increase confidence in IPL data.

### Grip Bending

Grip deflection should be more of a factor in tension and compression tests than in shear tests given the way the grip faces are fastened to the grip blocks (Figure 35). The theoretical analysis to correct for grip deflection seems to work well to provide further evidence of grip deflection. Whether to use this method or not to correct test error is another matter. In practice there is going to be friction between the grip face and the grip block that is not taken into account in the theoretical model. Also, tests are not run only in tension on the IPL and grip deflection is harder to predict for other loading directions. Grip deflection is also not the only error in a test. The metal shear tests shown in Figure 53 have a slope of around 375 N/mm/% error whereas the metal tension tests have a slope of 5000 N/mm/% error (Figure 52). This means that the shear tests have much more error for a given sample stiffness. Grip deflection does not explain the errors in shear tests since the shear force does not produce bending in the grips. This discounts the usefulness of correcting displacements in a test with analytically derived grip deflection values.

Grip deflection does explain to some extent the trends in the tension (Figure 52) and compression (Figure 54) tests that higher stiffness samples have more error. The amount of grip deflection is a function of load on the grip face, not sample compliance. Nevertheless, with a more compliant sample, the grip deflection is smaller compared to

the deflection of the sample. The grip deflection is therefore a smaller source of error in a test with a more compliant sample.

The errors in tension and compression tests can be partly accounted for by grip deflection whereas shear tests are not affected as much by grip deflection. Grip deflection could be eliminated by fastening the grips so a three-point-bending situation is eliminated.

### Gripping Effects

Gripping effects are inherent problems with reading displacements from the grips. Minimizing these effects is an important aspect of getting accurate results from the IPL (Huang [11] addresses this problem by modeling the grip/sample interaction with contact elements in the FEA model). The following discussion addresses these effects and how they can be minimized. First, a discussion is presented of how a non-linear elastic region in a test can show gripping effects, and second, how gripping effects affect the error in the tension, shear, and compression tests.

### False Non-Linear Constitutive Response

The data in Figure 39 show that indeed gripping effects are responsible for some of the error in a tension test. The curve produced by the LVDTs veers away from linear and does not have a clear yield point. It also has a much lower yield point than the sample tested with a sample mounted extensometer. The test data acquired from the sample mounted extensometer show that aluminum tension tests have a clearly defined

linear region. Some data from tests performed on the IPL do show appropriate linear constitutive responses as seen in Figure 40 and Figure 41 and some do not.

The false non-linear constitutive response cannot be because of the grip faces bending because the grips bend linearly proportional to the applied load (if the angle remains small). Error due to grip bending would show a curve that is more compliant than the true modulus but it would still be linear. The gripping effects seen are proposed to be due to the severe serrations on the grip faces. Figure 35 shows the serrations on the grip face which are cut at a  $45^\circ$  angle and are 1.524 mm apart. A sample being tested needs to have a high enough hardness that the serrated points cannot deform the material enough to cause softening. The steel samples are hard enough not to be damaged by the grip serrations thus maintaining their integrity and not softening under the grip pressure. Aluminum is a softer material than steel and thus deforms more in the grips than steel. The fiberglass samples are softer still and are crushed in the grips which softens the material. Lighter pressures were used on some fiberglass tests but it did not make a difference. The serrations on the grip faces seem to be inadequate for rigidly gripping fiberglass or even aluminum. The large errors of the fiberglass samples shown in Figure 52, Figure 53, and Figure 54 could be accounted for in large part due to gripping effects. Apart from the severity of the grip serrations, a balance needs to be struck between gripping pressure and grip slippage. This is a balance that changes with the material being gripped. The key is to balance the gripping pressure and texture of the grip surface to minimize grip induced stresses and sample slippage. This is an area for future effort.

Coguill and Adams [19] have presented work in this area that could help in resolving the issue.

### Load Readings

The absolute standard deviation data in Table 2 show that the precision error of loads  $F_y$  are worse than the error of loads  $F_x$  for a given applied load and the data from Figure 42 show that  $M_z$  moment errors are again worse than both. This error will be examined by following the signal from the load cells until the loads are resolved into their component loads. A discussion of the accuracy of the resolved loads then follows.

### Precision of Load Readings

The question that arises by examining the data in Table 2 is which of the absolute or relative standard deviation values is more constant over the range of the loads and consequently which is more pertinent to a discussion on load precision. Figure 55 contains a log scale plot of relative standard deviation percent values versus the magnitude at which the standard deviation values were read. This is data taken with Omega DMD-465 load cell amplifiers that replaced the amplifiers built in-house. A/D conversion is done with a 16 bit converter. These are modifications discussed later on.

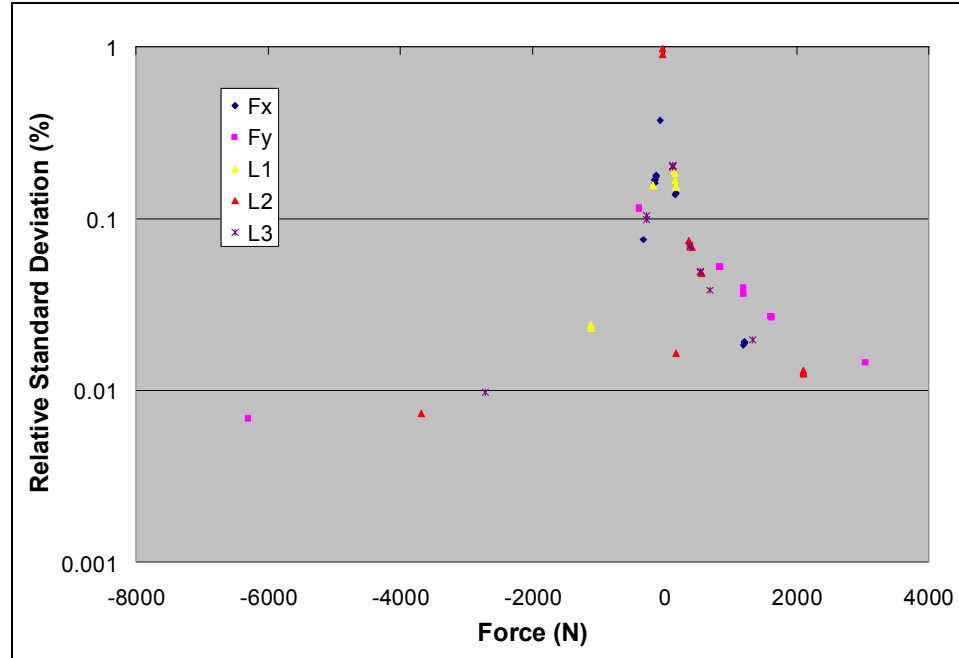


Figure 55. Log scale plot of relative standard deviation versus the force at which the data was taken. Standard deviation taken with 20,000 readings per data point

The relative standard deviation values are not constant versus the force values at which they were taken. This gives good evidence that load precision error is best discussed with reference to absolute standard deviation values. The same data plotted as absolute standard deviation values is shown in Figure 72. Given that absolute standard deviation values are more pertinent, the following discussion addresses these precision errors as absolute errors (not dependant on the applied load). The setup discussed is before any modifications were made to the load acquisition hardware.

The load cells are rated to a repeatability error of  $\pm 0.03\%$  full scale which makes them adequately precise and they conform to ASTM testing standards of  $\pm 1\%$  error provided the data acquisition and amplifiers don't decrease the precision and the accuracy errors are within  $\pm 1\%$  [15].

The load cells are connected to amplifiers built in-house which are in turn connected to the National Instruments UMI-7764 Accessory, which is connected to the NI PCI-7344 Device. The PCI-7344 Device is 12 bit which gives it 4096 binary values over the range of the full-scale input voltage and converts the signal from analog to digital. It has input voltage range settings of -10 V to +10 V, 0 V to +10 V, -5 V to +5 V, and 0 V to +5 V. The full-scale load of the load cells is  $\pm 8896$  N which means the maximum resolution that the PCI-7344 Device can distinguish is  $8896 \text{ N}/2048 \text{ bins} = 4.34 \text{ N/bin}$  (the load cells are 8896 N tension and  $-8896$  N compression). This resolution is possible if the full-scale voltage signal from the load cell is amplified to the full-scale voltage range setting of the PCI-7344 Device.

The data in Table 2 show that the average of the absolute standard deviations of loads 1, 2, and 3 is 16.3 N. This is 3.8 times higher than the possible 4.34 N resolution if the amplifier adds no error (Table 4). Thus, the amplifier could be the main culprit of precision error in the loads.

Additional error accumulates by resolving the loads into their components. Referencing Figure 16, load cells 2 and 3 (attached to the ends of actuators 2 and 3) are nearly aligned with the  $y$  axis. Load cell 1 (attached to actuator 1) is rotated roughly  $135^\circ$  from the  $+x$  axis. When force 1 from load cell 1 is resolved into its  $x$  and  $y$  components,  $F_x$  is equal to the force times the cosine of  $135^\circ$  ( $\cos(135^\circ)=-0.7071$ ) and  $F_y$  is equal to the force times the sine of  $135^\circ$  ( $\sin(135^\circ)=0.7071$ ). Both components are thus the force scaled by  $\sim 0.7$ . The force from load cell 2 is scaled by the cosine of about  $90^\circ$  ( $\cos(90^\circ)=0$ ) to get  $F_x$ .  $F_y$  is obtained similarly but with the sine of  $90^\circ$  ( $\sin(90^\circ)=1$ ).  $F_x$

and  $F_y$  for load cell 3 are obtained the same way. These components are then summed over the three load cells to get the total  $F_x$  and  $F_y$ . As the forces are scaled into their components, the errors in the forces are also scaled. Thus for load 1, the error contribution in the  $x$  direction is about the same as in the  $y$  direction. The error contributions to  $F_x$  from loads 2 and 3 are nearly zero and the error contribution to  $F_y$  from loads 2 and 3 is nearly the sum of the entire error of loads 2 and 3. This produces a larger standard deviation in  $F_y$  than in  $F_x$ .

This same concept can also apply to the accuracy of  $M_z$ .  $M_z$  is obtained by multiplying the load from each load cell by its respective moment arm (measured from the center of the sample to the line of action of the force). These moment arms magnify the error. The standard deviation for load cell 1 (16.3 N) is multiplied by moment arm 1 (0.56 m). This is an error of 9.128 N-m. This is added to the error from load cell 2 (16.3 N \* 0.34 m = 5.53 N-m) and then to the error from load cell 3 (16.3 N \* 0.43 m = 7.05 N-m). The total error is 21.7 N-m. This is a worst-case scenario since in practice the errors can cancel each other just as well as add together (21.7 N-m is larger than the standard deviation of 9.21 N-m). The data in Figure 42 show that errors of 21.7 N-m do happen if no averaging takes place.

If the amplification and load cell errors can be neglected and the same 12-bit A/D converter is used, maximum  $F_x$  errors could be the error from load 1 (4.34 N) times the cosine of the angle actuator 1 makes with the  $x$ -axis ( $0.7 + 0 + 0$ ) which is 3.04 N. Maximum  $F_y$  errors could become the component errors from loads 1, 2, and 3 ( $0.7 + 1 + 1$ ) times the resolution from the PCI-7344 Device ( $4.34 \text{ N} * 2.7 = 11.72 \text{ N}$ ). Maximum

$M_z$  errors could become the error from loads 1, 2, and 3 (4.34 N) times the moment arms 1, 2, and 3 (0.56 m + 0.34 m + 0.43 m = 1.33 m) which equals 1.78 N-m; much better than the error of 21.7 N-m that happens with the in-house built amplifier.

There is the possibility of acquiring the loads through the SCXI chassis and 16-bit PCI-6034E DAQ Device. If this were done the precision would increase even more than that calculated with the 12 bit A/D converter. Table 4 contains a summary of the differences in errors between the setup with the in-house built amplifier and 12 bit A/D conversion, the setup with negligible amplifier errors and 12 bit A/D conversion, and the setup with 16 bit A/D conversion.

Table 4. Summary of current load errors and potential minimized load errors

	Absolute standard deviation with precision errors from load cells, in house built amplifier, and 12 bit A/D conversion	Potential precision errors due to 12 bit A/D conversion with negligible error from load cells and amplifier	Potential precision errors due to 16 bit A/D conversion with negligible error from load cells and amplifier
Load 1	12.87 N	4.34 N	0.27 N
Load 2	18.14 N	4.34 N	0.27 N
Load 3	17.85 N	4.34 N	0.27 N
F <sub>x</sub>	10.82 N	3.04 N	0.19 N
F <sub>y</sub>	28.16 N	11.72 N	0.73 N
M <sub>z</sub>	9.21 N-m	1.78 N-m	0.36 N-m

A typical tension or shear test is expected to reach loads in excess of 5000 N whereas a moment test will reach upwards of 120 N-m. Since the current  $F_x$  and  $F_y$  errors shown in Table 4 are such a smaller percentage of the maximum test loads than the error of  $M_z$ , the need to increase the precision of  $F_x$  and  $F_y$  is not as great as the necessity to increase the precision of  $M_z$ .

#### Accuracy of Resolved Loads

Relative Percent Error Figures. The ASTM standard for force verification of testing machines specifies conformance as being  $\pm 1\%$  error for the entire range of the load [15]. Given this standard, none of the resolved load components are in compliance. The data in Figure 47, Figure 49, and Figure 51 show that percent errors are large initially and then drop off as the loads get large.  $F_x$  and  $F_y$  loads converge to precise percent error values as the loads get large whereas  $M_z$  loads do not converge as much. The imprecision of  $M_z$  loads could be the cause of this.  $F_y$  percent errors converge much later than do the  $F_x$  percent errors ( $F_y$  loads converge around 5000 N whereas  $F_x$  loads converge around 2000 N). This also could be caused by higher imprecision of  $F_y$  than  $F_x$ .

Absolute Load Error Figures. The data in Figure 46 show that the  $F_x$  load errors are about  $\pm 60$  N and the data in Figure 48 show the  $F_y$  load errors are between  $-50$  N and  $200$  N. The data in Figure 50 show that the  $M_z$  load errors are relatively high compared to a sample test, which has maximum moments around 120 N-m.

Beyond the precision errors discussed previously, the cause of these accuracy errors is due to friction. The errors shown in Figure 46 and Figure 48 are generally positive errors, which show that other loads are present other than those caused by pulling on the sample. There are a couple sources of friction between where the loads are measured and where the sample is located. The actuator pivot points have a bit of friction in the tapered bearings; however, it is assumed negligible. The major source of friction is the out-of-plane constrainer. This effect was shown in Figure 21 and is the reason that offset loads are subtracted in a test. The loads in Figure 46, Figure 48, and Figure 50 already have the offset loads subtracted. If the IPL tends to deflect out-of-plane, more friction is present in the out-of-plane constrainer. Out-of-plane deflection also causes side forces on the load cells due to the way the load cells are mounted. The load cells are allowed to pivot around the  $z$  axis but are constrained from rotating about the  $x$  and  $y$  axes.

In summary, friction is the major cause of load error mainly due to the out-of-plane constrainer. The error is made worse by out-of-plane deflection of the IPL, which causes more friction in the out-of-plane constrainer. Side loads on the load cells could also contribute to the error. Increasing the precision of the load readings using new amplifiers and the 16-bit A/D converter could decrease these errors. But even as such, the errors are not prohibitively large as to exclude testing -- especially tension and shear tests. The load errors are not considered a large cause of errors seen in the tension, shear, and compression tests since the  $F_x$  and  $F_y$  relative percent errors converge and the errors are scattered about this mean.

## Tension Tests

### Sensitivity to Material Properties

When doing FE analysis, as was done to validate the IPL sample tests, material properties play a large role. An error in material properties results in errors in either force or displacement results. To establish the relationship between material property error and force or displacement error, the plane stress constitutive equations of elasticity were examined. Isotropic materials were studied to simplify the relationships. This only required examining the effect that errors in the two independent elastic constants had on force or displacement. These of course are elastic modulus and Poisson's ratio. If transversely isotropic conditions were assumed, five elastic constants would be needed and if orthotropic conditions were assumed, nine elastic constants would be required.

The relationship between the elastic modulus ( $E$ ), Poisson's ratio ( $\nu$ ), and strain (which is proportional to displacement) is defined by the following equations (excluding the equation for strain in the  $z$  direction):

$$\epsilon_x = \frac{1}{E}(\sigma_x - \nu\sigma_y) \quad 13$$

$$\epsilon_y = \frac{1}{E}(\sigma_y - \nu\sigma_x) \quad 14$$

The strains are inversely proportional to  $E$  and proportional to  $\nu$  by  $C-\nu$  where  $C$  is a constant. Note that  $\nu$  is only a factor if there is an applied stress or strain perpendicular to the major strain direction (the perpendicular stress and perpendicular strain will subsequently be called the minor stress and strain respectively). Figure 56 contains a plot of Equation 14 where  $\epsilon_y$  is plotted versus  $E$  and  $\nu$ . The two stresses have equal

magnitude.  $E$  and  $\nu$  are varied by 50% in each direction around the standard values for aluminum.

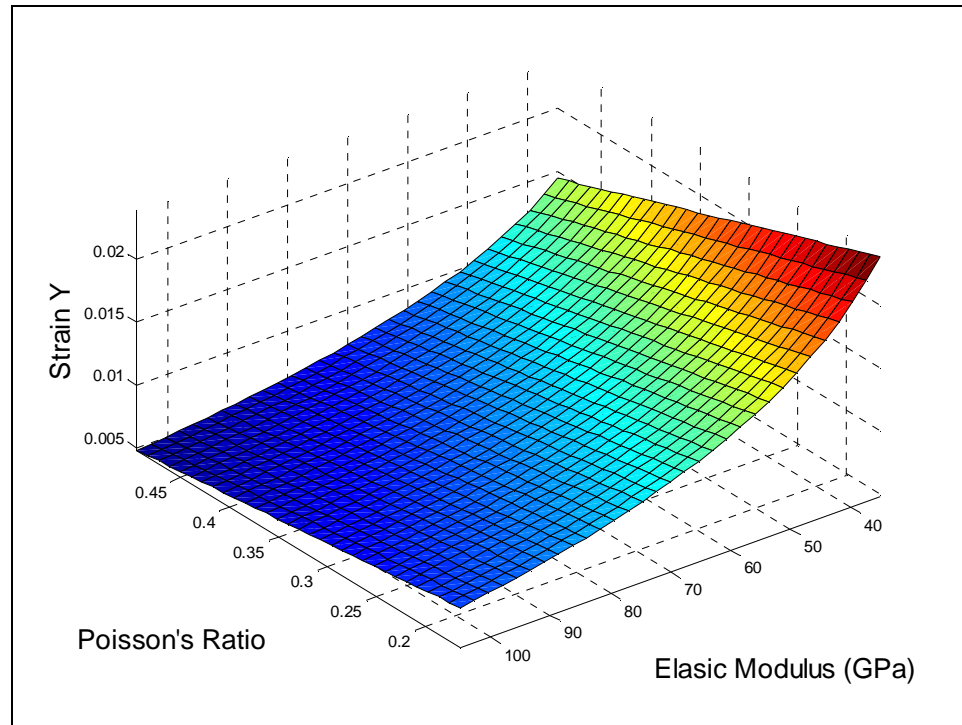


Figure 56.  $\epsilon_y$  versus  $E$  and  $\nu$  according to elastic constitutive plane stress equations.  $\sigma_x = \sigma_y$

If displacements are applied, the stresses (which are proportional to forces) are calculated by:

$$\sigma_x = \frac{E}{1-\nu^2} (\epsilon_x + \nu\epsilon_y) \quad 15$$

$$\sigma_y = \frac{E}{1-\nu^2} (\epsilon_y + \nu\epsilon_x). \quad 16$$

Here the stresses are proportional to  $E$ . Figure 57 contains a plot of Equation 16 where  $\sigma_y$  is plotted with respect to  $E$  and  $\nu$ . The two strains have equal magnitude.

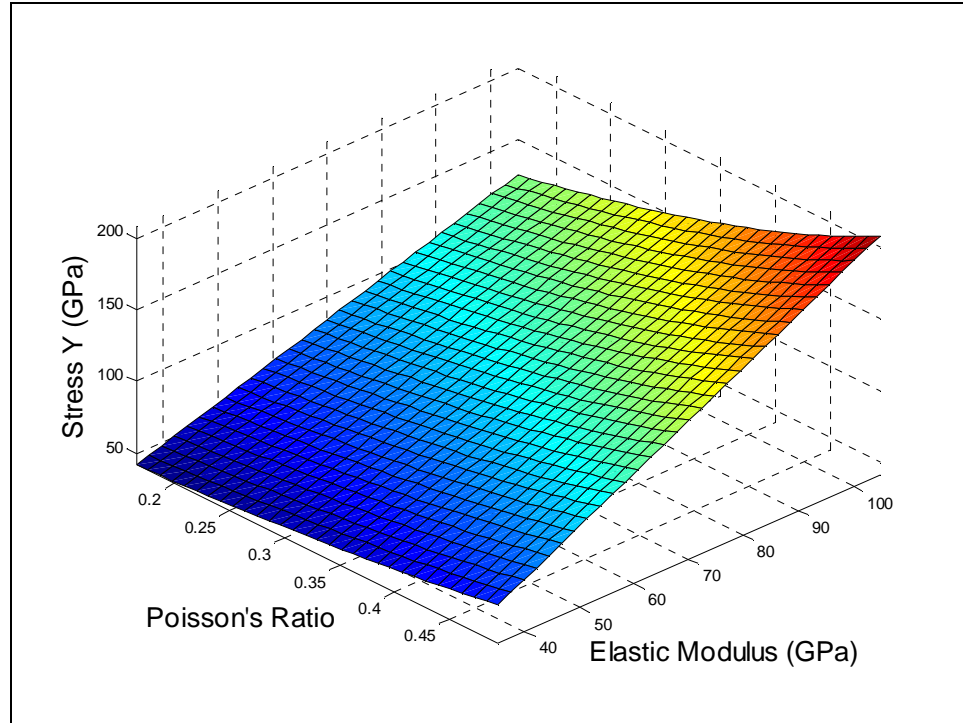


Figure 57.  $\sigma_y$  versus  $E$  and  $\nu$  according to elastic constitutive plane stress equations.  $\sigma_y = \sigma_x$

Supposing that  $E$  is 10% lower than the true modulus,  $\sigma_x$  and  $\sigma_y$  are equal, and  $\varepsilon_x$  and  $\varepsilon_y$  are equal, Equations 13 and 14 give major strains that are 11.1% higher. Major stresses for the same situation are proportional to the elastic modulus and are thus 10% lower. A 10% decrease in Poisson's ratio gives major strains that are 4.9% higher and major stresses that are 4.7% lower.

When the minor stresses are zero,  $\varepsilon_x$  and  $\varepsilon_y$  in Equations 13 and 14 have no dependence on  $\nu$  and major strains are inversely proportional to  $E$ . If  $E$  is 10% lower, then the major strains are again 11.1% higher. The major stresses in Equations 15 and 16 are 10% lower if  $E$  is 10% lower with zero minor strains. Major strains are not dependent on  $\nu$  when minor stresses are zero. If  $\nu$  is 10% lower in Equations 15 and 16 with no minor strains, the major stresses are 2.3% lower.

The data in Figure 58 and Figure 59 show the relationship between the percent difference of major stresses or strains due to 10% lower values of  $\nu$  as minor strains or stresses vary from zero to the same magnitude as the major strains or stresses.

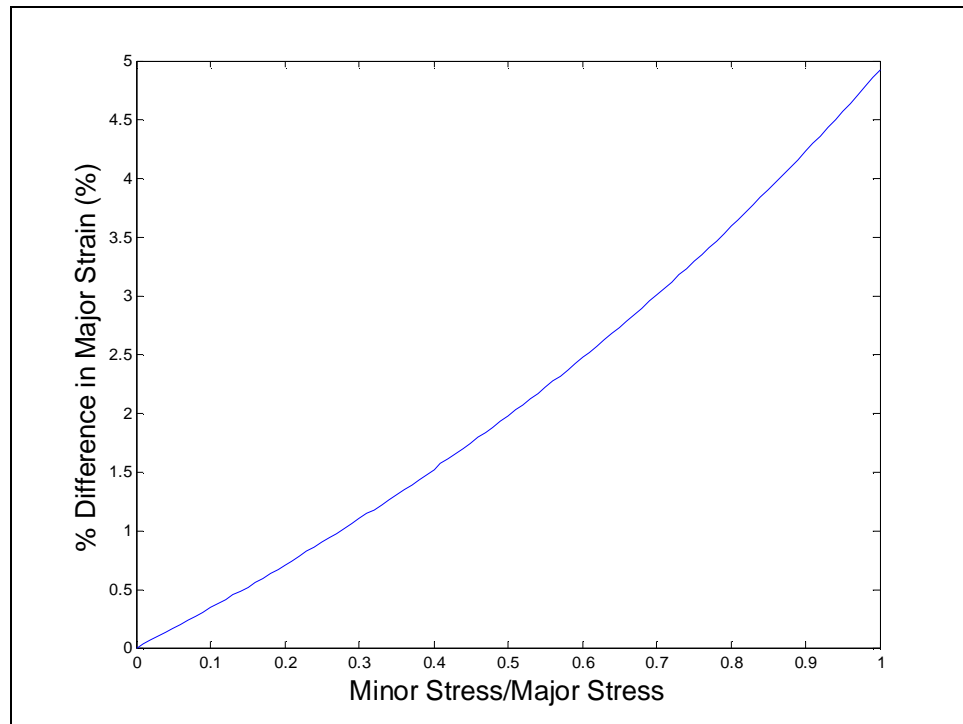


Figure 58. Percent difference in major strain due to a 10% lower Poisson's ratio as the ratio of minor to major stress varies

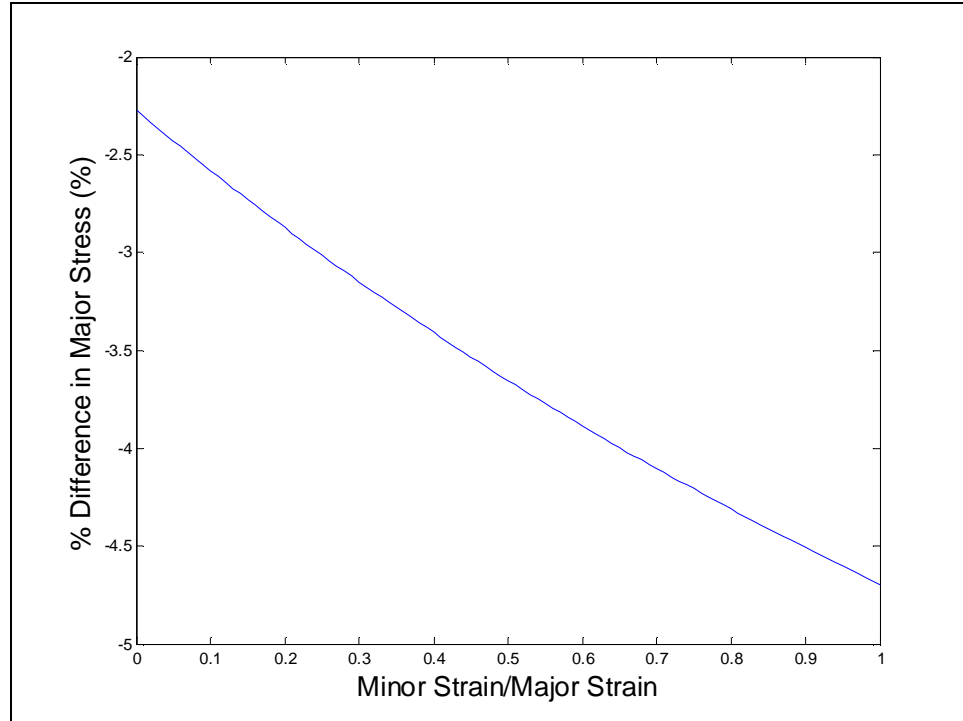


Figure 59. Percent difference in major stress due to a 10% lower Poisson's ratio as the ratio of minor to major strain varies

To apply this information to the tension, shear, and compression test data in Figure 52, Figure 53, and Figure 54, the effect of material property error on force divided by displacement needs to be investigated. If a strain is applied to a test sample and the corresponding stress is calculated, Equations 15 and 16 are essentially divided by a strain value which is a constant. This does not change the relationship between the material properties and the stresses and strains. Thus, the same trends seen in Figure 58 and Figure 59 apply.

The question then arises how the samples shown in Figure 66 and Figure 67 are affected by changes in Poisson's ratio or elastic modulus.

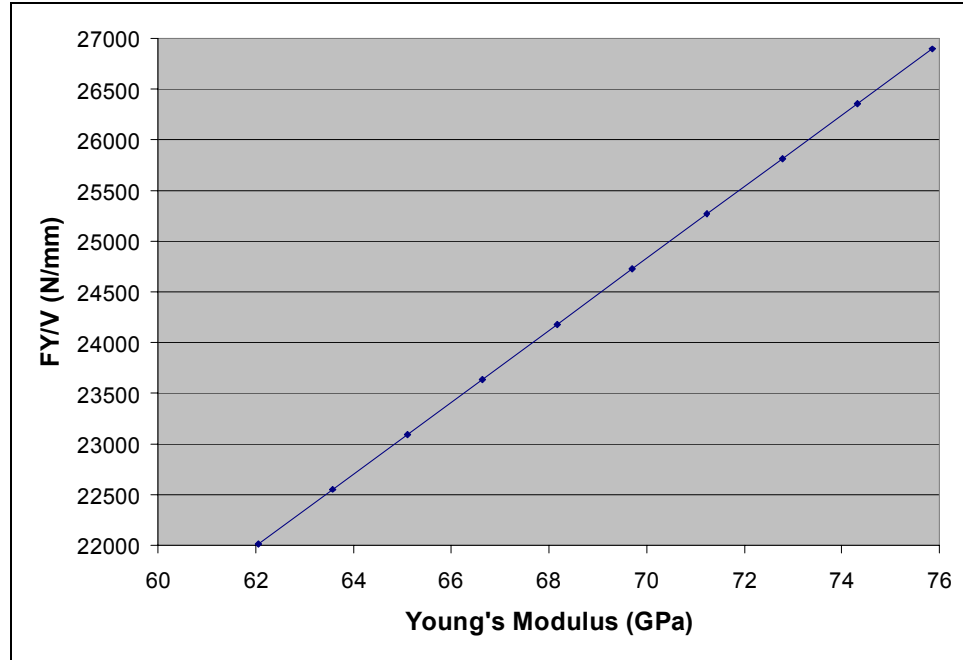


Figure 60.  $F_y/v$  as elastic modulus is varied 20% for the test coupons in Figure 66

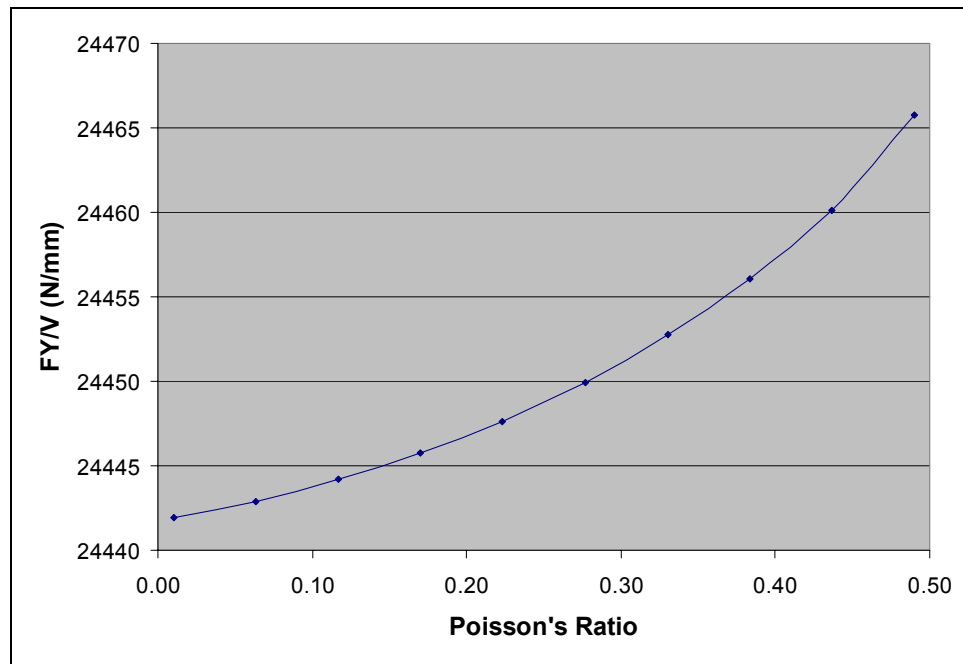


Figure 61.  $F_y/v$  as Poisson's ratio is varied for the test coupons in Figure 66

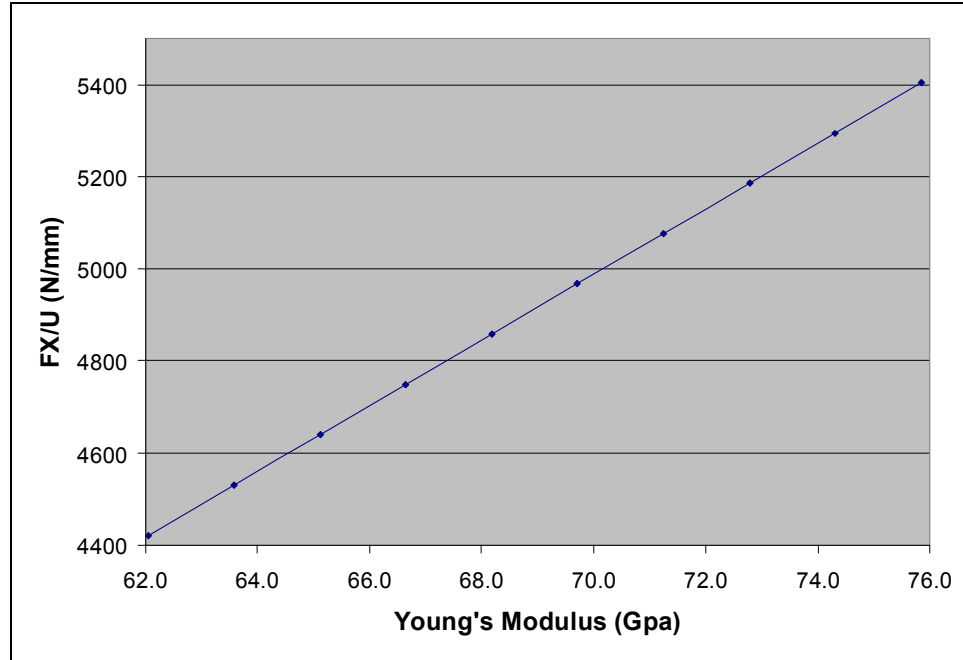


Figure 62.  $Fx/u$  as Young's Modulus is varied 20% for the test coupons in Figure 67

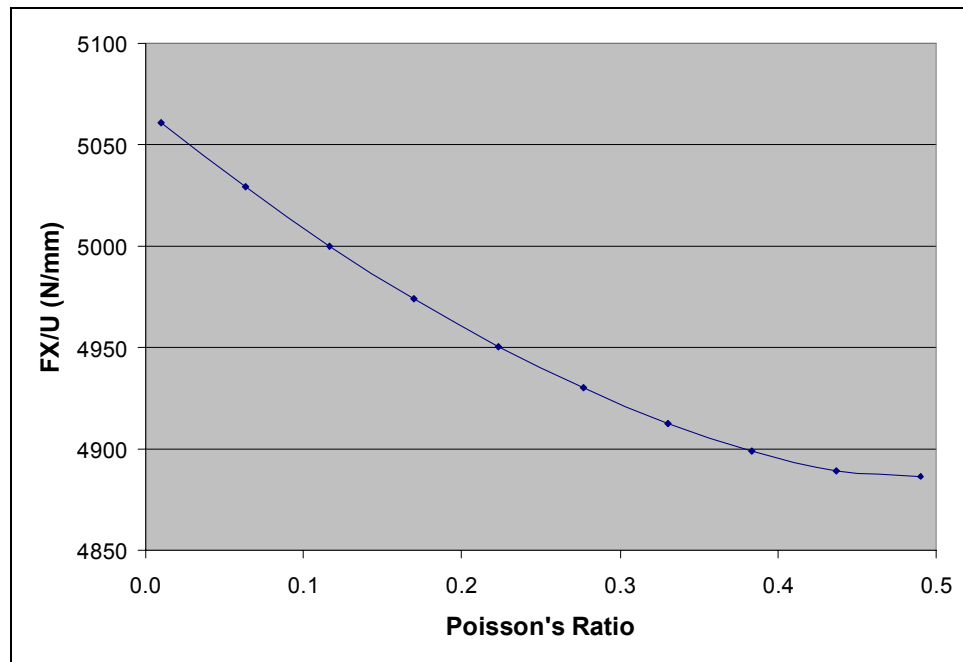


Figure 63.  $Fx/u$  as Poisson's ratio is varied for the test coupon in Figure 67

The data in Figure 60 show that  $Fy/v$  varies linearly with elastic modulus. Elastic modulus is varied  $\pm 10\%$  around the true modulus in Figure 60 and  $Fy/v$  varies by  $\pm 10\%$  as well. The same situation applies to the shear test data shown in Figure 62.

The data in Figure 61 show how  $Fy/v$  varies as Poisson's ratio varies from 0 to 0.5 for a pure tension test on the sample shown in Figure 66. There is not much of an effect on the magnitude of  $Fy/v$  even though the trend is similar to the relationship between major stress and Poisson's ratio shown in Figure 57. It is therefore safe to conclude that an error in Poisson's ratio has little effect on the error in a tension test.

The data in Figure 63 show an inverse relationship as the data in Figure 61. It seems that as Poisson's ratio increases, sample stiffness decreases if the sample experiences large shear stresses. Even so, the magnitude of change in sample stiffness is very small for a large change in Poisson's ratio and does not affect the error in a shear test much.

The conclusion of this study on the effects of material properties on sample tests is that a change in the elastic modulus has either a linear or nearly linear effect on the force or displacement and a change in Poisson's ratio has little effect on the results of a test.

### Optimized Coupon Geometry

Given Figure 52, there should be a coupon geometry that has low enough stiffness to give errors less than 10% in a tension test for aluminum or steel samples. Ritter [7] has proposed a coupon geometry that is reprinted here for clarity (Figure 64).

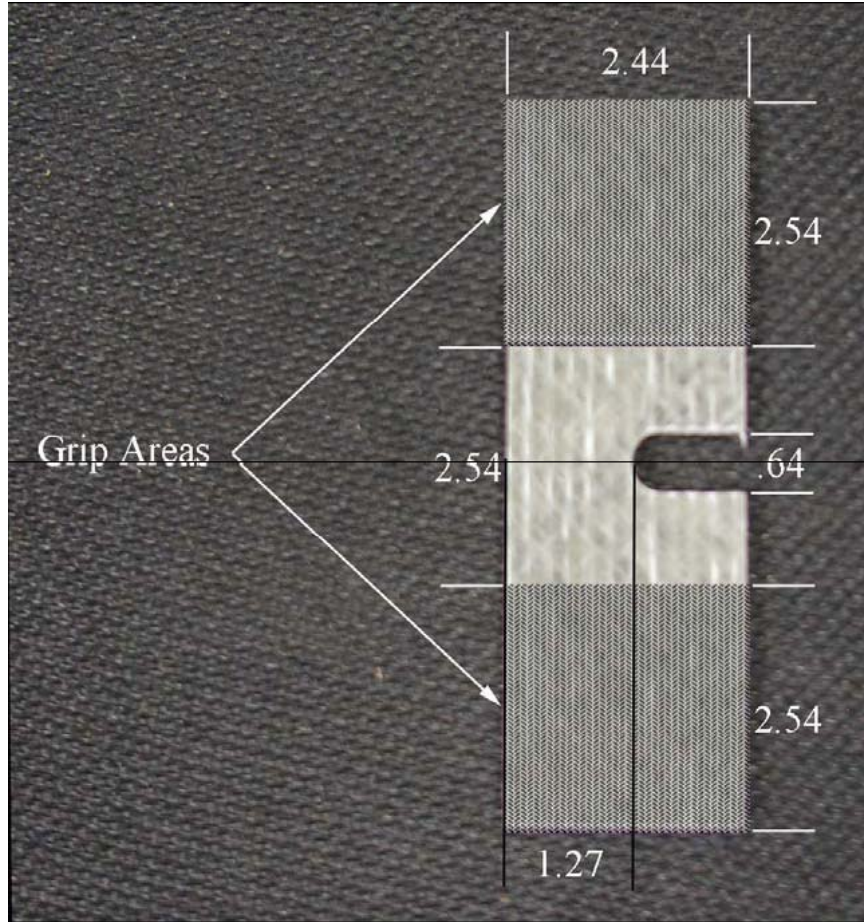


Figure 64. IPL coupon geometry [7]

The coupon is notched on one side which locates failure away from the grips. In keeping with this basic coupon design, a similarly shaped coupon was designed that took into account the tension testing results of Figure 52. Aluminum was used for this coupon design since fiberglass results were not as predictable. Steel could have been used also. One change from the coupon in Figure 64 was to have two notches on the coupon instead of one. This avoided any moment reactions in a pure tension test. The design was developed with an ANSYS [17] FEA optimization scheme (Appendix C). This involved building a model parametrically, meshing, applying boundary conditions and loads, solving, and then specifying constraint or state variables in the postprocessor. An

optimization scheme was then called which specified the parameters to vary (called the *design variables*), which to use as constraints (the *state variables*), and which to minimize (the *objective function*). Optimization looping was then done which varies the design variables according to a specified optimization method until the constraints of the state variable were met and subsequently the objective function was minimized. The design variables for the optimized coupon geometry were the width of the notched section of the coupon and the thickness of the coupon (marked as DV in Figure 65). These two design variables were chosen because they were two parameters easily modified although others could have been used. The minimum thickness was limited to 3.175 mm since thinner samples are not realistic for a testing coupon since they don't represent the macromechanical properties of engineering materials. The state variable was the applied force divided by the boundary displacement. The maximum value was constrained to be 25,000 N/mm. As shown in Figure 52, this value should give an error less than 10%. The objective function was the difference between 25,000 N/mm and the FEA model force/displacement results. The parameters not varied in the coupon were the length of the coupon (76.2 mm), the width (25.4 mm), and the radius of the notch (3.175 mm). The resulting coupon geometry is shown in Figure 65.

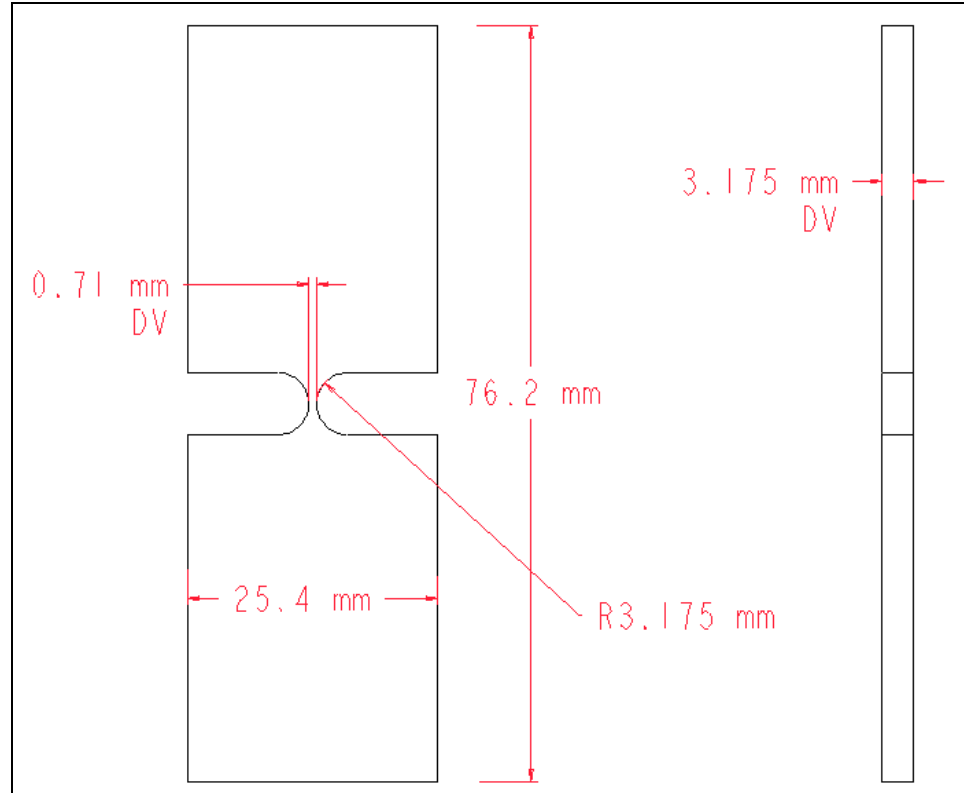


Figure 65. Impractical optimized coupon geometry for aluminum tension tests

The thickness of the coupon was 3.175 mm. This geometry is not very useful since the width of the notched section is less than 1 mm. This sample geometry had to be abandoned for something that is more practical. A longitudinal straight section in the notched section was added as shown in Figure 66. Here, the design variable is the length of the notched section.

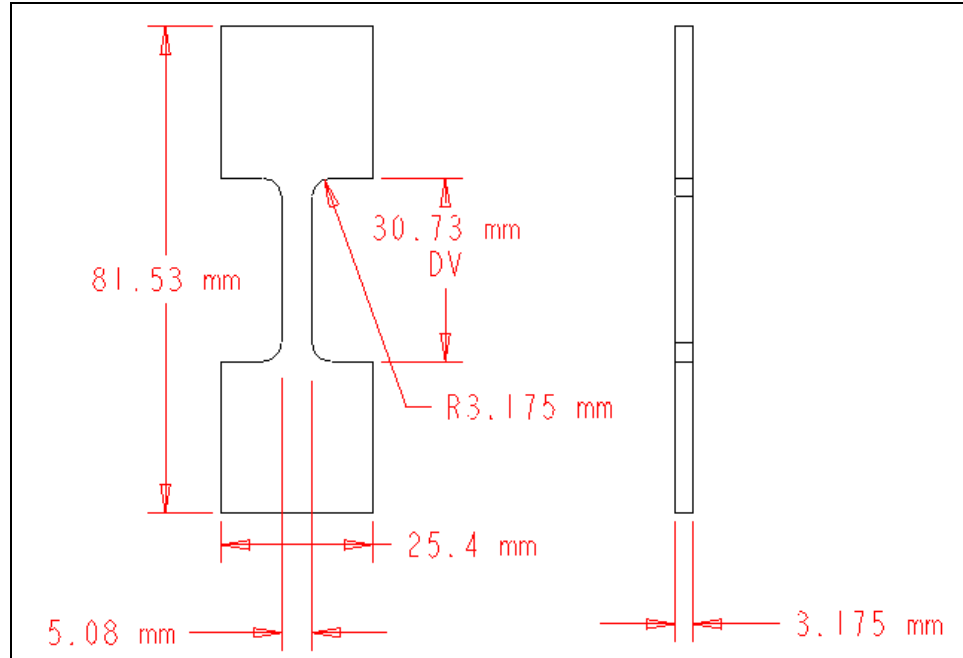


Figure 66. Practical optimized coupon geometry for aluminum tension test

### Shear Tests

The data in Figure 53 show that shear tests have much more error for a given sample stiffness than the tension or compression tests. In fact, for an equivalent error, the stiffness must be an order of magnitude less. Grip deflection cannot be blamed theoretically on any of the error since shear loading does not produce a three-point-bending situation. The error is mostly due to gripping effects and some out-of-plane deflection (aside from displacement reading and load reading errors). This puts even greater emphasis on having a gripping surface that holds the sample in shear.

The optimized sample geometry for shear tests was run with the same design variable as the tension test optimized coupon shown in Figure 66.

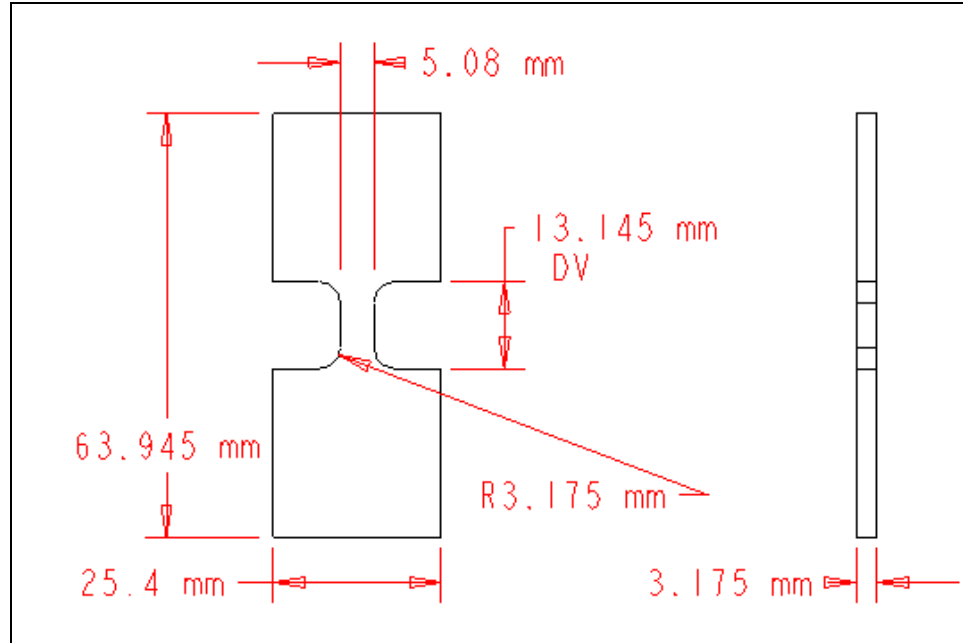


Figure 67. Optimized aluminum coupon for shear tests

This coupon was optimized for a  $Fx/u$  slope of 5000 N/mm. This should give an error of less than 10% according to Figure 53. It remains to be seen whether this coupon could work for a combined shear and tension test.

### Compression Tests

As mentioned previously, the compression test data is more scattered than the tension and shear test data (Figure 54). Out-of-plane deflection is the probable cause for this. The errors are generally negative however, which shows that out-of-plane deflection is not the only source of error in compression tests. Gripping effects also play a role.

The general trend of higher errors with increased sample stiffness is seen. The magnitudes are about the same as that of the tension tests: an error of 20% corresponds to a sample stiffness of around 100,000 N/mm. Consequently, an optimized coupon similar

to that shown in Figure 66 would work for a compression coupon, as well, as long as it did not buckle.

The true test of out-of-plane rigidity on an improved out-of-plane constrainer mechanism or rigid out-of-plane frame would be the accuracy of a compression test.

### Summary of Testing Results

The machine errors such as load and displacement precision and accuracy errors are much less than the errors shown in the tension, shear, and compression tests. The large errors in these tests must therefore be due to grip bending, out-of-plane deflection, and especially grip slippage.

## CHAPTER 7

## CURRENT CAPABILITIES OF THE IPL

Getting acceptable results from the IPL (defined to be errors less than 10%) is dependant upon three factors: the material being tested, the loading direction, and the sample geometry. These are somewhat interrelated so a list of acceptable and non-acceptable testing circumstances dependant on these factors is given. Thereafter is a summary of the main points of this paper.

Current Capabilities of the IPL

Testing composite samples in the current configuration requires care. This is twofold. 1) Tests must be conducted to ensure that grip slippage is negligible. This was determined to be a large source of testing variability for composites. 2) The severe serration on the grips needs to be mitigated since these can locally damage and crush the composite faces because of their low hardness, stiffness, and strength through the thickness compared to metals.

The IPL works well with steel samples and to a lesser extent aluminum (because of gripping effects) if the sample geometry provides a compliant enough sample. Errors less than 10% can be expected if the stiffness of the sample is less than 5000 N/mm for a shear test and less than 25,000 N/mm for a tension test. Samples that meet these requirements are shown in Figure 67 and Figure 66 respectively. If a combination of shear and tension are desired in a single test, then theoretically the sample geometry must

satisfy the respective stiffness requirements for each displacement direction although this needs to be verified by comparing tests with FEA.

Predicting the accuracy in compression tests is much more difficult than in shear or tension tests given the scatter of error data. This is due to the out-of-plane deflection of the IPL. It is therefore not advisable to do compression testing until a more rigid out-of-plane constraining method or mechanism is installed. This could be as simple as orienting the IPL horizontally. The combination of the out-of-plane constrainer and gravity could give enough out-of-plane rigidity to the IPL.

Moment tests were not advisable before the new load cell amplifiers were installed. They recently have been installed and so moment tests should be acceptable pending validation of the precision and accuracy data. A coupon configuration that has a low enough stiffness for moment tests also needs to be obtained.

A caveat to the testing allowances mentioned is that if a specific test is to be done, the force/displacement slope of an empirical test should always be compared to the FEA model. If this comparison yields acceptable errors then the test can be assumed valid in the non-linear region as well.

A summary of all testing conditions possible with the IPL is shown in Table 5 accompanied by a judgment of whether it is advisable or not to currently test that condition. If it is not advisable to test a particular condition, then a modification is recommended to enable testing.

Table 5. Current advisable and not advisable testing conditions and their caveats

<u>Testing Condition</u>	<u>Advisable</u>	<u>Caveat</u> <sup>1</sup>
Tension Test	Yes	<ul style="list-style-type: none"> <li>• Sample shown in Figure 66 is used</li> </ul>
Shear Test	Yes	<ul style="list-style-type: none"> <li>• Sample shown in Figure 67 is used</li> </ul>
Moment Test	?	<ul style="list-style-type: none"> <li>• Test is validated first.</li> <li>• The sample geometry satisfies stiffness threshold.</li> </ul>
Compression Test	No	<ul style="list-style-type: none"> <li>• IPL is mounted horizontal and out-of-plane deflection is minimized and verified.</li> <li>• Sample shown in Figure 66 is used.</li> <li>• No buckling occurs.</li> </ul>
Combination of Tension/ Shear/ Moment Test	?	<ul style="list-style-type: none"> <li>• Test is validated first</li> </ul>
Steel Sample	Yes	<ul style="list-style-type: none"> <li>• Appropriate sample geometry is used</li> </ul>
Aluminum Sample	Yes	<ul style="list-style-type: none"> <li>• Test is verified to be linear in the elastic region.</li> <li>• If not linear then grip effects present.</li> <li>• Appropriate sample geometry is used</li> </ul>
Composite Sample	? <sup>2</sup>	<ul style="list-style-type: none"> <li>• Grip faces are changed to have less severe serrations.</li> <li>• Grip effects are minimized and verified.</li> <li>• Appropriate sample geometry is used</li> </ul>
All Materials/ All Sample Geometry/ All displacements	No	<ul style="list-style-type: none"> <li>• Grip bending is minimized.</li> <li>• Out-of-plane deflection is minimized.</li> <li>• Moment load data is precise.</li> <li>• Gripping effects are minimized.</li> <li>• All tests are validated.</li> <li>• Appropriate sample geometry is used</li> </ul>

<sup>1</sup>A caveat for all tests is to use FE modeling to validate the results of a test

<sup>2</sup>A series of tests for typical load ranges is required to ensure that the specimen does not slip and that the specimen is not crushed by the grips

## CHAPTER 8

## RECOMMENDATIONS FOR THE IPL AND CONCLUSION

Some of the recommendations to correct the problems of the IPL are relatively simple and can be implemented without much cost or time. Others are quite extensive in both cost and time. Included in the following recommendations is a rating of where the modification lies on that cost and time scale.

Displacement Readings

The first step to be taken to improve the displacement measurements is to replace the LVDTs with higher accuracy models. Probe-style Macrosensor GHSAR 750 LVDTs have been purchased for this purpose (Figure 68).



Figure 68. Macrosensor GHSAR 750 LVDT [18]

They have a repeatability error of  $0.6 \mu\text{m}$ . The range is about 2.5 cm, much less than the Omega LVDTs currently being used. Implementing this modification would be somewhat time consuming but not otherwise costly since the new LVDTs are already purchased. The kinematic setup would have to be different than it is for the current LVDTs. The small travel and probe style of the Macrosensor LVDTs makes mounting the LVDTs on both ends (as it is now) much more difficult. A similar method to the

mounting method used by NRL could be implemented. In their method, a block is fixed to one grip on which the three LVDTs connected to the other grip slide (Figure 69).

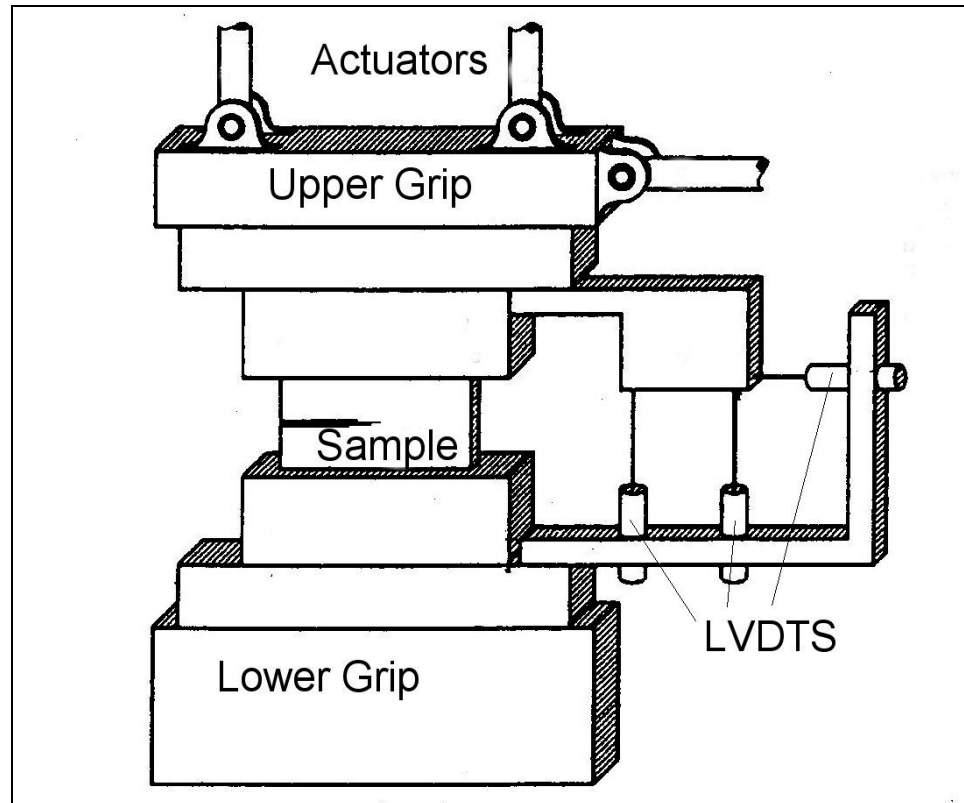


Figure 69. Schematic of the NRL IPL grips and LVDT setup [5]

Another advantage of the LVDT setup specified in Figure 69 is that it positions the LVDTs much closer to the sample than they are now. This decreases the effects of any deflection that occurs between the sample and the LVDT mounting points. However, this configuration could be difficult to resolve into  $u$ ,  $v$ , and  $\omega$  components, although preliminary work has already been done on this for the MSU IPL.

Another idea for mounting the LVDTs is to make a sample mounted mechanism that holds on to the sample via knife blades – similar to sample mounted extensometers.

Three small LVDTs would be attached to the mechanism and the kinematics would be resolved to get  $u$ ,  $v$ , and  $\omega$ .

The accuracy of the LVDT readings aside from the LVDTs themselves depends on the accuracy with which the LVDTs are mounted. Assuming the aforementioned LVDT setup is implemented, the position of the holding arm and sliding block shown in Figure 69 need to be known precisely. The precision needs to include the grip faces and the grip blocks as well.

#### Out-of-Plane Deflection

To minimize out-of-plane deflection of the IPL, a very rigid out-of-plane constrainer mechanism must be incorporated. This could be accomplished by mounting the actuators and grip assemblies between two large metal sheets (Figure 70).

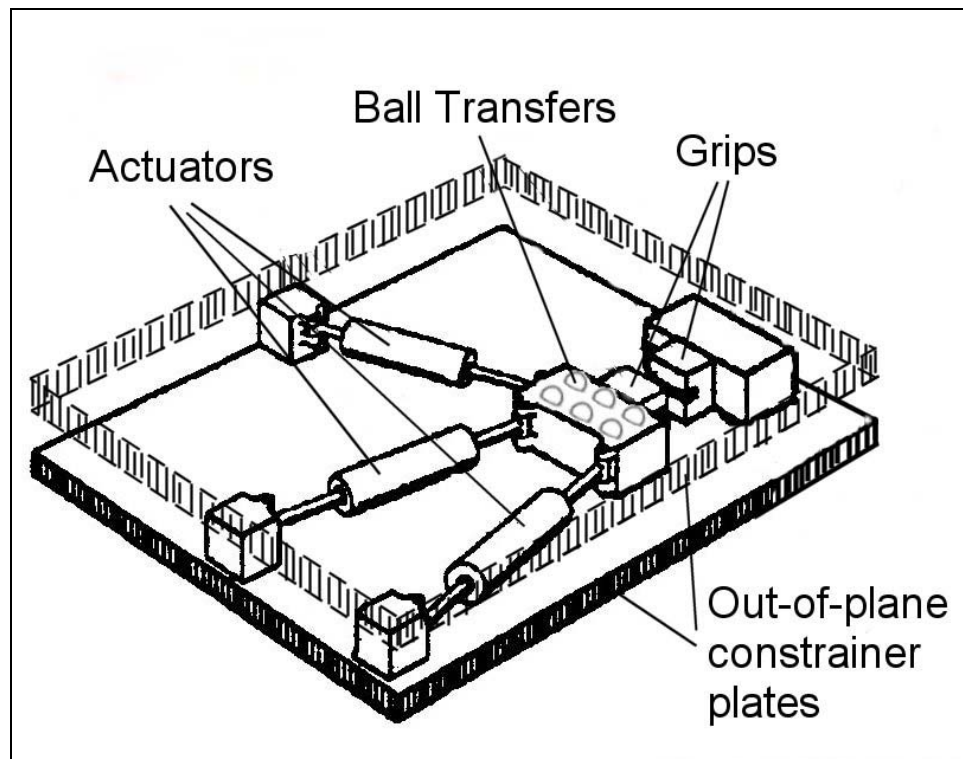


Figure 70. Proposed setup of the IPL to eliminate out-of-plane bending

One grip assembly would ride in between the metal sheets on ball transfers attached to the grip assembly mounting block. The other grip assembly would be fixed to the metal sheets. The grip assembly could have as many of these ball transfers attached as space permits to spread out the out-of-plane loads over the surface of the grip assembly mounting blocks in order to allow as little deflection as possible. This is a very costly and time-consuming modification. A less expensive alternative is to turn the present IPL frame horizontal to take advantage of gravity to constrain it in plane, although this will not eliminate all out-of-plane deflection.

#### Grip Deflection

To eliminate three-point-bending grip deflection, the grip faces must be fastened to the grip blocks through the center of the grip faces where the sample is gripped. This could be accomplished by fitting a square mating block in cavities located in the grip face and the grip block as seen in Figure 71. An interference fit could provide the attachment mechanism thereby requiring no further bolts.

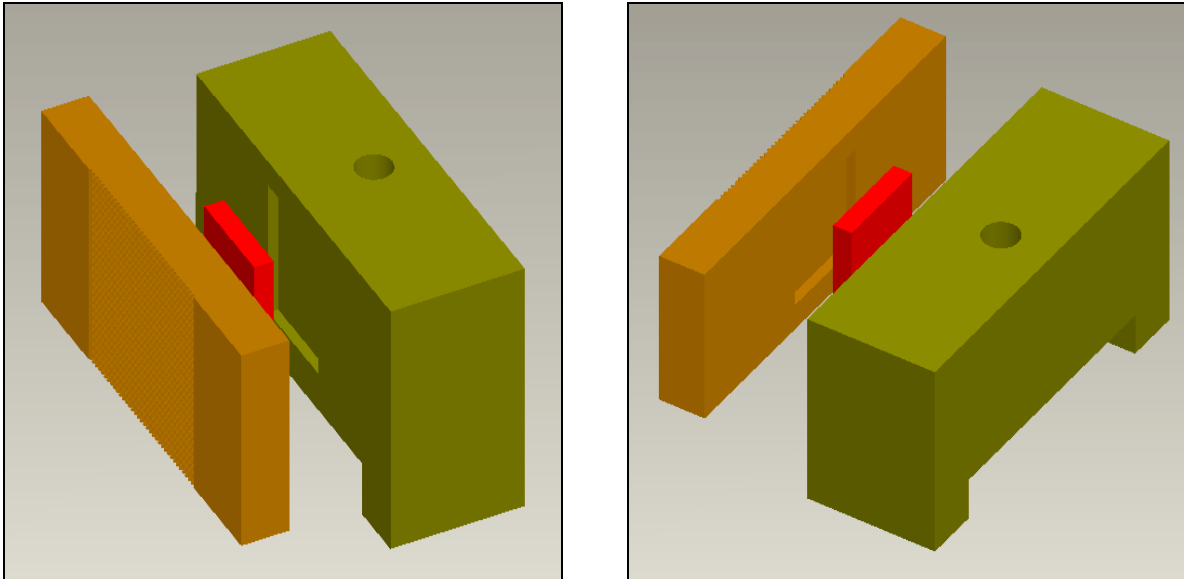


Figure 71. Press fit grip face assembly

This modification would entail making new precision-machined grip faces. The LVDT holding arms would have to be mounted to these grip faces as well.

### Gripping Effects

The gripping effects could be lessened in the composite and aluminum samples by increasing the number of serration points on the grip faces. This would spread out the gripping force on the sample thus limiting the amount of damage caused in the gripped area of the sample. This modification would require first investigating what grip surface works best for composite materials and then making new grips (silicon carbide coated grips that perform well testing composite materials have been studied by Coguill and Adams [19]). This is an involved modification if the new LVDTs are mounted on these new grips. If the same LVDT setup is used, then making new grips would not be too difficult.

Further investigation into the correct gripping pressure for a given material is warranted. A balance needs to be found between crushing the sample and preventing sample slippage.

### Load Readings

The main cause of precision error is the load amplifier. New load amplifiers would greatly decrease the load precision error. This would not be difficult to do. It would only involve buying three new amplifiers and wiring them to the load cells. While rewiring for the new load cell amplifiers, it would be easy to change the data acquisition task from the 12 bit UMI Accessory and PCI-7344 Device to the 16 bit SCXI Chassis and PCI-6034E Device. This could increase the load resolution for each load cell from about 16 N to less than 1 N.

The error in load readings could be decreased by decreasing the side loads on the load cells. Since the load cells are attached to the ends of the actuators, this could be accomplished by using ball joints to mount the ends of the actuators to the IPL frame. This would also relieve any side loads on the actuators and could be done on the current frame of the IPL. However, it would be difficult and would probably not be worth the small increase in load accuracy. It would best be left as a feature the new IPL frame discussed previously.

The inaccurate measuring technique used to acquire the actuator pivot points is also a cause of accuracy errors in the resolved loads. If a new frame is made, accurately measuring the actuator pivot point locations is a way to minimize resolved load error.

The moment arms used in calculating  $Mz$  magnify the errors from the load cell readings. If one end of the actuator was mounted closer to the sample, this would decrease the moment arms. This is a feature of the IPL schematic shown in Figure 70 and could be implemented along with a new out-of-plane constrainer frame design.

### Summary of Recommendations

The following is a list of the recommendations, starting with items that are easy to implement or imperative and ending with large and costly items.

- Buy new load cell amplifiers and install (complete as of 4-15-2006. Reference following section).
- Use the 16-bit SCXI chassis for data acquisition of the load cells (complete as of 4-15-2006. Reference following section).
- Make new grips with silicon carbide surfaces (in process).
- Investigate correct gripping pressures for composites (new hydraulics capable of 69 MPa installed as of 4-25-2006).
- Mount the grip faces through their centers instead of through the current mounting bolts.
- Orient the current IPL horizontally to allow gravity to keep the IPL in plane.
- Install the new LVDTs and mount them in a sliding contact configuration rather than having both ends pivot in ball joint rod ends.

- Build out-of-plane constrainer frame plates to sandwich the actuators and grip assemblies. Position all actuator mounting holes accurately to increase the accuracy of the resolved loads.
- Decrease the side loads on the load cells and actuators by mounting the actuators with ball joints. This is best left to a feature of a new IPL frame.
- Mount one end of the actuators close to the sample to decrease the moment arms. This is best left to a feature of a new IPL frame.

#### Procedure for Further Validation Tests

This thesis has attempted to enumerate the strengths and weaknesses of the IPL. It has been useful to quantify the accuracy and precision of the loads and displacements as modifications have been made. Continual validation studies are strongly recommended as more modifications are made. After a modification has been done, complete validation testing of the modified component is warranted to completely quantify the value of the modification and to provide a baseline for the next modification.

#### Recent Modifications

##### Load Cell Amplifiers and A/D Conversion

Since this initial study, some additional work has been performed on the IPL. The built in-house load cell amplifiers have been replaced by Omega DMD-465 amplifiers [20] and the load data acquisition has been changed to the 16 bit SCXI chassis from the 12 bit UMI accessory. Figure 72 contains loads 1, 2, 3 and  $F_x$  and  $F_y$  data from precision tests with the recent modifications. The data contained therein also show that absolute

standard deviation is relatively constant over the range of forces applied which discounts the usefulness of relative errors for precision data.

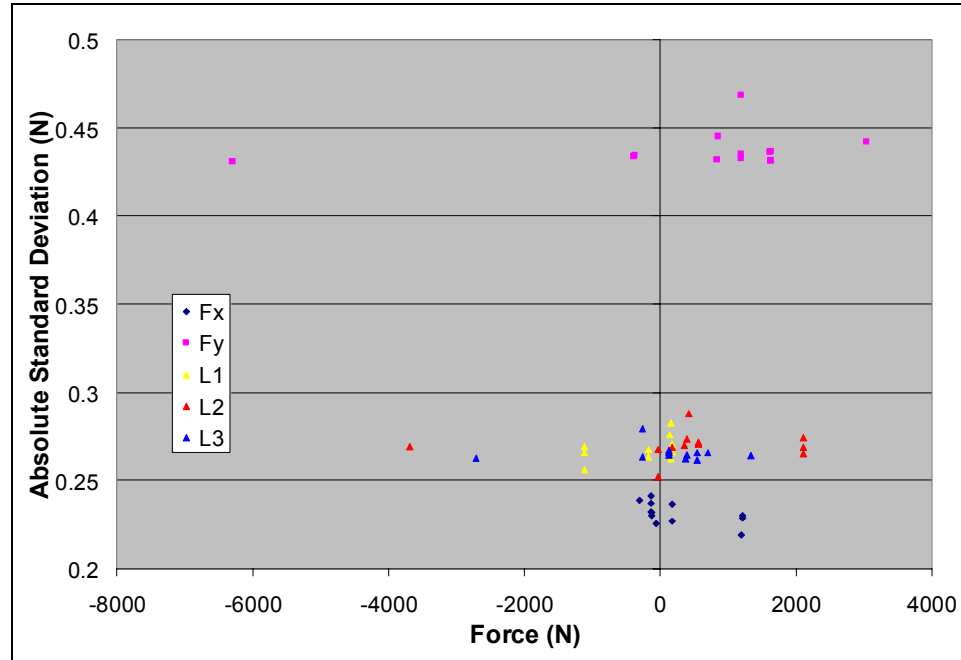


Figure 72. Absolute standard deviation versus force at which the data was taken. 20,000 readings were taken per data point

To summarize the progression of the load precision data, old (from Table 4), predicted, and new data are shown in Figure 73. The data are shown on a log scale plot because the new data are one to two orders of magnitude better.

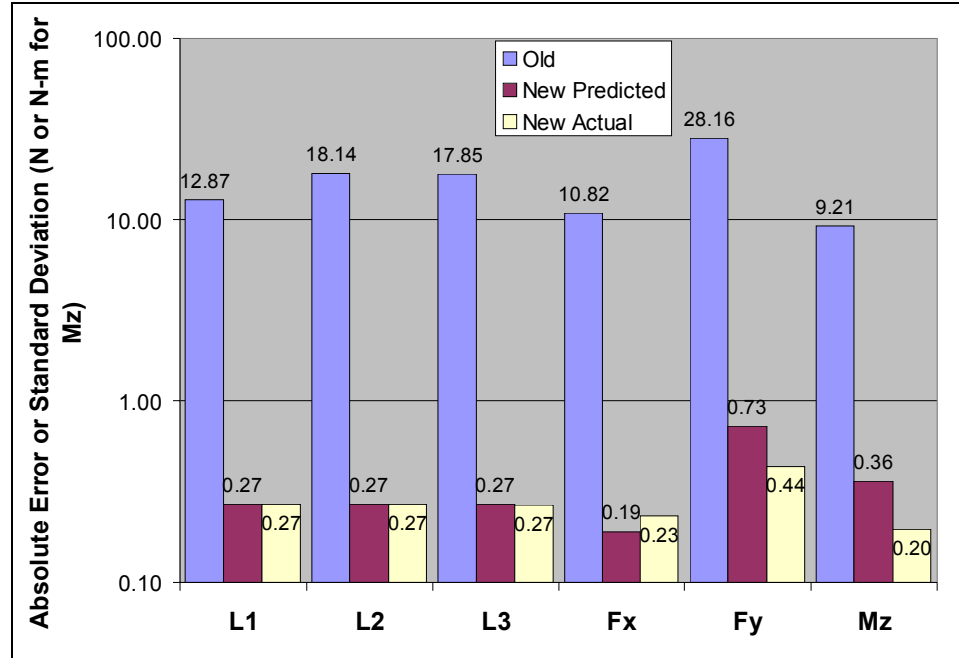


Figure 73. Old, predicted, and new load precision data on a log scale plot. Old load cell data was taken with in-house built amplifiers and 12 bit A/D conversion. New load cell data was taken with Omega DMD-465 amplifiers and 16 bit A/D conversion.

### New Grips and Higher Gripping Pressure

Grip slippage was shown to be a major problem with measuring displacement of a sample by measuring the displacements of the grips. This has been investigated further by following the recommendations of Coguill and Adams. SiC surfaces of 60 grit have been shown to work well with composite samples along with gripping pressures of around 69 MPa. A company called Carbinite Metal Coatings [21] has been identified that coats metal with carbide alloy resilient gripping surfaces. A free sample has been obtained shown in Figure 74.

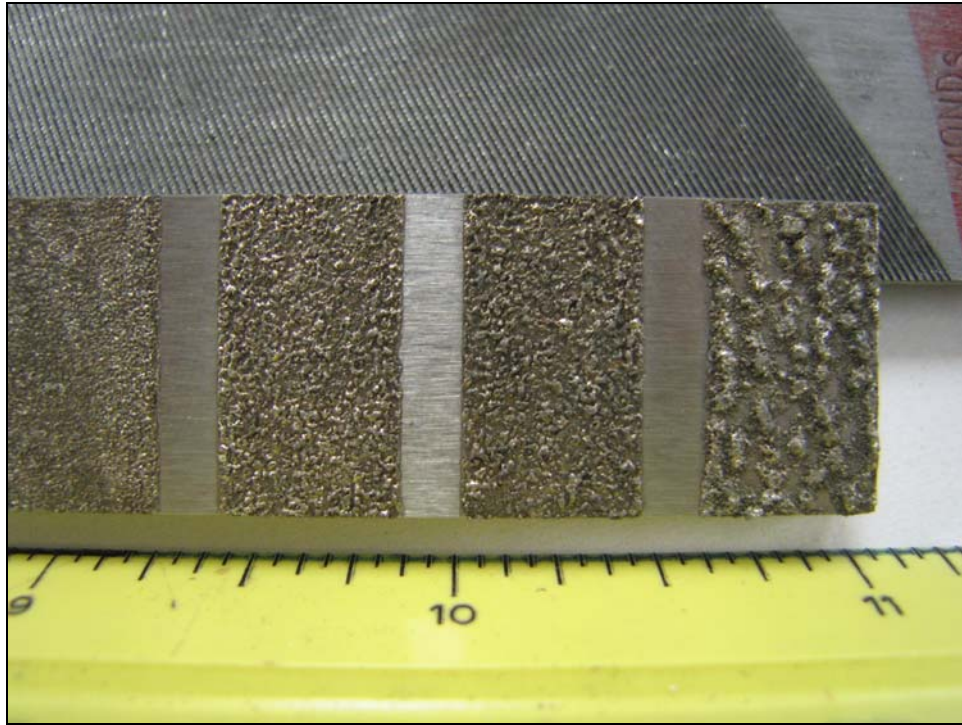


Figure 74. Sample of carbide alloy coated metal for gripping composites from Carbinite Metal Coatings

The hydraulic system installed on the IPL had a maximum rating of 20.7 MPa. This system has been replaced with a system capable of 69 MPa.

### Conclusion

Energy methods are very promising tools for predicting polymer composite material failure. A requirement to implement these methods is to have a substantial amount of empirical data that is unreasonable to obtain using a conventional uni-axial testing machine. The IPL, however, is a machine that can obtain the needed data. The ability to apply three different boundary displacements in a single test enables the IPL to be three times more effective at acquiring data than a conventional uni-axial testing machine. It is certainly worth the time and money to implement the modifications

previously outlined for the IPL to produce accurate empirical data. The IPL can aid in elevating composite research at Montana State University to the forefront of innovative composite design and analysis.

## REFERENCES

- [1] Dowling, Norman E. “Mechanical Behavior of Materials: Engineering Methods for Deformation, Fracture, and Fatigue.” 2<sup>nd</sup> Ed. New Jersey: Prentice Hall, 1999.
- [2] Swanson, S. R. “Introduction to Design and Analysis with Advanced Composite Materials.” Prentice Hall College Div, 1997
- [3] Wang, A.S.D. “Strength, Failure, and Fatigue Analysis of Laminates.” Engineered Materials Handbook, Vol. 1: Composites, ASM International, (1987) : 236-251.
- [4] Broek, David. “Elementary Engineering Fracture Mechanics.” Boston, MA: Martinus Nijhoff Publishers, 1986.
- [5] Mast, W. Phillip, Nash, Gerald E., Michopoulos, John, Thomas, Ray W., Badaliane, Robert, and Wolock, Irvin. “Experimental Determination of Dissipated Energy Density as a Measure of Strain-Induced Damage in Composites.” Naval Research Laboratory report NRD/FR/6383-92-9369. Washington, DC, 1992.
- [6] Booth, Eric, Schaff, Mark. “In-Plane Loader, a Multi-Axis Testing Machine.” Senior Design Project Report, Department of Mechanical and Industrial Engineering, Montana State University. 2001.
- [7] Ritter, William Joseph. “Application of Energy Methods to Modeling Failures in Composite Materials and Structures.” M.S. Thesis, Department of Mechanical Engineering, Montana State University, 2004.

- [8] Tsai, S. W., Wu, E. M. “A General Theory of Strength of Anisotropic Materials.” J. Composite Materials 5 (1971): 58-80.
- [9] Hahn, H. T., Erikson, J. B., and Tsai, S. W. “Characterization fo Matrix/Interface – Controlled Strength of Unidirectional Composites.” Fracture of Composite Materials. Ed. G Sih and V. P. Tamuzs: Martinus Nijhoff Pub, 1982.
- [10] Hashin, Z. “Failure Criteria for Unidirectional Fiber Composites.” J. Appl. Mech., 102 (1980):329-334.
- [11] Huang, Dongfang. “Constitutive Laws of Composite Materials via Multi-Axial Testing and Numerical Optimization.” M.S. Thesis, Department of Mechanical Engineering, Montana State University, 2003.
- [12] Labview is measurement and automation software available from National Instruments. 512-683-8411. [www.ni.com](http://www.ni.com).
- [13] Matlab is mathematics software available from The Mathworks. 508-647-7000. [www.mathworks.com](http://www.mathworks.com).
- [14] ASTM E 83-02. “Standard Practice for Verification and Classification of Extensometer System.” ASTM International, 2002.
- [15] ASTM E 4-03. “Standard Practices for Force Verification of Testing Machines.” ASTM International, 2003.

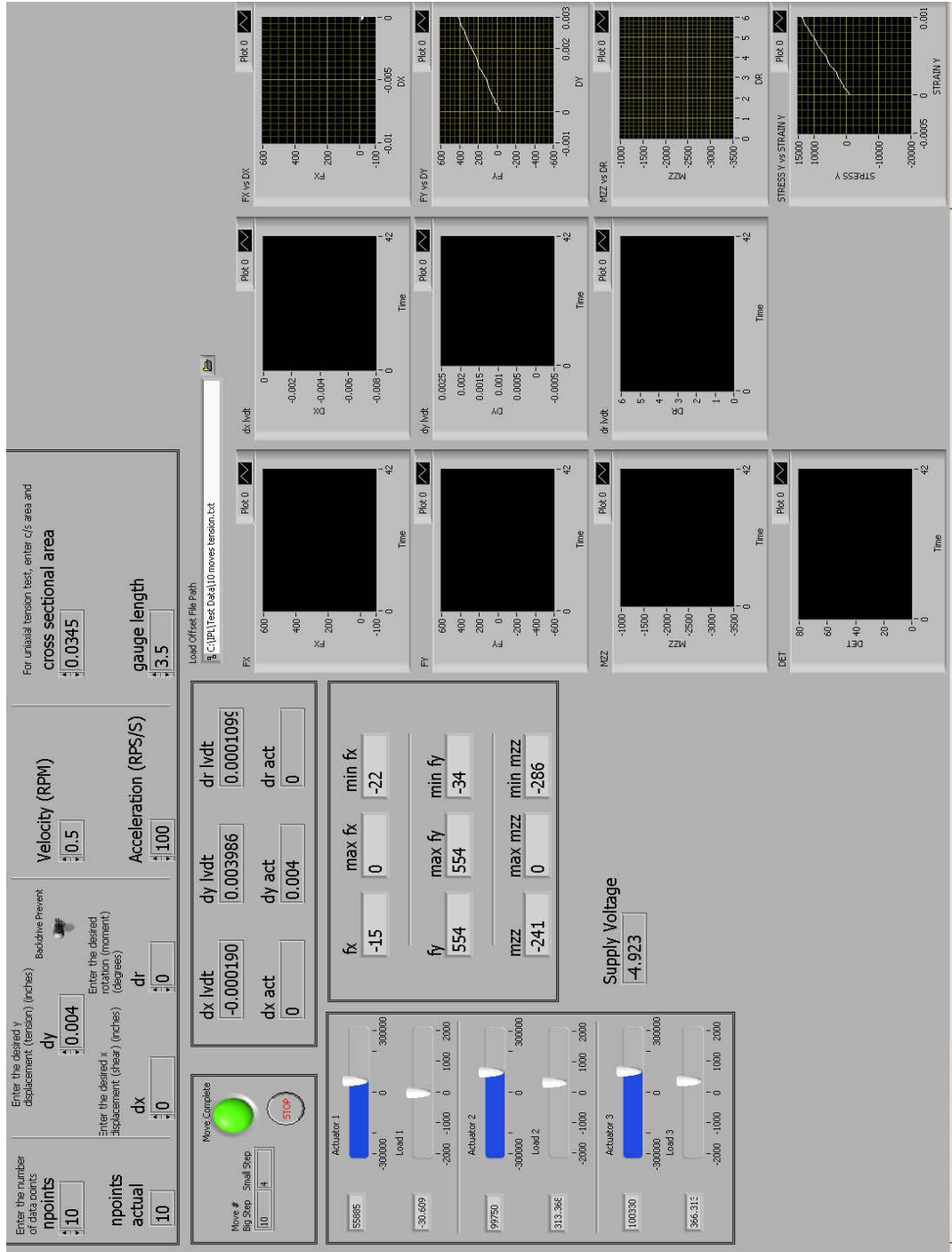
- [16] Young, Warren C., Budynas, Richard G. "Roark's Formulas for Stress and Strain." 7<sup>th</sup> Ed. McGraw Hill, 2002\
- [17] Ansys is finite element software available from Ansys Inc., 724-514-3304. [www.ansys.com](http://www.ansys.com).
- [18] Macrosensors is a division of Howard A. Schaevitz Technologies, Inc. 856-662-8000. [www.macrosensors.com](http://www.macrosensors.com).
- [19] Coguill, R, Adams, D. F. "Selection of the Proper Wedge Grip Surface for Tensile Testing Composite Materials." Composite Materials Research Group, University of Wyoming, Laramie. Presented at the SAMPE Conference, 1999.
- [20] Omega DMD-465 amplifier. <http://www.omega.com/pptst/DMD-465.html>. 1-800-USA-WHEN.
- [21] Carbinite Metal Coatings. [www.carbinite.com](http://www.carbinite.com).

APPENDICES

APPENDIX A

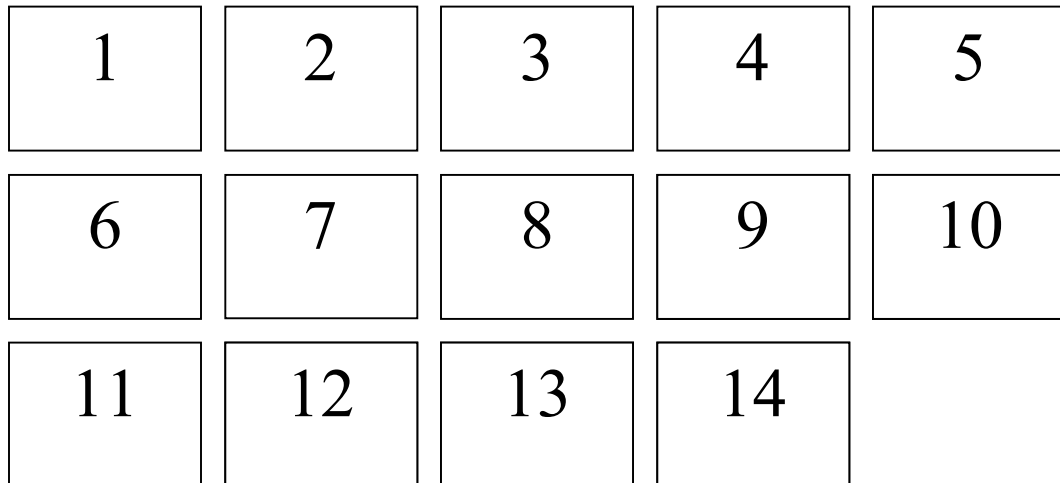
LABVIEW CODE

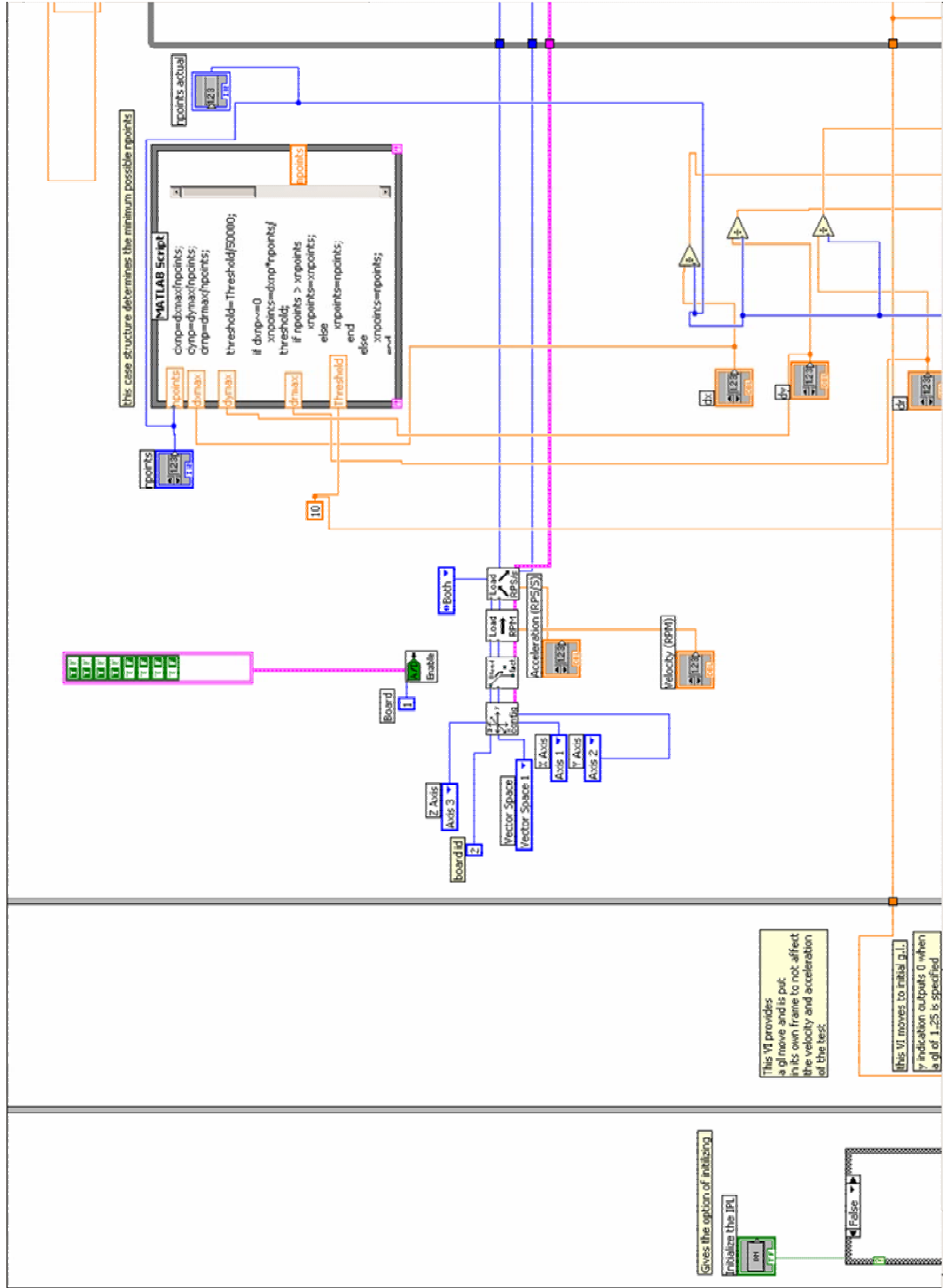
Labview Front Panel

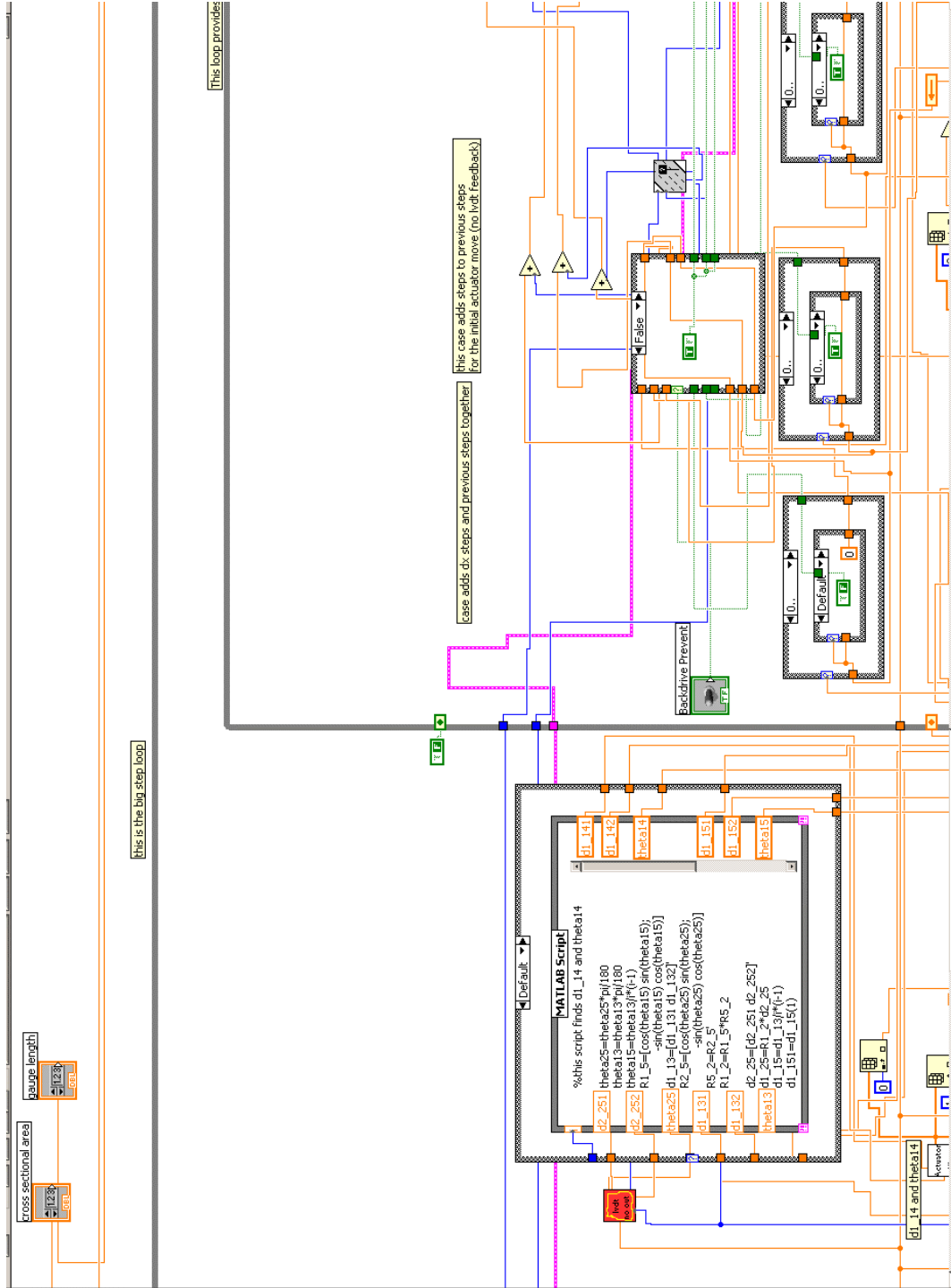


Labview Block Diagram

Graphical programming languages such as Labview can be easy to use since a visual inspection shows data flow. However, presenting code is not as easy as linear programming; Labview code can be spacious and unwieldy. To help organize the following block diagram, a map is supplied which shows the assembly of the block diagram sheets. This block diagram is the main program (VI) that controls a test with LVDT position controlled feedback. No attempt has been made to show all the sub VIs as that would require a book unto itself.

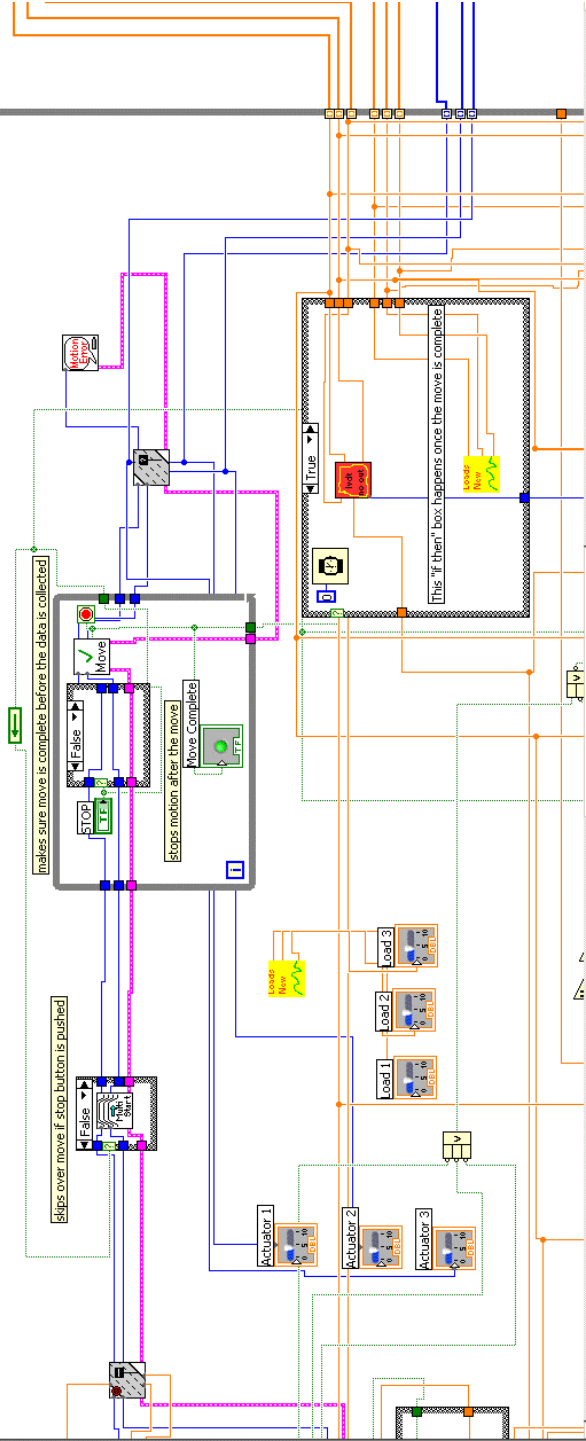


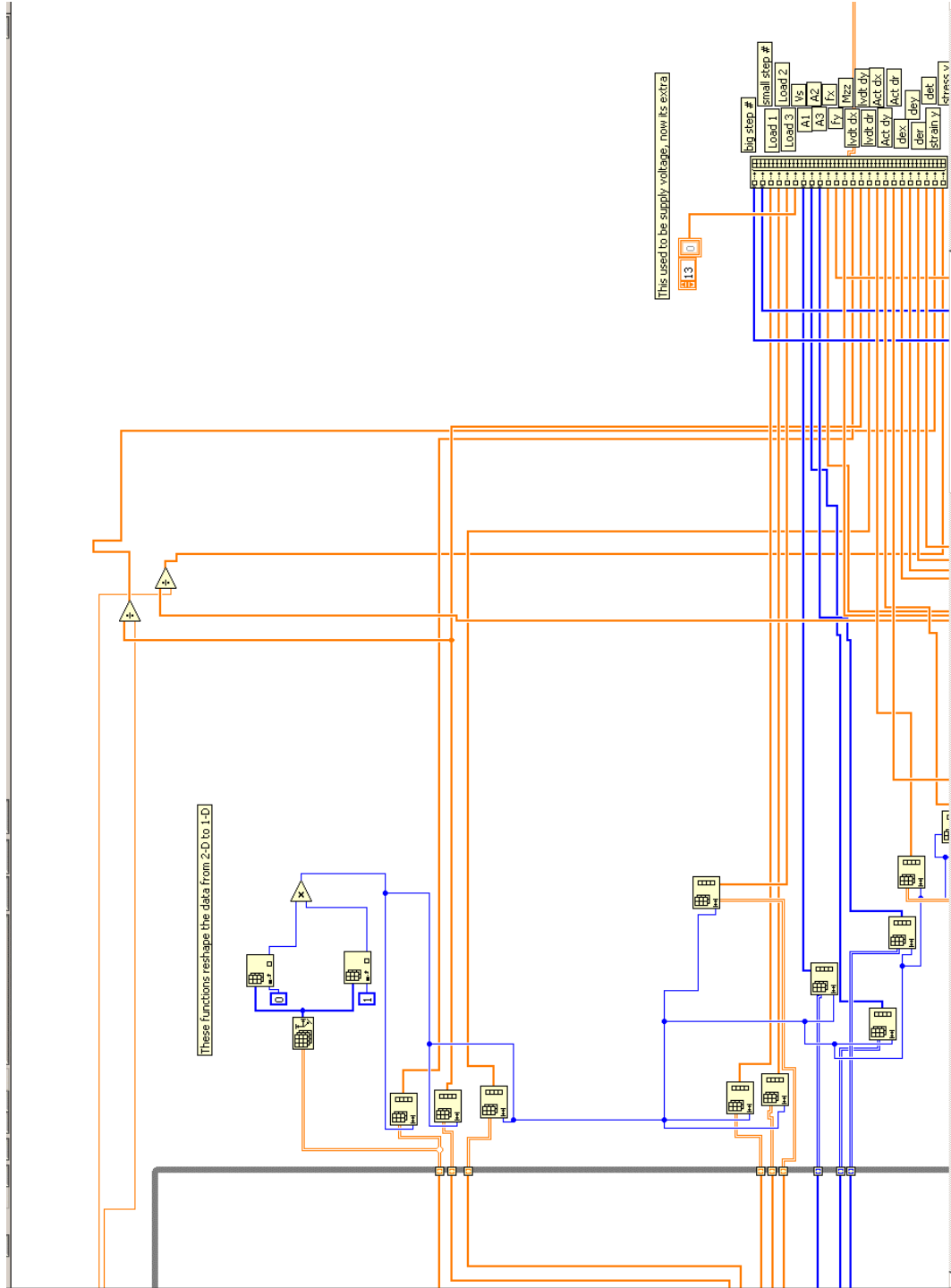




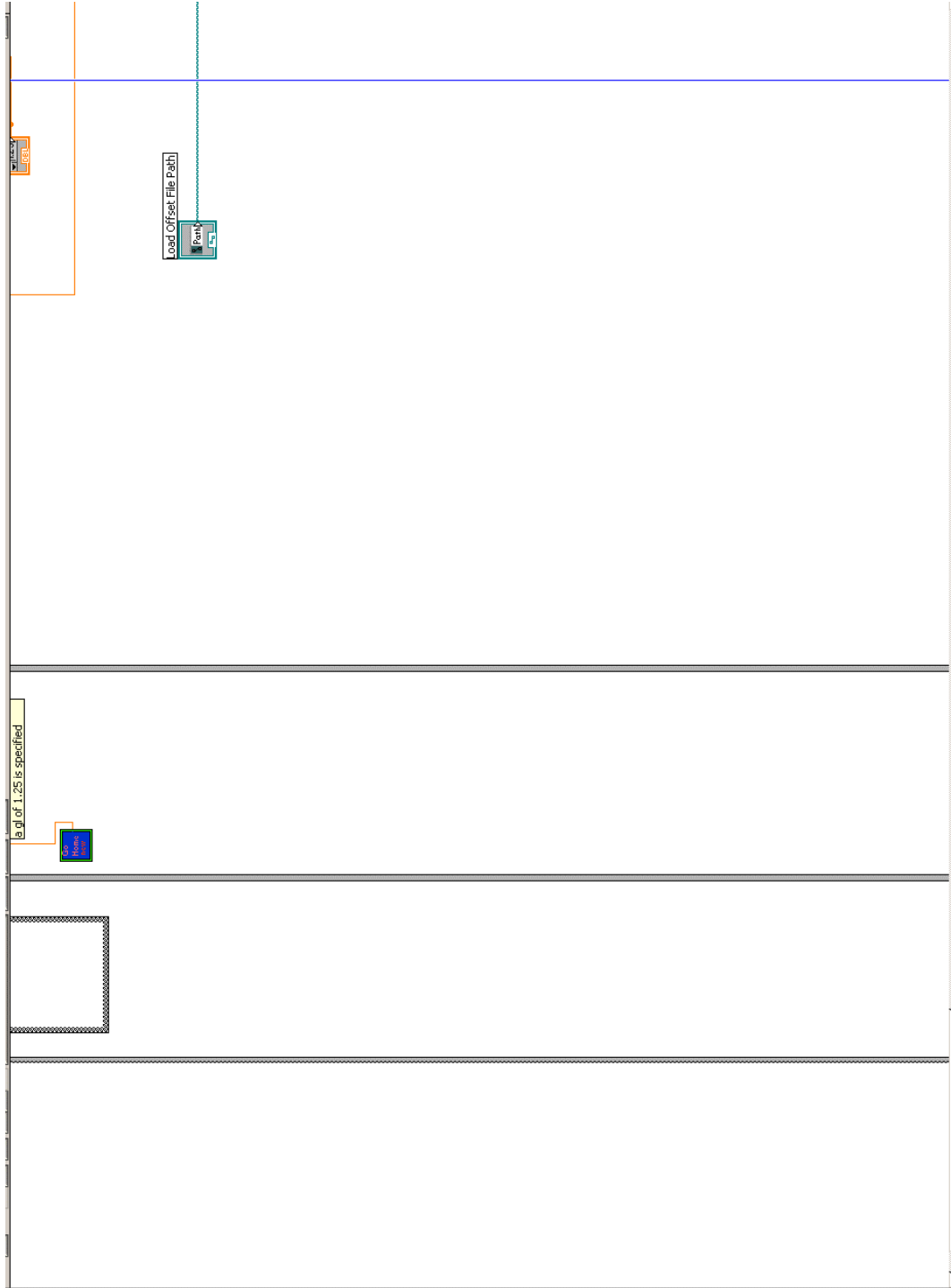
For general information on the operation of this VI, refer to the "Show VI Info..." option under the Windows menu.

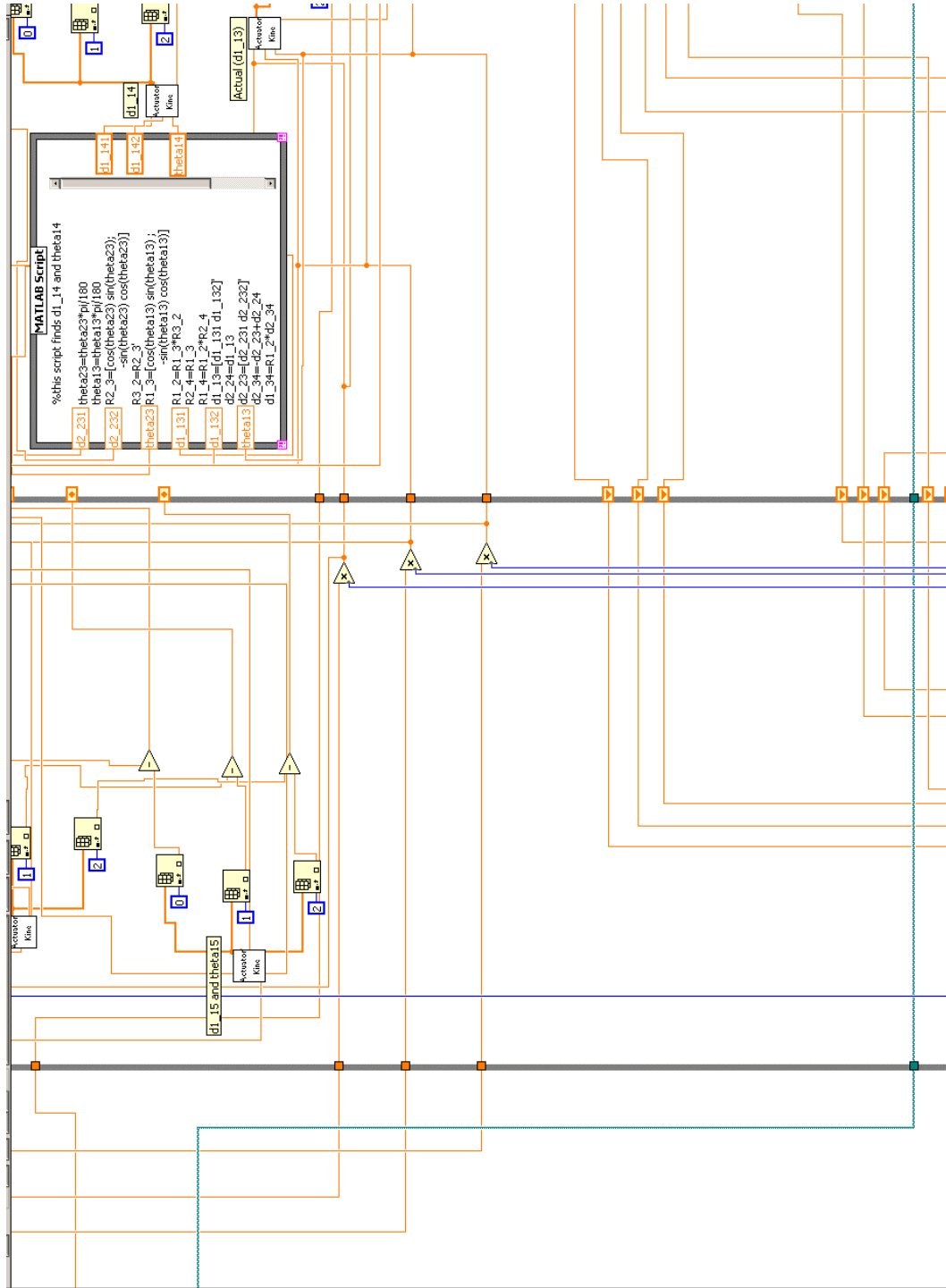
LVDT control for position

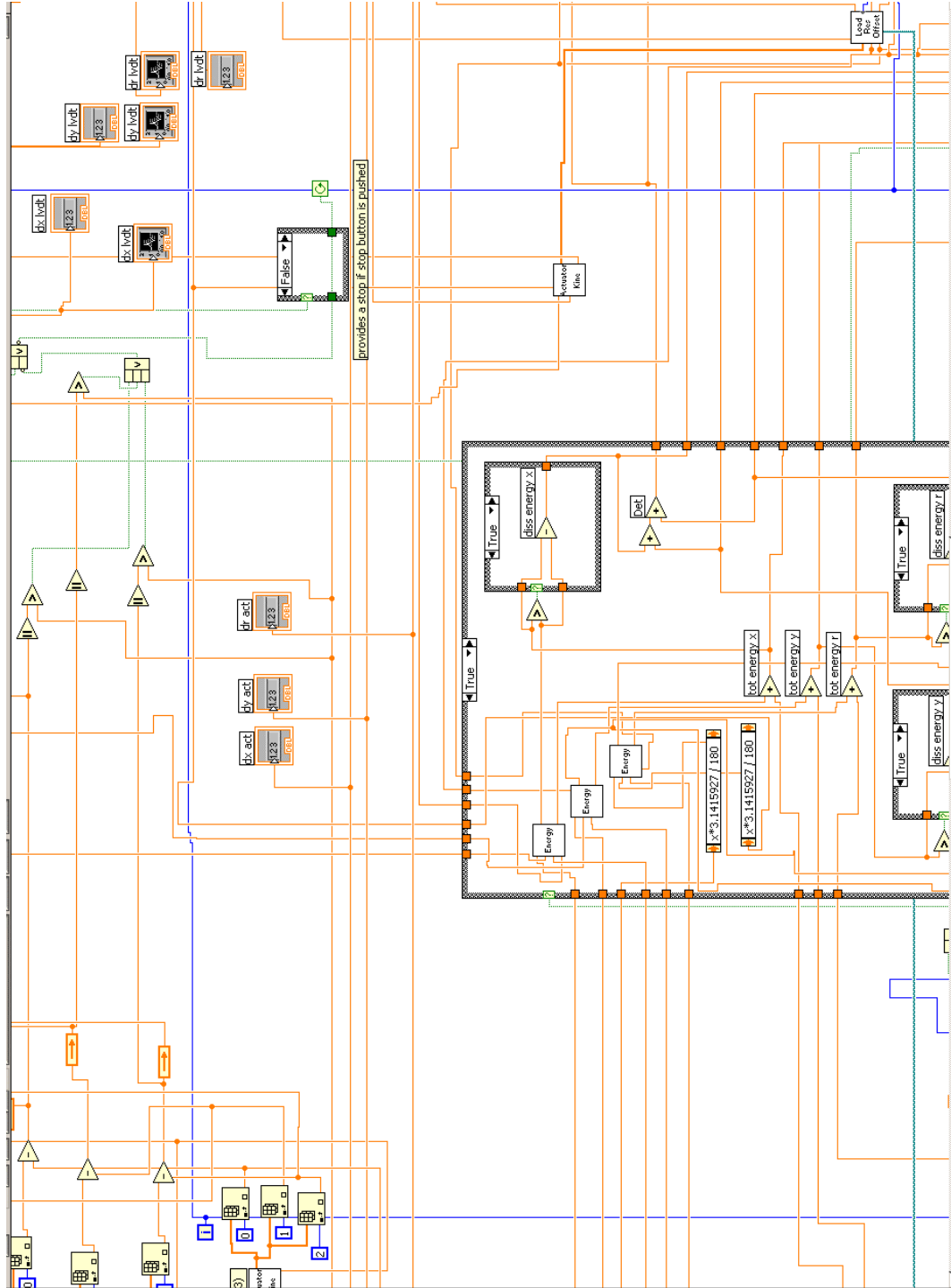


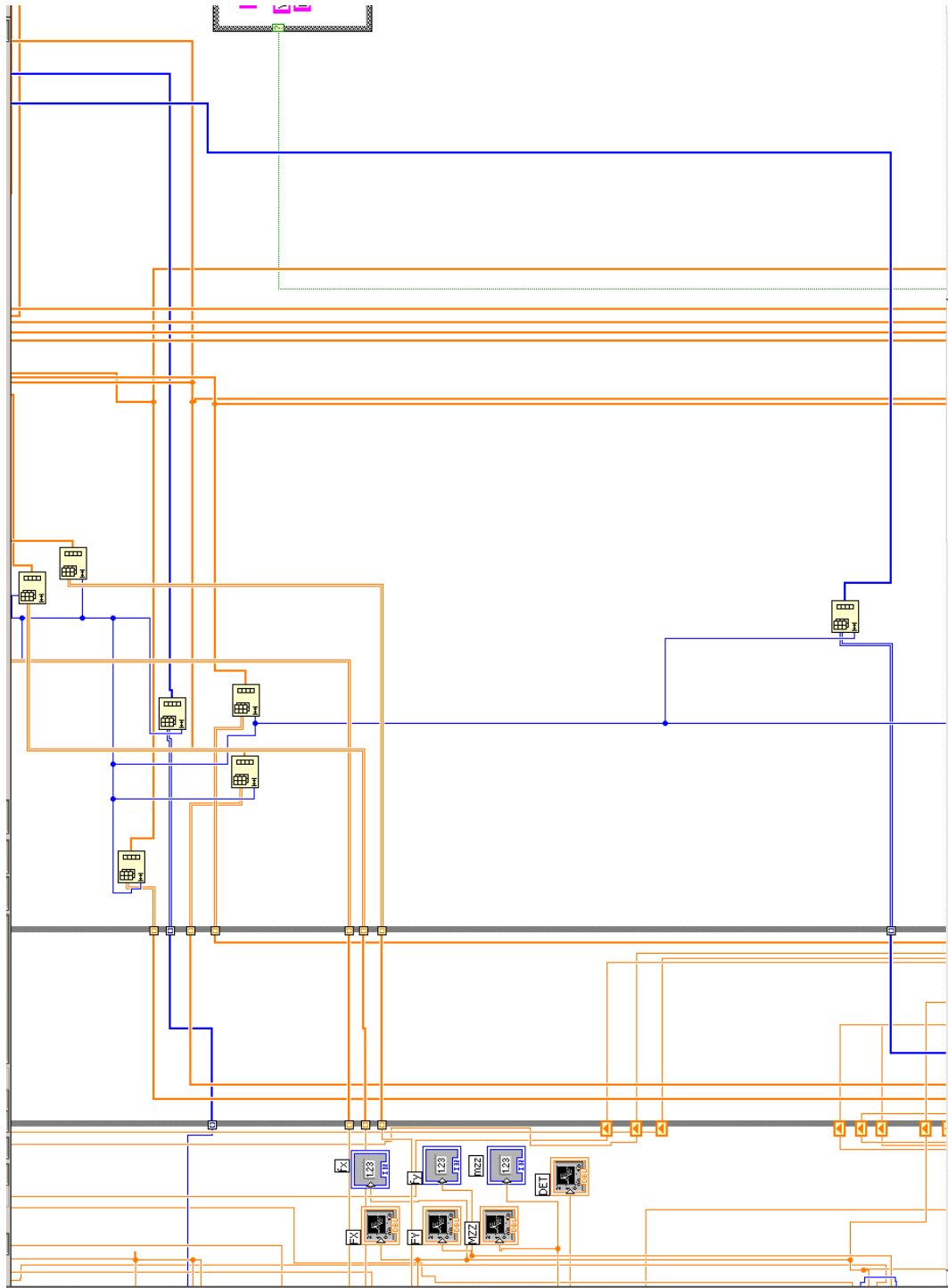




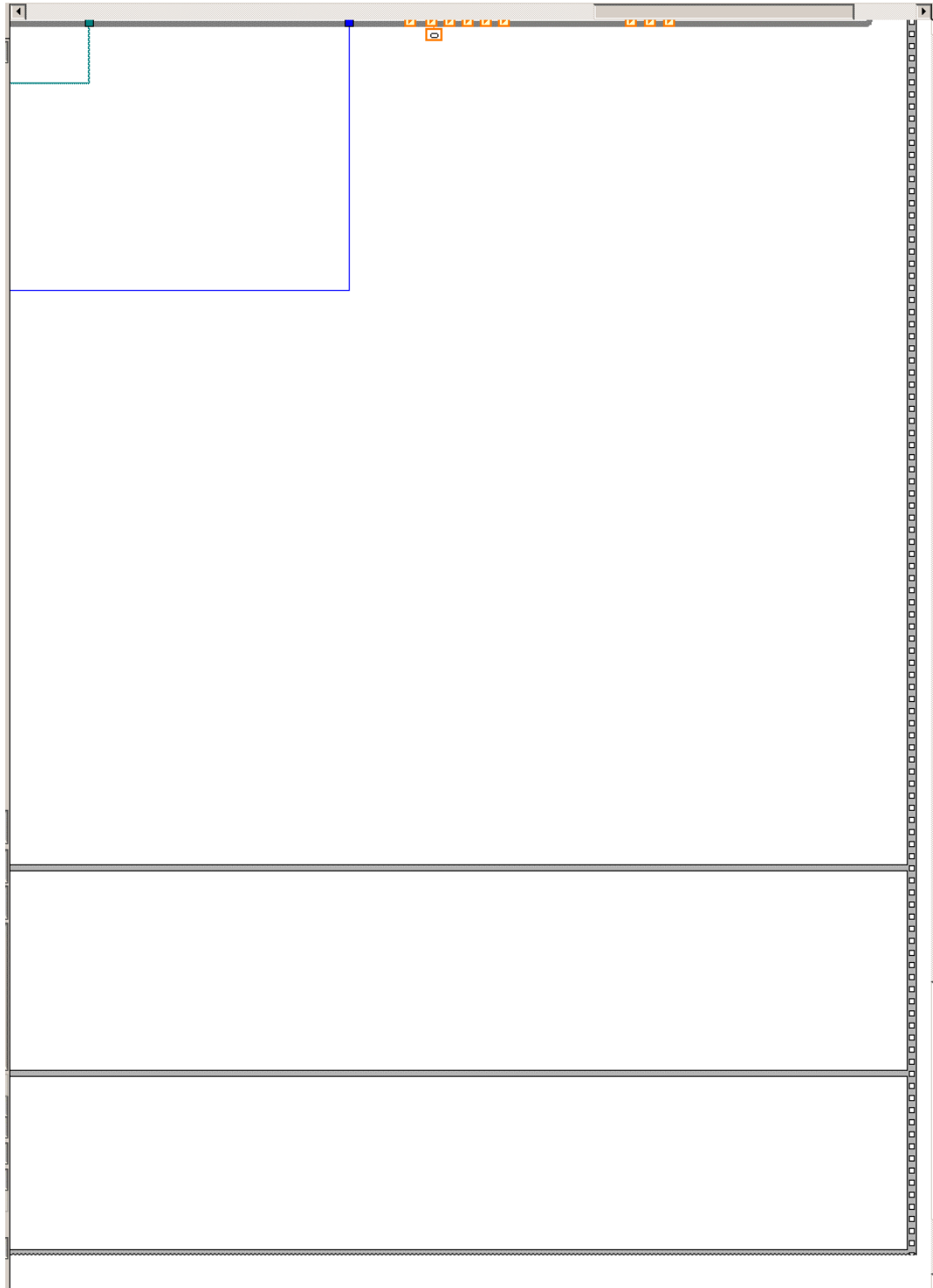


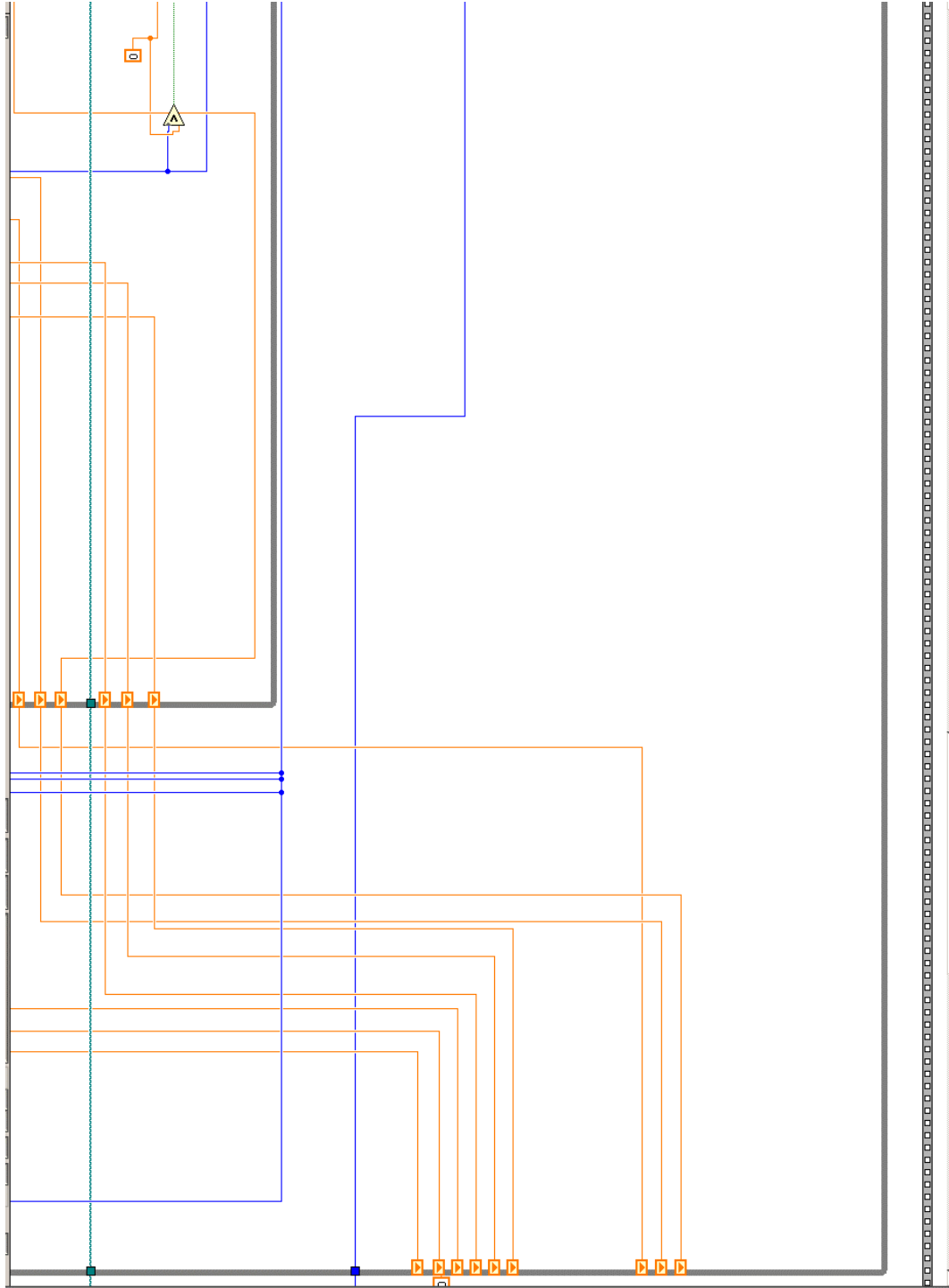


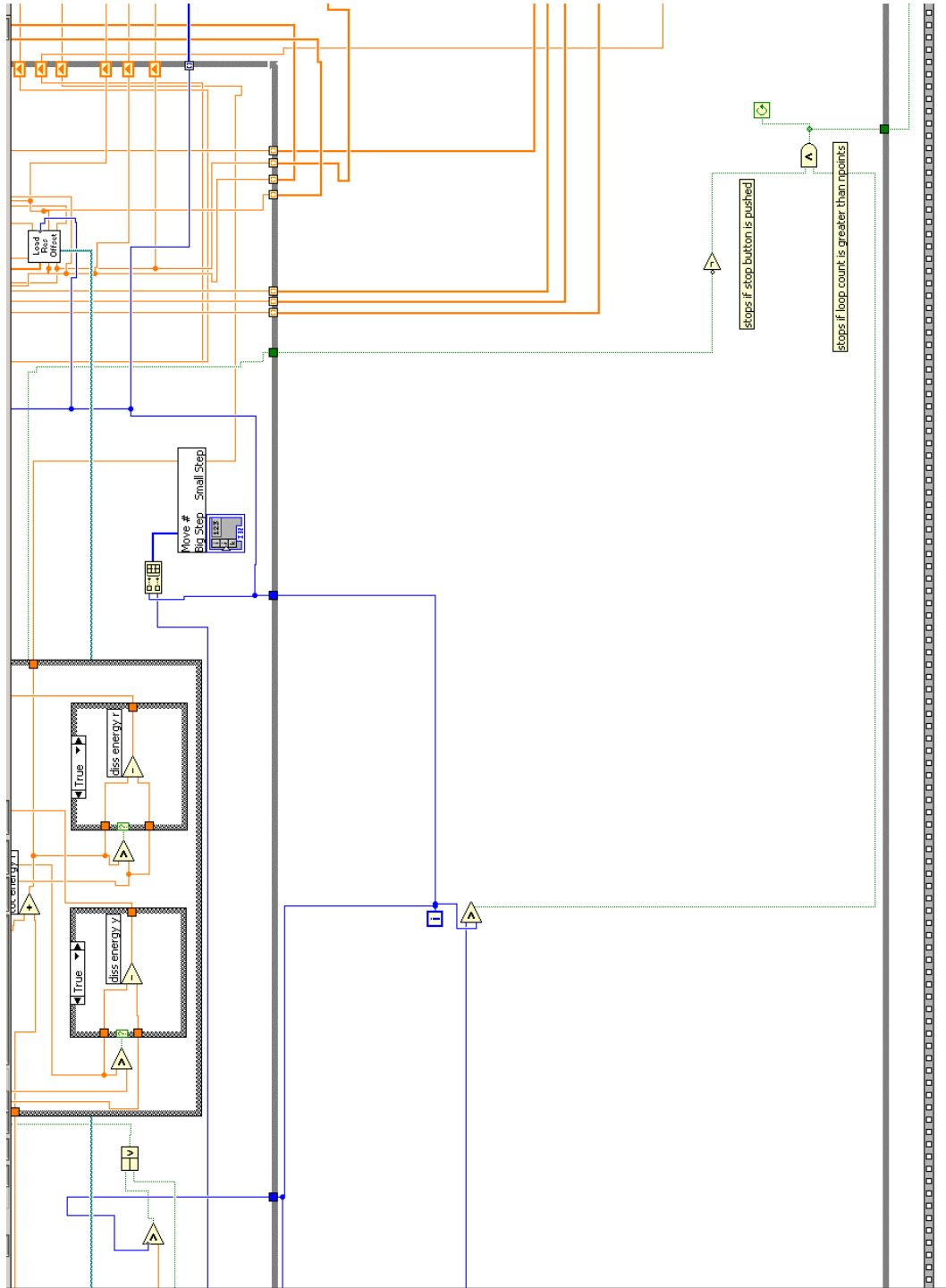


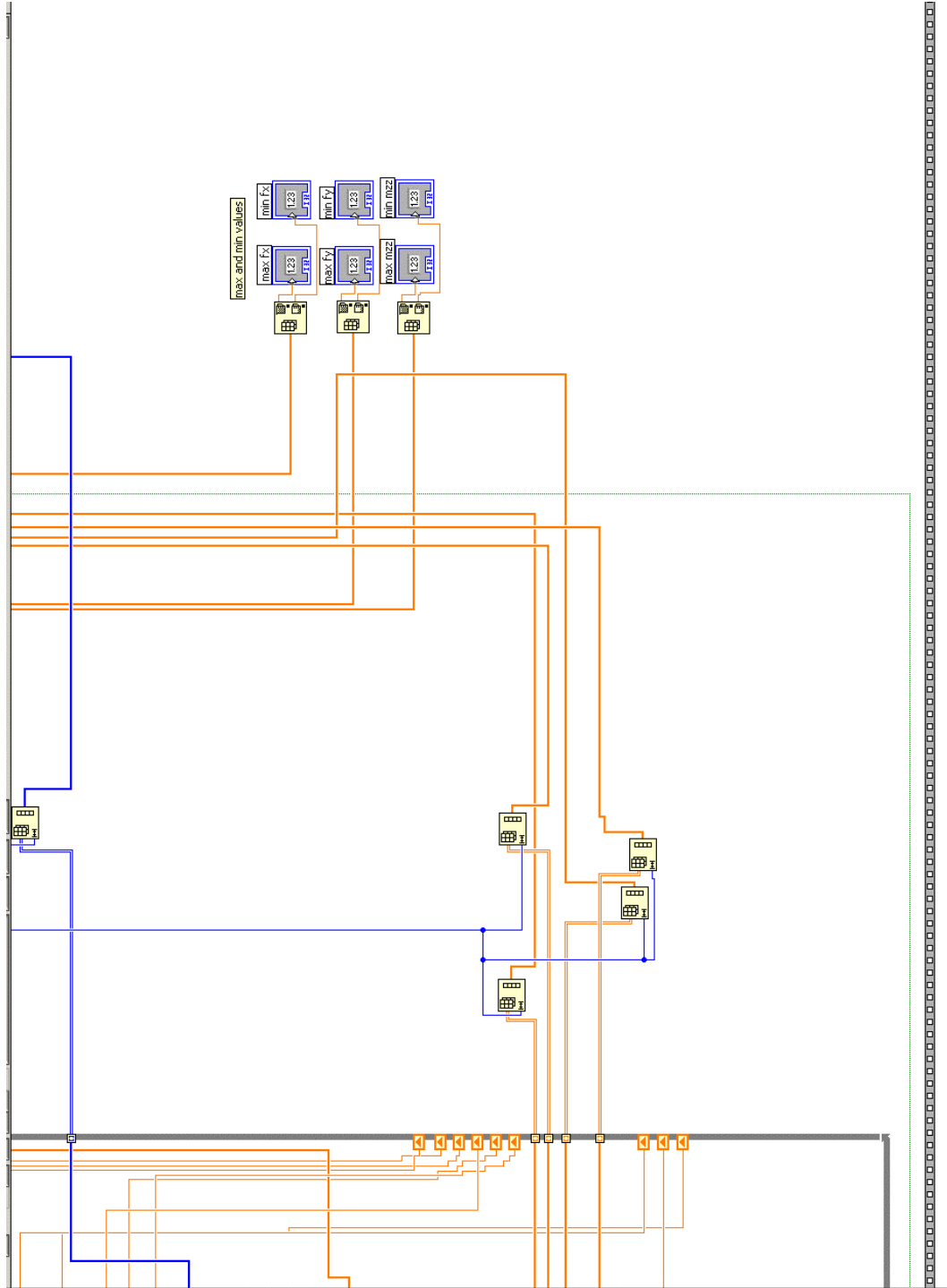












APPENDIX B

MATLAB CODE

IPL Actuator Kinematics

This program finds the actuator lengths and angles for a desired array of IPL boundary conditions.

The variables “npoints”, “dxmax”, “dymin”, “dymax”, and “drmax” are imported from Labview.

```
% Coordinates of the pivot points with 1 inch initial gauge length: (at zero position)
p1=[40.0038 -0.1039]; p2=[12.0249 -11.8695]; p3=[-15.9817 -12.4551];
p4=[20.0463 12.3855]; p5=[15.0270 12.4121]; p6=[-18.2402 12.2643];
```

```
% Create the initial axis vectors. (actuator vectors)
act1i=p4-p1
act2i=p5-p2
act3i=p6-p3
```

```
%Find the length of each initial actuator vector, sqrt(a1^2+a2^2)
lact1i=norm(act1i)
lact2i=norm(act2i)
lact3i=norm(act3i)
```

```
% Create the deformation vector for a displacement
for i=1:npoints+1
```

```
% Array of discrete displacement points
dx=(i-1)*dxmax/npoints;
dy=dymin + (i-1)*(dymax - dymin)/npoints;
dr=(i-1)*drmax/npoints;
```

```
% Position vector of all pivot points after displacement by dx and dy (from origin)
```

```
p1ta=[-dx/2 -dy/2]+p1;
p2ta=[-dx/2 -dy/2]+p2;
p3ta=[-dx/2 -dy/2]+p3;
p4ta=[dx/2 dy/2]+p4;
p5ta=[dx/2 dy/2]+p5;
p6ta=[dx/2 dy/2]+p6;
```

```
% Angle between displaced (and initial) positions of pivot points and x-axis due to dx
and dy (degrees)
```

```
a1=atan2(p1ta(2),p1ta(1))*180/pi;
a2=atan2(p2ta(2),p2ta(1))*180/pi;
a3=atan2(p3ta(2),p3ta(1))*180/pi;
a4=atan2(p4ta(2),p4ta(1))*180/pi;
a5=atan2(p5ta(2),p5ta(1))*180/pi;
a6=atan2(p6ta(2),p6ta(1))*180/pi;
```

```

% Angle between displaced position vectors and x-axis due to dx dy plus dr (radians)
a1t=a1-dr/2;
a2t=a2-dr/2;
a3t=a3-dr/2;
a4t=a4+dr/2;
a5t=a5+dr/2;
a6t=a6+dr/2;
% New lengths of the positions 1,2,3,4,5,6 from origin after displacement step dx,dy,dr
r1=norm(p1ta);
r2=norm(p2ta);
r3=norm(p3ta);
r4=norm(p4ta);
r5=norm(p5ta);
r6=norm(p6ta);
% New position vectors of [(1,2,3,4,5,6),origin] due to dx, dy, and dr
p1t=[r1*cos(a1t*pi/180) r1*sin(a1t*pi/180)];
p2t=[r2*cos(a2t*pi/180) r2*sin(a2t*pi/180)];
p3t=[r3*cos(a3t*pi/180) r3*sin(a3t*pi/180)];
p4t=[r4*cos(a4t*pi/180) r4*sin(a4t*pi/180)];
p5t=[r5*cos(a5t*pi/180) r5*sin(a5t*pi/180)];
p6t=[r6*cos(a6t*pi/180) r6*sin(a6t*pi/180)];
% New position vectors of actuators due to dx, dy, and dr
act1=p4t-p1t;
act2=p5t-p2t;
act3=p6t-p3t;
% Length of actuator position vectors after dx, dy, and dr
lact1=norm(act1);
lact2=norm(act2);
lact3=norm(act3);
% Length of displacement of each actuator due to dx, dy, dr
da1=lact1-lact1i;
da2=lact2-lact2i;
da3=lact3-lact3i;
% Number of steps actuator takes to displace for each data step (rounded to nearest
integer)
st1=round(50000*da1);
st2=round(50000*da2);
st3=round(50000*da3);
% Angle between actuator vectors and x axis (radians)
aa1=atan2(act1(2),act1(1));
aa2=atan2(act2(2),act2(1));
aa3=atan2(act3(2),act3(1));
% Ratio of actuator vector components to actuator length
c1=cos(aa1);

```

```
s1=sin(aa1);
c2=cos(aa2);
s2=sin(aa2);
c3=cos(aa3);
s3=sin(aa3);
% Entering important parameters into data file
% Number of steps each actuator takes for each data step
  datout1(I,1)=st1; datout1(I,2)=st2; datout1(I,3)=st3;
% Amount of displacement for each data step
  datout1(I,4)=dx; datout1(I,5)=dy; datout1(I,6)=dr;
% Ratio of actuator vector components to actuator length for each data step
  datout1(I,7)=c1; datout1(I,8)=s1; datout1(I,9)=c2;
  datout1(I,10)=s2; datout1(I,11)=c3; datout1(I,12)=s3;
% Position points to use as moment arms for Mzz calcs
  datout1(I,13)=p1t(1); datout1(I,14)=p1t(2);
  datout1(I,15)=p2t(1); datout1(I,16)=p2t(2);
  datout1(I,17)=p3t(1); datout1(I,18)=p3t(2);

end
```

IPL Load Resolve Code

This code resolves the loads from load cells 1, 2, and 3 into  $F_x$ ,  $F_y$ , and  $M_z$

$c_1$ ,  $c_2$ ,  $c_3$ ,  $s_1$ ,  $s_2$ , and  $s_3$  are the cosine and sine of the angles that actuators 1, 2, and 3 make with the positive  $x$  axis. These parameters are brought in from the kinematics program shown previously.

```
%component loads
fx1=(load1-offset_load(I,1))*c1;
fx2=(load2-offset_load(I,2))*c2;
fx3=(load3-offset_load(I,3))*c3;
fy1=(load1-offset_load(I,1))*s1;
fy2=(load2-offset_load(I,2))*s2;
fy3=(load3-offset_load(I,3))*s3;

%total component loads
Fx=fx1+fx2+fx3;
Fy=fy1+fy2+fy3;

%moment arms (these are also from the kinematics program)
r1=[datout(I,13),datout(I,14),0];
r2=[datout(I,15),datout(I,16),0];
r3=[datout(I,17),datout(I,18),0];

%load vectors
vf1=[fx1,fy1,0];
vf2=[fx2,fy2,0];
vf3=[fx3,fy3,0];

%Moments for each actuator
Mz1=cross(r1,vf1);
Mz2=cross(r2,vf2);
Mz3=cross(r3,vf3);

%Total moment vector
Mzz=Mz1+Mz2+Mz3;

%picks off the magnitude of the moment
Mzz=Mzz(3);
```

IPL LVDT Program

This program numerically solves the LVDT kinematics to find dx, dy, and dr from the discrete LVDT readings during a test.

```
addpath('C:\IPL\LVDT Files') %adds path to find user defined function 'myfun'
```

```
if i==0
```

```
%This section finds the initial lengths of the LVDT's given the specified g.l.
```

```
Dx=0;
```

```
Dy=G1;
```

```
Dr=0;
```

```
%initial guess positions
```

```
w0=[pi/2 7/8*pi pi/2 7 5 4.7]; %theta1,theta2,theta3,L1,L2,L3
```

```
options=optimset('Display','off'); % Option to display output
```

```
[w,fval] = fsolve(@sol_4_L1L2L3,w0,options,Dx,Dy,Dr); % Call optimizer
```

```
%converts back to degrees
```

```
THETA1=w(1)*180/pi;
```

```
THETA2=w(2)*180/pi;
```

```
THETA3=w(3)*180/pi;
```

```
L1_L_ini=w(4);
```

```
L2_L_ini=w(5);
```

```
L3_L_ini=w(6);
```

```
end
```

```
%These are the LVDT readings at move zero
```

```
if i==0
```

```
L1_ini=l1;
```

```
L2_ini=l2;
```

```
L3_ini=l3;
```

```
end
```

```
%This section finds the actual dx, dy, dr
```

```
%Actual lengths of the LVDT's when vise blocks touch
```

```
L1=L1_L_ini+l1-(L1_ini);
```

```
L2=L2_L_ini+l2-(L2_ini);
```

```
L3=L3_L_ini+l3-(L3_ini);
```

```
%initial guess positions
```

```

x0=[pi/2 7/8*pi pi/2 0 0 0]; %theta1,theta2,theta3,dtheta,dx,dy

options=optimset('Display','off'); % Option to display output

[x,fval] = fsolve(@sol_4_dxdydr,x0,options,L1,L2,L3); % Call optimizer

%converts back to degrees
THETA1=x(1)*180/pi;
THETA2=x(2)*180/pi;
THETA3=x(3)*180/pi;

DX=x(5);
DY=x(6);
DTHETA=x(4)*180/pi;

if i==0
DX_ini=DX;
DY_ini=DY;
DTHETA_ini=DTHETA;
end

DX=DX-DX_ini;
DY=DY-DY_ini;
DTHETA=DTHETA-DTHETA_ini;

%This is the function sol_4_L1L2L3

function F=sol_4_L1L2L3(x,DX,DY,DR)

LVDT_Positions %this brings in the LVDT initial kinematic information

theta1=x(1);
theta2=x(2);
theta3=x(3);
dtheta=DR;

fi=pi/2+dtheta;
si=fi-gama;
bata=fi+alfa;

L1x=x(4)*cos(theta1);
L2x=x(5)*cos(theta2);
L3x=x(6)*cos(theta3);

```

```

dx=d*cos(si);
ex=e*cos(si);
fx=f*cos(bata);
gx=g*cos(fi);

```

```

L1y=x(4)*sin(theta1);
L2y=x(5)*sin(theta2);
L3y=x(6)*sin(theta3);
dy=d*sin(si);
ey=e*sin(si);
fy=f*sin(bata);
gy=g*sin(fi);

```

```

kx=DX;
ky=DY;

```

```

F=[ -L1x+cx+hx+kx+gx+dx;
    -L1y+cy+hy+ky+gy+dy;
    bx+L2x+ex-gx-kx-hx;
    by+L2y+ey-gy-ky-hy;
    ax+L3x+fx-L2x;
    ay+L3y+fy-L2y];

```

```

%This is the function sol_4_dxdydr

```

```

function F=sol_4_dxdydr(x,L1,L2,L3)

```

```

LVDT_Positions    %this brings in the LVDT initial kinematic information

```

```

theta1=x(1);
theta2=x(2);
theta3=x(3);
dtheta=x(4);

```

```

fi=pi/2+dtheta;
si=fi-gama;
bata=fi+alfa;

```

```

L1x=L1*cos(theta1);
L2x=L2*cos(theta2);
L3x=L3*cos(theta3);
dx=d*cos(si);
ex=e*cos(si);

```

```
fx=f*cos(bata);
gx=g*cos(fi);
```

```
L1y=L1*sin(theta1);
L2y=L2*sin(theta2);
L3y=L3*sin(theta3);
dy=d*sin(si);
ey=e*sin(si);
fy=f*sin(bata);
gy=g*sin(fi);
```

```
kx=x(5);
ky=x(6);
```

```
F=[ -L1x+cx+hx+kx+gx+dx;
    -L1y+cy+hy+ky+gy+dy;
    bx+L2x+ex-gx-kx-hx;
    by+L2y+ey-gy-ky-hy;
    ax+L3x+fx-L2x;
    ay+L3y+fy-L2y];
```

%This is the LVDT initial information called "LVDT\_Positions" in inches.

```
Ax=-4.0860;
bx=-3.5020;
cx=-6.8045;
hx=0;
```

```
ay=-1.9785;
by=1.4052;
cy=2.7303;
hy=2.2987;
```

```
d=8.3091;
e=9.3148;
f=1.4235;
g=0.1320;
```

```
gama=86.72*pi/180;
alfa=133.12*pi/180;
```

IPL LVDT Feedback Loop

This script finds d1\_14 and theta14

%The following 3 parameters are known from the LVDT displacement readings

d2\_231=-10;

d2\_232=10;

theta23=45

%The following 3 parameters are known from the specified movements the IPL should take

d1\_131=0;

d1\_132=20;

theta13=45

%The rest is used to find theta 34 and d1\_34

%converts degrees to radians

theta23=theta23\*pi/180;

theta13=theta13\*pi/180;

%rotation matrices

R2\_3=[cos(theta23) sin(theta23);  
-sin(theta23) cos(theta23)];

R3\_2=R2\_3';

R1\_3=[cos(theta13) sin(theta13) ;  
-sin(theta13) cos(theta13)];

R1\_2=R1\_3\*R3\_2;

R2\_4=R1\_3;

R1\_4=R1\_2\*R2\_4;

R3\_4=R3\_2\*R2\_4;

d1\_13=[d1\_131 d1\_132]'

d2\_24=d1\_13;

d2\_23=[d2\_231 d2\_232]'

d2\_34=-d2\_23+d2\_24

d1\_34=R1\_2\*d2\_34

d1\_14=d1\_13+d1\_34

d1\_141=d1\_14(1);

d1\_142=d1\_14(2);

theta14=atan2(R1\_4(1,2),R1\_4(1,1))\*180/pi

theta34=atan2(R3\_4(1,2),R3\_4(1,1))\*180/pi

APPENDIX C

ANSYS CODE

Tension/Shear/Compression Test FEA Sample Code

This code imports an iges file which contains the coupon geometry and applies a boundary displacement in tension. It then finds the force reaction at the boundary. Compression and shear sample code is similar.

```
FINISH
/CLEAR
```

```
*SET,YOUNGS,10E6
*SET,POISSONS,.33
*SET,ELSIZE,.05
*SET,DY,.002
```

```
IOPTN,IGES,NODEFEAT
IOPTN,MERGE,YES
IOPTN,SOLID,YES
IOPTN,SMALL,YES
IOPTN,GTOLER,DEFA
IGESIN, TEST_29 ,'IGS',..\..\..\IPL\TEST DATA\9-30-05 INSTRON AND IPL
TESTS\TEST 29'
```

```
FINISH
/PREP7
```

```
ET,1,SOLID45
MPTEMP,,,,,,,,
MPTEMP,1,0
MPDATA,EX,1,,YOUNGS
MPDATA,PRXY,1,,POISSONS
```

```
LWPL,-1,15,0.5
WPSTYLE,0.05,0.1,-1,1,0.003,0,0,,5
VSBW, 1
LWPL,-1,4,0
LWPL,-1,4,1
VSBW, 3
LWPL,-1,29,1
FLST,2,2,6,ORDE,2
FITEM,2,1
FITEM,2,4
VSBW,P51X
WPSTYLE,,,,,,,,0
```

FLST,2,3,5,ORDE,3  
FITEM,2,2  
FITEM,2,7  
FITEM,2,11  
DA,P51X,SYMM

FLST,2,2,5,ORDE,2  
FITEM,2,12  
FITEM,2,18  
/GO  
DA,P51X,UY,-DY

ESIZE,ELSIZE  
MSHAPE,0,3D  
MSHKEY,1

FLST,5,5,6,ORDE,4  
FITEM,5,2  
FITEM,5,-3  
FITEM,5,5  
FITEM,5,-7  
CM,\_Y,VOLU  
VSEL,, , ,P51X  
CM,\_Y1,VOLU  
CHKMSH,'VOLU'  
CMSEL,S,\_Y

VMESH,\_Y1

CMDELE,\_Y  
CMDELE,\_Y1  
CMDELE,\_Y2

FINISH  
/SOL

FLST,2,5,5,ORDE,5  
FITEM,2,4  
FITEM,2,21  
FITEM,2,24  
FITEM,2,-25  
FITEM,2,29  
FLST,2,1,5,ORDE,1

```
FITEM,2,27  
ASEL,,LOC,Z,0  
DA,ALL,UZ,0
```

```
ALLSEL  
FINISH  
/SOLU  
SOLVE  
ALLSEL,ALL  
SOLVE  
FINISH  
/POST1  
NSEL,,LOC,Y,0  
FSUM
```

FEA Optimization Code for Coupon Geometry

This code optimizes the coupon geometry seen in Figure 66.

Code to Build the Model

```

/PREP7

*SET,YOUNGS,10E6
*SET,POISSONS,.33
*SET,ELSIZE,.05
*SET,DY,.02

THICK=.125
WIDE=.5
LONG_NOTCH=.96/2
THIN=.1
RAD=.125
LONG=LONG_NOTCH+RAD+1

ET,1,SOLID45

MP,EX,1,YOUNGS
MP,PRXY,1,POISSONS

K,1,0,0,0
K,2,THIN,0,0
K,3,THIN,-LONG_NOTCH,0
K,4,THIN+RAD,-RAD-LONG_NOTCH,0
K,5,WIDE,-RAD-LONG_NOTCH,0
K,6,WIDE,-LONG,0
K,7,0,-LONG,0
K,8,THIN+RAD,0,0

L,1,2
L,2,3
L,4,5
L,5,6
L,6,7
L,7,1
LARC,3,4,8,RAD

```

AL,ALL  
VEXT,ALL,,,,,THICK

LWPL,-1,10,0.5  
VSBW, 1

LWPL,-1,31,0  
VSBW, 3

LWPL,-1,33,1

FLST,2,2,6,ORDE,2  
FITEM,2,1  
FITEM,2,4  
VSBW,P51X

LWPL,-1,26,0  
VSBW, 2

ESIZE,ELSIZE  
MSHAPE,0,3D  
MSHKEY,1  
VMESH,ALL

FLST,2,4,5,ORDE,4  
FITEM,2,3  
FITEM,2,5  
FITEM,2,16  
FITEM,2,33  
DA,P51X,SYMM

FLST,2,2,5,ORDE,2  
FITEM,2,9  
FITEM,2,19  
DA,P51X,UY,-DY

FLST,2,1,5,ORDE,1  
FITEM,2,25  
DA,P51X,UZ,0

FINISH  
/SOL  
SOLVE

FINISH  
/POST1

NSEL,,LOC,Y,0  
FSUM

\*GET, FSUM\_Y\_0, FSUM,0 , ITEM,FY

ALLS

FYDYFEA=-FSUM\_Y\_0/DY

FYDYEXP=142000

SSE=(FYDYFEA-FYDYEXP)\*\*2

FINISH

Code to Optimize Coupon

/COM, \*\*\*\*\*  
/COM, \*\*\* AARON COUPON DIMENSION OPTIMIZATION \*\*\*  
/COM, \*\*\*\*\*

/COM, \*\*\* ENTER OPT AND IDENTIFY ANALYSIS FILE \*\*\*

/OPT  
OPCLR

OPANL,'TENSION\_COUPON\_NOTCH\_SECTION','TXT','C:\DOCUMENTS AND  
SETTINGS\OWNER\DESKTOP\IPL 2'

/COM, IDENTIFY OPTIMIZATION VARIABLES  
OPVAR,THIN,DV,0.001,.25,  
OPVAR,RADC,DV,.125,.5,.125  
OPVAR,FYDYFEA,SV,140000,144000,  
OPVAR,SSE,OBJ,,, ! OBJ: FORCE DIVIDED BY DISPLACEMENT

/COM, \*\*\* RUN THE OPTIMIZATION \*\*\*  
OPKEEP,ON ! SAVE BEST DESIGN  
!OPSEL,-1 ! DELETE INFEASIBLE DESIGNS  
!OPTYPE,SWEEP ! SWEEP TOOL  
!OPSWEEP, BEST,2 ! REFERENCE POINT FOR SWEEP GENERATION  
OPTYPE,SUBP ! SUBPROBLEM APPROXIMATION METHOD  
!OPSWEEP,,5  
!OPMAKE

OPSUBP,100,50,  
OPEQN,0,0,0,0,0,

!OPSAVE,'TEST\_23','OPT0','C:\IPL\TEST DATA\9-30-05 INSTRON AND IPL  
TESTS\TEST 23\' ! SAVE THE CURRENT OPT DATABASE  
!OPDATA,'TEST\_23','OPT','C:\IPL\TEST DATA\9-30-05 INSTRON AND IPL  
TESTS\TEST 23\'

OPEXE

/COM, \*\*\* REVIEW RESULTS \*\*\*  
OPLIST,ALL,,1 ! LIST ALL DESIGN SETS

FINISH